Downloaded from orbit.dtu.dk on: Apr 30, 2024

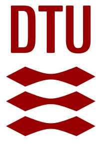

DTU Library

MEMS Tunable nanostructured photodetector

Learkthanakhachon, Supannee

Publication date:
2015

Document Version
Publisher's PDF, also known as Version of record

Link back to DTU Orbit

Citation (APA):
Learkthanakhachon, S. (2015). *MEMS Tunable nanostructured photodetector*. Technical University of Denmark.

General rights
Copyright and moral rights for the publications made accessible in the public portal are retained by the authors and/or other copyright owners and it is a condition of accessing publications that users recognise and abide by the legal requirements associated with these rights.

- Users may download and print one copy of any publication from the public portal for the purpose of private study or research.
- You may not further distribute the material or use it for any profit-making activity or commercial gain
- You may freely distribute the URL identifying the publication in the public portal

If you believe that this document breaches copyright please contact us providing details, and we will remove access to the work immediately and investigate your claim.

MEMS Tunable nanostructured photodetector

Supannee Learkthanakhachon

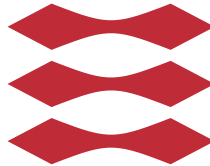

Photonics Engineering
Technical University of Denmark
A thesis submitted for the degree of
Doctor of Philosophy
2015

Technical University of Denmark
Department of Photonics Engineering
Ørsteds Plads, building 343,
FTNK-PhD-2015

Preface

This thesis was prepared at the department of Photonics Engineering, the Technical University of Denmark in fulfilment of the requirements for acquiring a Philosophiae doctor (Ph.D.) in Photonics Engineering.

The thesis deals with the design and fabrication of tunable resonant-cavity-enhanced photodetector using dielectric subwavelength gratings as reflectors operating at 1550 nm optical communication wavelength. The main work in this thesis divided equally into device design and process development. The properties of dielectric subwavelength grating are described.

The main result of the thesis is the new resonant cavity structure using dielectric subwavelength gratings as ultra high reflective broadband reflectors and process development to realize the design. The tuning characteristics are reported for different types of cavities and compared with the conventional distributed Bragg reflector (DBR) structure.

Results from the fabricated devices are reported along with an investigation of the design parameters which influence the performance deviation from the design.

Supannee Learkthanakhachon

Acknowledgements

I would like to thank Associate Professor Il-Sug Chung and Associate Professor Kresten Yvind for being supervisors of the work and gratefully acknowledge the DTU PhD Scholarship, NATEC Center of Excellent, and Danish Research Council for funding this project. I would especially like to thank Alireza Taghizadeh for developing the code and designing the HG-HCG device structure and Gyeong Cheol Park for optimizing processing flow of chip bonding. I would like to also extend my thanks to Danchip Cleanroom staffs for practical assistance to the work and special thanks goes to Peixiong Shi for late night discussion on technology of electron beam lithography, providing accompany documents as a reference for my design of experiment, and stayed after office hours to assist me. The inspiration, assistance, technical discussions from the PhD students and staffs in Nanophotonics Signal and Processing group ad Nanophotonics Device group are very much appreciated as well.

Contents

Preface i

Acknowledgements iii

1 Introduction 1
- 1.1 Tunable photodetectors: background and perspective 1
- 1.2 Resonant cavity enhanced photodetectors 3
- 1.3 Photodetectors on Si platform 4
- 1.4 Thesis outline 6

2 Dielectric Subwavelength Gratings (SWGs) 7
- 2.1 Introduction 7
- 2.2 Subwavelength High Contrast Grating (HCG) 9
  - 2.2.1 Theory of HCG as Broadband reflector 10
  - 2.2.2 Properties of HCG reflectors 11
- 2.3 Subwavelength Hybrid Grating (HG) Reflector 16
- 2.4 Summary 19

3 Tunable Resonant Cavity Enhanced (RCE) Photodetector Design 21
- 3.1 Resonant Cavity Design 22
  - 3.1.1 Theory of RCE photodetectors 22
  - 3.1.2 Tunable RCE with HCGs 27
  - 3.1.3 Tunable RCE with HGs 39
- 3.2 Micro-Electro-Mechanical System (MEMS) Design 43
  - 3.2.1 Electrostatic Actuation 44
  - 3.2.2 Beam Bending 46
  - 3.2.3 MEMS simulation 47

4 Device Fabrication 51
4.1 Device Processing . . . 51
4.2 Processing tests . . . 59
4.2.1 Electron beam dose test . . . 59
4.2.2 Reactive ion etching of the grating . . . 60
4.2.3 Wet etch tests . . . 64
4.2.4 Lift off process . . . 66
4.2.5 Metal deposition on a tapered BCB . . . 67
4.3 Summary . . . 68

5 Device Characterization 69
5.1 Characterization . . . 69
5.1.1 Characterization set up . . . 70
5.1.2 Diode characteristics: Current vs. Voltage . . . 71
5.1.3 Photocurrent spectrum . . . 72
5.2 Discussion on the broken metal lines . . . 76
5.3 Summary . . . 76

6 Conclusion and Outlook 79
6.1 Conclusion . . . 79
6.2 Outlook . . . 80

A Fabrication Process 83
A.1 Process Flow . . . 83

B Mask Design 99

C Device Structure 105
C.1 Double HCG Device Structure . . . 105
C.2 Hybrid HG-HCG Device Structure . . . 107
C.3 III-V Epitaxy for Fabrication . . . 108

Bibliography 109

CHAPTER 1

Introduction

In this chapter, an introduction to the field of research and motivation is described. The background and perspective of the current advances in tunable resonant cavity photodetectors are given in the first section. Next, the history of the resonant-cavity-enhanced (RCE) photodetector is briefly mentioned. Then, integration techniques to the Si platform are discussed. The last section will describe the outline of this thesis.

1.1 Tunable photodetectors: background and perspective

Tunable photodetectors with narrow spectral linewidth, large tuning wavelength range, and small footprint are attractive devices for applications in which capability of wavelength-selective light detection is demanded. For example, in the wavelength division multiplexing-passive optical network (WDM-PON), such tunable photodetectors can be employed on the receiver site of passive broadcasting, i.e., optical network units (ONUs), providing new WDM-PON design possibilities. Portable compact spectrometers are another application of interest.

So far, many tunable photodetector structures have been reported [1–9]. Among them, the resonant-cavity-enhanced (RCE) photodetector structure is the most suitable for achieving the narrow spectral linewidth, thanks to inherent resonance in the structure [10]. Compared to conventional p-i-n photodiodes, p-i-n RCE photodetectors can provide higher absorption efficiency at resonance as well as faster intrinsic response. So far, most of the research effort on RCE photodetectors emphasizes on static wavelength selectivity and related applications, e.g., in [11, 12]. Then, several approaches for gaining tunable wavelength selectivity have been investigated, by using a micromachined movable aluminum mirror [9], the quantum confined Stark effect with an air-semiconductor interface as a mirror [6, 7], and a movable distributed Bragg reflector (DBR) [4, 8]. To get narrow spectral linewidth, both reflectors of the RCE photodetector need to have sufficiently high reflectivity. In this respect, the movable DBR approach is ideal. The broadest tuning range experimentally demonstrated by using the movable DBR approach is 75 nm with the spectral linewidth of 4 nm to 6 nm.

In recent years, high-index-contrast subwavelength gratings (HCG) have received great attention for high, broadband, and polarization-selective reflectivity for normal incident light [13, 14]. HCGs, a membrane layer with one- or two-dimensional periodic perforations, are typically made of semiconductor or dielectric material surrounded by low refractive index media [15]. Due to high reflectivity property, compactness, and other novel functionalities, the HCGs become attractive candidate to replace the DBRs for integrated photonics devices including lasers, filters, waveguides, and sensors [16]. Recently, it has been shown that tunable vertical-cavity surface-emitting lasers (VCSELs) can potentially achieve tuning range as large as 100 nm by employing a HCG as a movable reflector [17]. This motivates the work in this thesis for RCE photodetector structures have similar optical cavity as VCSELs. In this thesis, We would like to investigate the static and tuning characteristics of RCE photodetectors based on HCGs.

In this work, we propose three tunable RCE photodetector designs with subwavelength gratings operating at 1550-nm wavelength. The proposed structures are hybrid structure combining InP material with Si wafer. The movable HCG is made of InP and the other fixed subwavelength grating is made of Si. The tuning range, peak absorption efficiency, spectral linewidth, and polarization selectivity are numerically investigated and discussed.

1.2 Resonant cavity enhanced photodetectors

Photodiodes are semiconductor devices with a p-n or p-i-n structure, operating under reverse bias which create a depletion region. The depletion region is a region free of charge carrier and has built-in electric field that opposes the flow of electrons from the n-side to the p-side. When the photodiode is illuminated, electron-hole pairs are created in the depletion region through absorption. Then, the electrons and holes are drifted to the n- and p-sides, respectively. This flow of photocurrent is proportional to the incident optical power. The main difference between the p-n and p-i-n structures is that the p-i-n structure has a drift component dominates over the diffusion component compares to the p-n structure because the depletion width can be tailored and is larger in p-i-n photodiodes. The question is how large the depletion width should be for the p-i-n photodiodes?

Generally, there are three parameters that are used to evaluate the detector performances. They are responsivity, dark current, and bandwidth. Responsivity is a ratio of photocurrent to optical incident power. Dark current is response current of the detector without light signal. Bandwidth is the parameter which determines the device speed. To achieve a high-speed response, the thickness of the depletion region has to be thin which allow electron-hole pairs to escape quickly. However, the thin depletion region causes low responsivity. The responsivity, R, of the device is related to quantum efficiency, η, by the following equation:

$$R = \eta \frac{e}{hv} \tag{1.1}$$

where hv is the photon energy and e is the elementary charge particle. The quantum efficiency can be expressed as:

$$\eta = \frac{P_{abs}}{P_{in}} = 1 - e^{-\alpha d} \tag{1.2}$$

where P_{abs} and P_{in} are the absorbed power and incident power, respectively. α is the absorption coefficient and d is the depletion width. It is seen that the quantum efficiency of the device is proportional to the depletion width.

In the 1990s, considerable amount of effort was directed to improve high speed and high efficiency of the p-i-n photodiodes [18]. Several techniques have been proposed. The most promising approach is having a Fabry-Perot cavity formed around the p-i-n structure. This is a structure in which a vertical-cavity surface-emitting lasers (VCSEL) is made [19]. This type of photodiode is referred to as the RCE photodiode. The Fabry-Perot cavity has a set of longitudinal modes

where the optical field resonates constructively. As a result, the sensitivity of the photodiode can be enhanced greatly while a small depletion width is maintained. The wavelength selective nature of such structure is desirable for WDM applications. The detection wavelength can be shifted by adjusting the cavity length.

1.3 Photodetectors on Si platform

Silicon (Si) has been dominated an integrated circuit industry for decades. Due to bandwidth limitation because of line impedance and to eliminate electromagnetic interference that comes from inductance and capacitance of electrical interconnects, there have been efforts trying to use optical interconnects for intra-board and inter-board communications [20]. However, challenges of optical interconnect to be implemented widely remain unsolved. The optical devices such as lasers and detectors should be integrated with electrical driving circuits. Several kinds of semiconductor materials such as Si, Ge, and III-V materials have been studied and proposed.

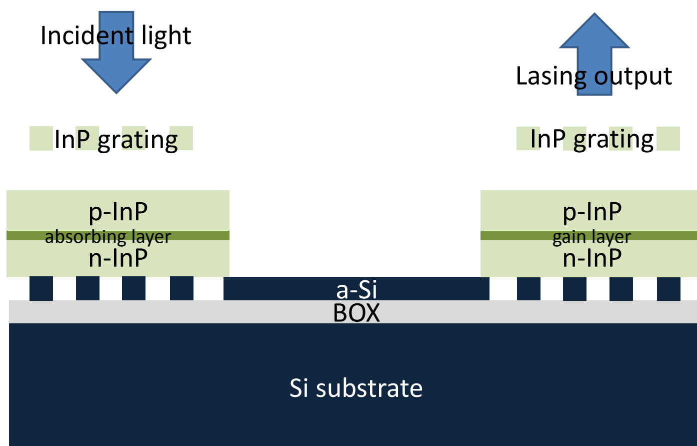

Figure 1.1: Schematic of the bidirectional transceiver system.

Silicon detectors Normally, Si is transparent in the 1300-1500 nm operating wavelength. Therefore, it is not a suitable material for fiber-optic communica-

tion. Usually, Si has strong absorption at the wavelength below 1000 nm. It is excellent for using in applications such as biomedical devices and space imaging.

Ge-on-Si A novel approach for light detection at 1550 nm communication wavelength using Ge has been proposed, developed, and manufactured. Ge is known to have high compatibility with Si processing. Because Ge has a smaller bandgap than Si, it exhibits strong absorption at the wavelength of interest. Although, Ge is more compatible with Si than III-V semiconductors, good quality Ge growth on Si requires high temperature processing (> 700 °C). This high temperature processing can cause difficulty in integrating with growth sequences. [21].

III-V epitaxial grown on Si Another approach is the direct growth of a III-V epitaxial structure on Si. The lattice mismatches of GaAs and InP on Si are 4.1% and 8.1%, respectively. In addition, the thermal expansion coefficient mismatches of GaAs and InP on Si are 120.4% and 76.9%, respectively [22]. These mismatches result in severe dislocation during growth. Many methods to reduce dislocation have been proposed but the dislocation density in a III-V epitaxial structure grown on a Si wafer is still two order of magnitude higher than that in a III-V epitaxial structure grown on a III-V wafer.

III-V bonded on SOI The last approach is combining a silicon-on-insulator (SOI) with III-V material using bonding technologies. Many low temperature bonding techniques have been proposed and developed in recent years. With this approach, the device can be integrated on chip and no accurate alignment is required [23, 24]. By using plasma-assisted bonding technique, the devices have been demonstrated on 150-mm SOI wafers [25, 26]. This is a promising approach to integrating light sources and detectors on the same platform.

In this work, the III-V/SOI platform is pursued. The hybrid III-V on SOI would allow us to create both high efficiency light source and receiver at the same time which could reduce production cost. Utilizing the grating structure allows us to directly bonded the active material to the silicon platform. A high thermal conductivity of the silicon is useful to dissipate heat during light emission and receiving. Buried oxide underneath the silicon is a requisite to create a high reflective mirror from the grating structure. It can serve as a protective layer and acts as a cladding layer for an optical waveguide. An example of a bidirectional optical transceiver which utilizes grating structures is shown in Fig. 1.1.

1.4 Thesis outline

This thesis discusses the work on designing and developing a processing flow of the tunable RCE photodetector by using the dielectric subwavelength gratings for 1550 nm communication wavelength on SOI platform. The grating serves as a surface-normal broadband highly reflective mirror. This grating replaces the conventional DBR used in typical resonant cavity structures. Different resonant cavity types are proposed and studied. The device operates under TM-polarized light incident.

Chapter 2 provides a background and properties of dielectric subwavelength gratings including HCG and HG as highly reflective mirrors.

Chapter 3 studies different cavity type of the tunable RCE photodetector with the HCG and HG reflectors. The chapter divided into two main sections, the HCG based RCE photodetector and the combined HG/HCG RCE photodetector. Simulation results regarding tunability, detection linewidth, and quantum efficiency of different types of optical cavities will be provided.

Chapter 4 describes the realization of the chosen tunable RCE photodetector structure which is the HG/HCG RCE photodetector. The content consists of the main processing flow and short processing tests to develop the process parameters.

Chapter 5 presents the measurement results of the fabricated devices.

Chapter 6 concludes and summarizes findings in this thesis.

Chapter 2

Dielectric Subwavelength Gratings (SWGs)

2.1 Introduction

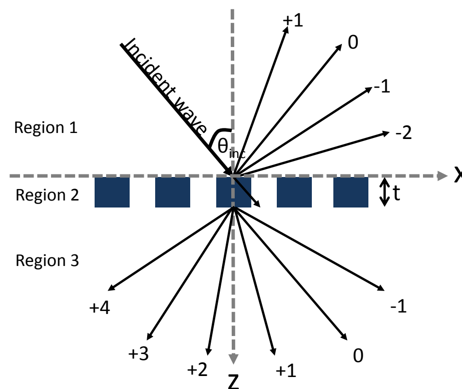

Figure 2.1: Geometry of a planar diffraction grating

One dimensional diffraction gratings are periodic structures that have pitches comparable to the wavelength of an incident wave as shown in Fig. 3.17. The

incident wave creates diffracted forward and backward propagating waves in the region 3 and region 1, respectively. The field propagating through the grating is disturbed and the phase is shifting as a result of modulated relative permittivity (dielectric constant). The outgoing wave of a near field region, therefore, is modulated and has the same periodicity as the grating. For dielectric media, the grating relative permittivity function, $\epsilon_r(\vec{r})$ can be described as [27]

$$\varepsilon_r(\vec{r}) = \varepsilon_{r,eff} + \Delta\epsilon\cos(\vec{K}\cdot\vec{r}) \tag{2.1}$$

where $\varepsilon_{r,eff}$ is the average of the dielectric constants of the grating bar and air. $\Delta\epsilon$ is half of the difference of the dielectric constants of a grating bar and air. $\vec{K}$ is the grating wave vector equals to $2\pi/\Lambda$ where Λ is the grating period. The incident wave, E_{inc} can be assumed as a plane wave:

$$E_{inc} = \exp(-\jmath\vec{k}_{inc}\cdot\vec{r}) \tag{2.2}$$

where $\vec{k}_{inc}$, the incident wave vector is $2\pi n_{inc}/\lambda_0$; n_{inc} is the refractive index of the incident medium and λ_0 is the free space wavelength. As a result of Floquet theorem, the wave vector of i-th diffracted order, $\vec{k}_i$, can be written as:

$$\vec{k}_i = \vec{k}_{inc} - i\vec{K}. \tag{2.3}$$

Eq. 2.3 can be rewritten in the form of a general grating equation:

$$n_{eff}\sin\theta_i = n_{inc}\sin\theta_{inc} - i\frac{\lambda_0}{\Lambda} \tag{2.4}$$

where θ_i is the refracted angle of each diffracted mode and θ_{inc} is the angle of incidence. For subwavelength regime, only 0th order diffraction is of interest. Therefore, we can develop a condition by setting $i = 1$. Under normal incidence, $n_{inc}\sin\theta_{inc} = 0$ and $\sin\theta_i$ is maximum at 1. The condition becomes:

$$1 > n_{eff}\frac{\Lambda}{\lambda_0} \tag{2.5}$$

Assuming a transverse electric (TE) field is incident on the grating, the diffracted field in region 1 can be written as:

$$E_1 = E_{inc} + \sum_i R_i\exp(-\jmath\vec{k}_{1i}\cdot\vec{r}) \tag{2.6}$$

where R_i is the normalized amplitude of the i-th reflected wave. In region 2 and 3, the modulated electric field can also be expressed as:

$$E_2 = \sum_i S_i(z) \exp(-\jmath \vec{k}_{2i} \cdot \vec{r}) \tag{2.7}$$

$$E_3 = \sum_i T_i \exp[-\jmath \vec{k}_{3i} \cdot (\vec{r} - t\hat{z})] \tag{2.8}$$

where $S_i(z)$ is the normalized amplitude of the i-th harmonic field in the grating region, T_i is the normalized amplitude of the transmitted wave, and k_{ji} is the x-component wave vector of the i-the harmonics in region j.

To obtain the diffracted amplitude, $S_i(z)$, Eqs. 2.1 and 2.7 are substituted into the wave equation:

$$\nabla^2 E_2 + k_0^2 \varepsilon(x, z) E_2 = 0 \tag{2.9}$$

resulting in an infinite set of coupled-wave equations where k_0 is the free space wave vector. After solving the system of differential equations, a solution can be written in a form of eigenvalues and eigenvectors. By matching the boundary conditions of the tangential electric and magnetic fields at z=0 and z=t, R_i and T_i can be determined. The described procedure to analyze the planar diffraction gratings is referred to as rigorous couple-wave analysis (RCWA) which has been proposed by Moharam in 1981 [28]. It is the chosen method to analyse the grating in this work. The RCWA software used in this thesis is python-based CAMFR [29] and Matlab-based rcwa-1d [30]. CAMFR was used to efficiently calculate reflection and transmission coefficients. While, rcwa-1d was mainly used to plot the field profiles. To accurately model the grating, a convergence test was done on both software. Fig. 2.2 shows rcwa1d converges faster than CAMFR and solutions from both softwares agree well up to 4 decimal places when the number of modes is 61. Therefore, the author used this number as a default value to model the gratings in this thesis.

2.2 Subwavelength High Contrast Grating (HCG)

A type of subwavelength grating which referred to as high contrast grating (HCG) has been proposed by Chang-Hasnain et al. in 2004 [15, 31]. The HCG

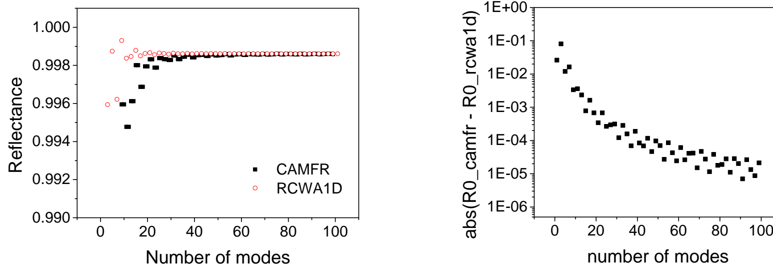

Figure 2.2: (a) Modes convergence of a CAMFR and rcwa1d. (b) Absolute values of the reflectance difference calculated by CAMFR and rcwa1d under TM-light incidence.

is a single layer dielectric subwavelength grating where the refractive index difference between the grating and its surrounding materials is high. HCGs have many interesting properties including surface normal broadband high reflectivity (e.g., 99.9% over 100 nm), high quality factor resonance ($> 10^7$), capability of transverse mode control. The HCGs have gained popularity in recent years. Due to its outstanding properties and ease of fabrication, many optoelectronic devices and applications have been proposed and demonstrated [32–40].

In this section, the theory of HCG and its properties as a broadband reflector are briefly reviewed, which has been used for theoretical and numerical studies in this thesis.

2.2.1 Theory of HCG as Broadband reflector

Chang-Hasnain et al. have proposed a theoretical model to explain broadband reflective and high-Q resonator properties of the HCGs [41–43]. The physics of the HCG has been explained that as the plane wave incidents on the grating, a few waveguide array modes are excited depending on the wavelength and the grating dimensions. However, because of the large index difference, only two modes have real propagation constant in z-direction defined in Fig. 2.3. The two modes with real propagation constants propagate to the exit plane, accumulating the phase change. At the exit plane, they reflect back and couple into each other. Same mode couplings occur again when the modes travel back and reach the input plane. Because the HCG period is shorter than the incident wavelength and the input and output media have low refractive indices, only the 0th order diffraction carries energy for reflection and transmission. The reflection process in HCGs can be explained with a picture of guided-mode

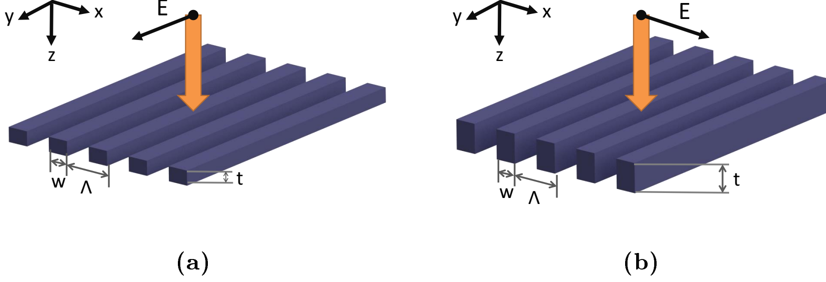

Figure 2.3: Schematic of the (a) TE polarized and (b) TM polarized subwavelength HCG where Λ = grating period, w = grating width, and t=grating thickness. The black arrow represents the electric field polarization direction and the orange arrow is the light propagation direction.

resonance (GMR) [44–46]. Under GMR condition with n_{ex}=refractive index of exiting material and n_g=refractive index of grating,

$$max(n_{inc}, n_{ex}) \leq \left| n_{inc} \sin\theta_{inc} - i\frac{\lambda_0}{\Lambda} \right| < n_g \tag{2.10}$$

an incident plane wave couples to leaky waveguide modes in the grating. For the HCG which operates, depending on the grating parameters, the resonance of two counter propagating waveguide modes take place either in phase or out of phase which results in either enhancement or inhibiting the radiation.

2.2.2 Properties of HCG reflectors

HCGs are polarization sensitive by nature. The HCG can be designed to be highly reflective to either TE- or TM-polarized incident fields. In this thesis, the HCG that is highly reflective to TE- and TM-polarized incident fields are referred to as TE-HCG (c.f. Fig. 2.3a) and TM-HCG (c.f. Fig. 2.3b), respectively.

Figure. 2.4 shows an example of the 0th-order reflectance and transmittance of the TM-HCG at normal incidence, in which the incident and exiting materials are SiO_2 and the grating is made of Si. To design the HCG with broadband

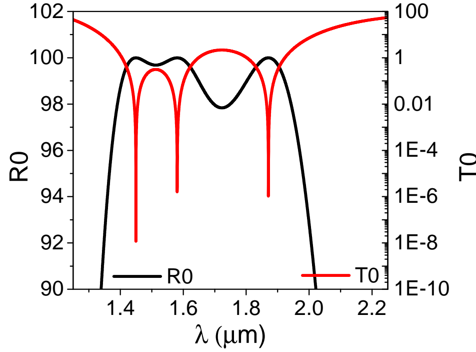

Figure 2.4: Reflectance in linear scale and transmittance in logarithmic scale of a TM HCG with grating parameters: $n_L = 1$, $n_H = 3.47$, $n_{inc} = n_{ex} = 1.47$, $\Lambda = 750nm$, $DC = 0.63$, $t_{HCG} = 500nm$

high reflectivity, important design parameters, i.e., grating period, Λ, grating thickness, t, and duty cycle (DC) or filling ratio need to be well engineered. In this example, the bandwidth in which the 0th-order reflectance, R_0, is higher than 90% is 682.2 nm. When we look at the higher reflectance of $R_0 > 99\%$, there are two bandwidth ranges, one from 1405.4 nm to 1648.4 nm and the other from 1802.2 nm to 1922.8 nm. In light of the GMR theory, we can explain that this broadband property of the grating is attributed to 3 resonances at 1448 nm, 1588 nm, and 1876 nm which correspond to the 0th, 1st, and 2nd diffraction orders, respectively. Three dips in the transmittance spectrum are related to these resonances.

TE-HCG vs TM-HCG vs DBR Broadband mirrors with very high reflectivity find their applications in optoelectronics devices. The simplest form of broadband mirror is a thin metal film. However, due to its high absorption at our wavelength of interest, 1.55 μm, the reflectivity cannot be achieved higher than 99%. Distributed Bragg mirrors (DBRs) have been used as an ultra high reflectivity broadband mirror for years. By alternating layers of two different materials with an optical thickness equal to 1/4 of the wavelength, the reflected components from interfaces interfere constructively, resulting in a high reflectance. The reflectivity of the DBRs depends on the refractive index difference of the two materials and the number of repeated pairs. The bandwidth of the DBRs also is strongly proportional to the refractive index difference. However, for a III-V material system, it is difficult to find a lattice-matched material with the large index difference. One of the preferred choices of materials for DBRs on III-V platform are AlGaAs/GaAs with a refractive index

difference of approximately 0.5.

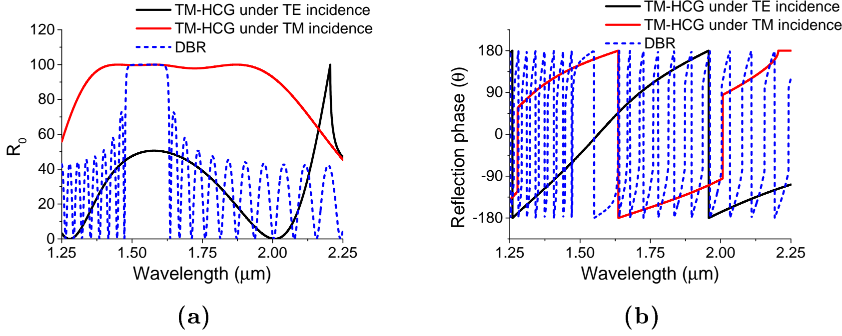

Figure 2.5: (a) Reflectance and (b) phase plot of a HCG with n_L=1, n_H = 3.47, n_{inc} = n_{ex} = 1.47, Λ=750 nm, DC=0.63, t_{HCG}=500 nm under TE (solid black) and TM (solid red) polarized light in comparison with 36-pair $Al_{0.9}Ga_{0.1}As/GaAs$ DBR (blue dashed).

As seen in Fig. 2.5, with 36 pairs of $Al_{0.9}Ga_{0.1}As/GaAs$ DBR, the reflectivity at 1.55 μm is 99.98%. The bandwidth with a reflectivity higher than 99 % is 129.7 nm. The TM-HCG, on the other hand, under TM polarized light incidence has the bandwidth as broad as 243 nm. The graph also shows the polarization sensitive property of the HCG. The reflectance of the same grating under the TE-polarized light incidence is less than 50% over 1 μm wavelength range. It is worth mentioning that one cycle of the reflection phase shift of the HCG covers over 697.8 nm, while the DBR covers only 169.4 nm. In theory, this range of the reflection phase could limit the tuning range of the resonant devices. However, in practice, the tuning range is limited by the reflectance spectrum because low reflectance region, $<$ 90%, drastically reduces the resonant field amplitude. Even though, the reflectance of this HCG under TE-polarized light incidence reaches almost 50% at 1.55 μm, the reflection phase shift of the TE-polarized wave differs by π from the TM-polarized wave. Therefore, if the resonant cavity designs to resonate the TM wave, the TE wave will be off resonance. In this thesis, TM-HCG is the only structure of interest which will be analysed and fabricated.

HCG thickness vs wavelength One interesting property of the HCG is its scalability with wavelength [47]. The reflectance and transmittance spectra of the HCG with specific grating parameters Λ, DC, and t would be identical to another HCG with grating parameters of $2 \times \Lambda$, DC, and $2 \times t$ at a wavelength range scaled by a factor of 2. Therefore, the HCG can be designed to operate in

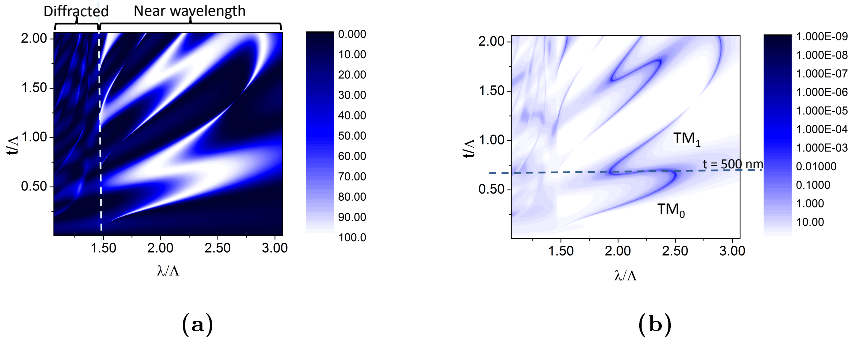

(a) (b)

Figure 2.6: (a) Reflectance in linear scale and (b) transmittance contour in logarithmic scale of a TM HCG as a function of wavelength and grating thickness. The figure illustrates diffracted regime and near-wavelength regime. The 1st order diffraction cutoff line is marked (vertical dash line) in (a) and the broadband highly reflective mirror thickness is marked (horizontal dash line) in (b).

a specific wavelength range and scaled to another range of interest by scaling the structure by a factor of wavelength ratio. Therefore, we can draw a reflectance and transmittance contour map of any HCG by normalizing the wavelength and grating thickness, t, over the grating period, Λ. Fig. 2.6 is the contour plot of the surface-normal incident TM polarized wave onto the HCG. The diffraction regime is clearly seen at $\frac{\lambda}{\Lambda} < 1.47$ which corresponds to the refractive index of the incident and exiting media. When the higher order diffraction emerges, the reflectivity of the 0th-order is reduced. In the near subwavelength regime, the S-shaped high reflection patterns are observed. The HCG reflectivity pattern evolves from narrowband reflection to broadband reflection and back to narrowband as the grating thickness increases. It is explained by Shokooh-Saremi et al. [48] that for the broadest reflection band, TM_0 is the main excited mode. As the grating thickness increases, higher order modes are allowed. These high order modes play a role to excite the grating. The Bloch mode theorem explains the broadband reflection occurs where there are weak coupling of the simultaneous Fabry-Perot resonances of two array waveguide modes. The narrowband reflectivity, on the other hand, indicates strong coupling. As the grating thickness further increases, the second order resonance emerges. As a result, another S-shaped high reflection area comes up. However, the bandwidth of the second order resonance is narrower than the first one.

The field intensity profiles of the HCG considered for Fig. 2.4 and 2.5a at the non-resonant wavelength, 1.52 μm, and 3 leaky-mode resonant wavelengths of 1.448 μm, 1.588 μm, and 1.876 μm inside the grating are shown in Fig. 2.7.

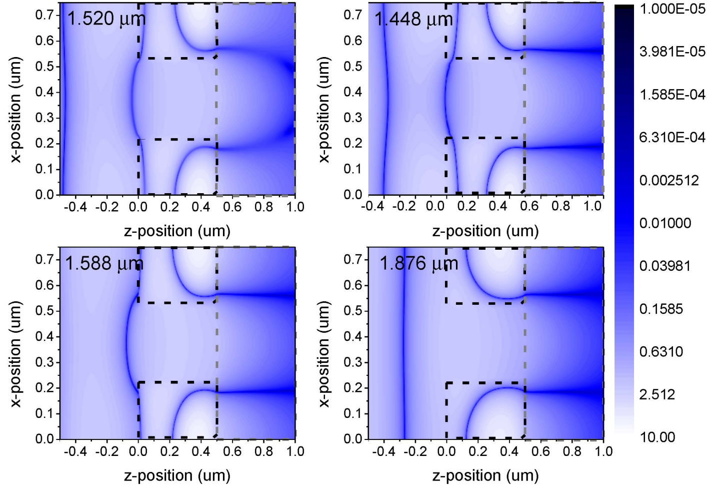

Figure 2.7: $|H_y|$ field component of the HCG considered for Figs. 2.4 and 2.5a. A TM polarization wave with an amplitude of 1 is incident from the left. The area in the black dashed lines represent the grating bars and the area in the grey dashed lines represent the exiting media.

The incident wave from the left passes through the SiO_2, hits the grating at z = 0 μm, and exits at z = 0.5 μm. The H_y field component shows that the mode is mainly confined within the Si grating. However, the field amplitudes are low because of the weak coupling of the two waveguide-array modes. The transmission power was cancelled out causing broadband reflection.

Duty cycle vs wavelength Duty cycle (DC) is defined a ratio of the grating width to the grating period, $\frac{w}{\Lambda}$. It is one of the key design parameters. Under an optimized value of the duty cycle at the certain thickness, the dc Fourier coefficient of the electromagnetic field inside the grating is zero. It is explained by the Bloch mode theorem that the nth Fourier coefficient of the electromagnetic field expansion corresponds to the $\pm nth$-order transmission coefficient. For the HCG, only 0th-order carries power along the z - direction. Thus, only the dc Fourier coefficient influences the output of the grating. Under the destructive interference condition of the two waveguide modes, the dc Fourier coefficient equals to zero, which leads to low transmittance and high reflectance [41]. The change in duty cycle directly affects the modulation of permittivity. So, it determines how the electromagnetic field is disturbed. To design the wideband reflector, the right DC has to be numerically determined. As shown in Fig. 2.8,

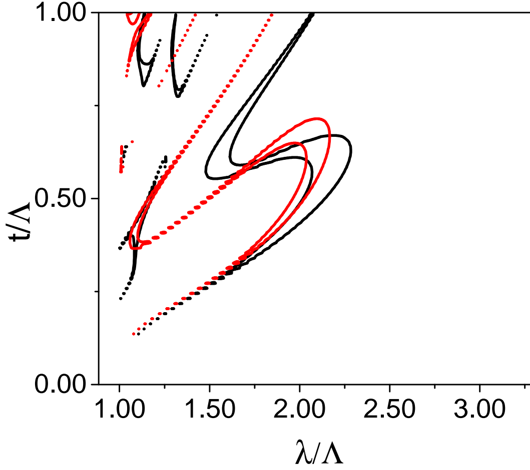

Figure 2.8: Duty cycle contour line at $R_0 = 99\%$ of a InP HCG with air as incident and exiting material and grating parameters: $\Lambda = 735$ nm, w = 365(red) and 515(black) nm, h = 530 nm

the region with constant reflectance, $R_0 = 99\%$, has an S-shaped with different slope for different grating width. Therefore, by varying the DC, we can choose the location and bandwidth of the high reflective regime.

2.3 Subwavelength Hybrid Grating (HG) Reflector

The HCG requires to be surrounded by a low refractive index material. This could be beneficial for some applications such as waveguides and resonators because using air and/or SiO_2 as the low index material can simplify processing. However, for optical device integration on the SOI platform, having low refractive index material between the III-V material and the Si can complicate the processing. Early in 2014, our group proposed a new type of broadband reflector which eliminates the requisite of the low refractive index material [49]. As shown in Fig. 3.12, the new structure consists of a subwavelength grating and a high refractive index cap layer. This cap layer can be thicker than the grating and still exhibits broadband reflectivity. For the HCG structure, two waveguide array modes are allowed to propagate within the grating. These modes interact only with the 0th-order diffraction at the input and output planes. Similar to

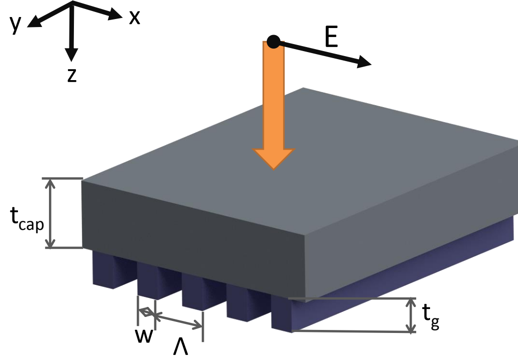

Figure 2.9: Schematic of the TM-HG reflector with the structure parameters : Λ = grating period, w = grating width, t_g=grating thickness, and t_{cap} = cap layer thickness. The black arrow represents the electric field polarization direction and the orange arrow is the light propagation direction.

the HCG, the HG reflector also allows two waveguide array modes in the grating layer. However, when a high refractive index layer is placed on top of the grating, the 1st-order diffraction arises. Therefore, in the cap layer, there are 0th-, 1st-, and -1st-diffraction order that interact with the waveguide modes in the grating. If the input and output media are made of low index materials, the reflection and transmission of this suggested structure would allow only the 0th-diffraction order to transport the energy. Under an optimized parameters, the cancellation of these modes leads to a high and broad reflectivity as observed in the HCG structure.

Important design parameters of the HG reflector are the same as the HCG with an addition of the cap layer thickness, t_{cap}. Figure 2.10 shows the reflectance, transmittance, and reflection phase shift of the HG reflector. The surface-normal TM-polarized light is incident on the HG reflector, where the incident medium is air and exiting medium is SiO_2. The cap layer is made of InP and the grating material is Si. With chosen design parameters, the reflection bandwidth where $R_0 > 99\%$ ranges from 1305.9 nm to 1624.1 nm and from 1675.5 nm to 1737.9 nm. The reflectance dip occurs between 1624.1 nm and 1675.5 nm where the reflectance drops below 99% but still higher than 98% as seen in Fig. 2.10a. There are 4 transmittance dips at 1340.8, 1466.4, 1583.5, and 1719.6 nm in this example. This drop of the transmittance corresponds to 4 resonances of leaky modes. Extra transmittance dip compared to the HCG arises from the resonance of the 1st-order diffraction in the cap layer. Compare to the previous

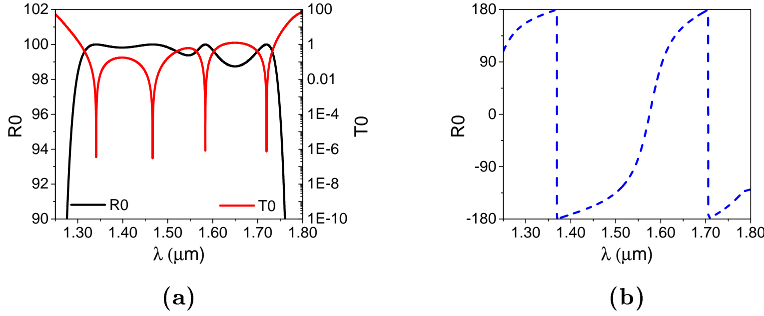

Figure 2.10: (a) Reflectance in linear scale and transmittance in log scale, and (b) reflection phase spectra of the TM HCG with grating parameters: $n_L = 1$, $n_H = 3.47$, $n_{inc} = 1$, $n_{ex} = 1.47$, $n_{cap} = 3.1661$, $\Lambda = 735nm$, $DC = 0.428$, $t_{HCG} = 500nm$,$t_{cap} = 320nm$

example of the HCG where the high reflectance band is 243 nm, the HG reflector in this example has broader high reflectance band of 318.2 nm. One period of the reflection phase shift in Fig. 2.10b of the HG reflector is 336.3 nm which is approximately half of what is observed in the HCG case. The reflection phase slope of the HG reflector around the center wavelength, 1.55 μm, is 3 times steeper than the HCG. However, the reflection phase of the HG reflector is more non-linear than the HCG structure. The reflection phase slope reduces from 37.72 rad/μm at 1.55 μm to 4.53 rad/μm at 1.4 μm.

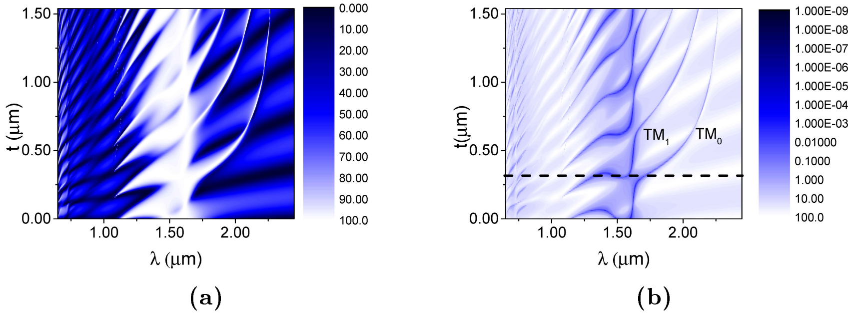

Figure 2.11: (a) Reflectance in linear scale and (b) transmittance in log scale drawn versus the wavelength and the cap layer thickness of a HG reflector with $n_L = 1$, $n_H = 3.47$, $n_{inc} = 1$, $n_{ex} = 1.47$, $\Lambda = 735nm$, $DC = 0.428$, $t_{HCG} = 500nm$.

The reflectance and transmittance contour map as a function of the cap layer

thickness and wavelength in Fig. 2.11 shows more excited modes are introduced as the cap layer thickness increase. It is seen in Fig.2.11b that at the thickness designated by the black dashed line, the reflectance bandwidth is the broadest and at that thickness, there is an overlap between the TM_0 and TM_1 modes. As a result, we can achieve broader highly reflective bandwidth than the HCG structure. The diffracted regime is found where $\lambda < 1.08$ μm.

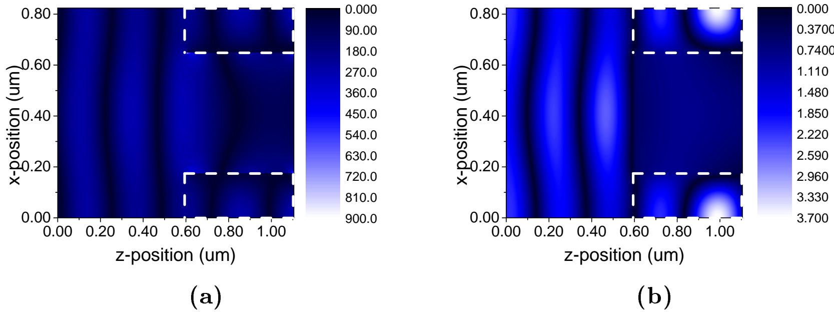

Figure 2.12: (a) E_x and (b) H_y contour plot of a HG reflector with parameters: $n_L = 1$, $n_H = 3.47$, $n_{cap} = 3.1661$, n_{inc}=1, $n_{ex} = 1.47$, $\Lambda = 824nm$, $DC = 0.43$, $t_{HCG} = 500nm$, and $t_{cap} = 605nm$. The region in the white dashed line indicates the grating bars.

We now look at the electromagnetic field profile inside the HG reflector. The TM-polarized light is incident from the left hitting the cap layer at z=0. The wave transmits through the grating at z=0.605 and exits the grating to the SiO_2 at z=1.105 as shown in Fig. 2.12. The wave inside the cap layer is disturbed and modulated due to the effect of the 1st-order diffraction. Similar to the HCG, the mode is strongly confined within the grating material. Fig. 2.12a shows how the plane wave is modulated inside the grating.

2.4 Summary

So far, we have presented properties of the HCG structure and the novel HG reflector where the additional high index layer is placed on top of the HCG. We showed that even with the addition of high index material, we can find the parameters that give even broader high reflectance band than the HCG. This chapter presents a homogeneous cap layer as an example. In practice, an active material can be placed inside the cap layer and form devices. The next chapter introduces the concept of the resonant cavity devices and simulation

results of resonant cavity enhanced (RCE) photodetector using the HCG and HG structures.

Chapter 3

Tunable Resonant Cavity Enhanced (RCE) Photodetector Design

As described in chapter 2, the HCG and HG reflectors provide broader highly reflective band than conventional distributed Bragg reflectors (DBRs). This chapter presents tunable RCE photodetectors which incorporate the HCGs and HG reflectors. The first section introduces a general theory of RCE photodetectors. The second section presents different types of cavity design and study tuning properties of each type of cavities with HCGs as the mirrors. The third section proposes three cavity designs including air coupled cavity (ACC), semiconductor coupled cavity (SCC), and extended cavity (EC). Numerical results show that the ACC configuration provides the broadest tuning range with the highest tuning efficiency around the centre wavelength. Third, we propose a novel tunable RCE photodetector with the HCG and HG reflector where an absorbing layer is included in a cap layer. The structure is numerically investigated. Results show similar tuning properties with the HCG structures and better tuning efficiency. In addition, the HG-HCG structure simplifies the fabrication by removing a need of a low refractive index layer. Therefore, we decided to fabricate the HG-HCG structure in later chapters.

3.1 Resonant Cavity Design

To design and understand the RCE photodetector, analytical models have been developed to describe the behaviour of an absorbing layer inside a Fabry-Perot resonator [10, 50, 51]. While analytical formulas provide intuitive results and understanding of how the parameters affect the device performances, numerical simulation is crucial to accurately model the devices. In the next section, we present the analytical expression to calculate a free spectral range (FSR), effective optical length (L_{eff}), cavity finesses (F), quantum efficiency (η), effective absorption coefficient (α_{eff}), and device time constants.

3.1.1 Theory of RCE photodetectors

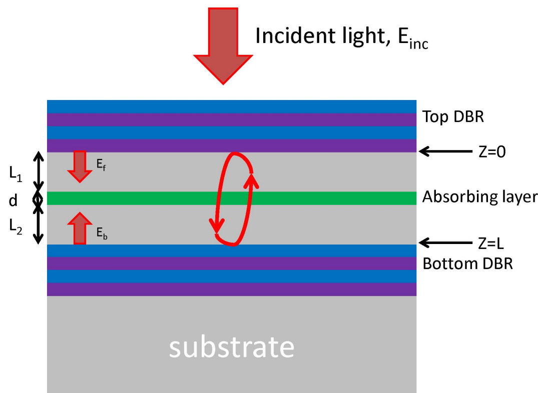

Figure 3.1: Schematic of a resonant cavity enhanced device.

The RCE photodetector is a photodiode placed inside a Fabry-Perot elaton cavity. As shown in Fig. 3.1, the RCE photodetector structure is similar to a vertical cavity laser structure. The top and bottom mirrors that form the resonant cavity are usually employed the DBRs which consist of alternating layers of low and high refractive index materials. For a normal incident beam from the top, E_{inc}, the complex transmission coefficient equals t_1. The reflection coefficient of the top and bottom mirrors are $r_{1,2} = |r_{1,2}|e^{-\jmath\phi_{1,2}}$. A pictorial representation of the wave propagation function which applies a technique from control system engineering called the block diagram can visualize the signal flow inside the cavity as shown in Fig. 3.2.

The block diagram represents a positive feedback of the cavity. Thus, we may

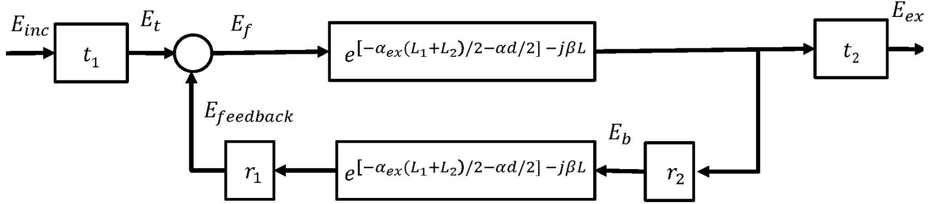

Figure 3.2: The block diagram of the RCE detectors.

express the transmitted propagating field at z = 0 as

$$E_t = t_1 E_{inc} \tag{3.1}$$

and the feedback propagating field as

$$E_{feedback} = r_1 r_2 e^{-\alpha_{ex}(L_1+L_2)-\alpha d-2\jmath\beta L} E_f \tag{3.2}$$

where α is the absorption coefficient of the active layer, α_{ex} is the absorption coefficient of the passive layers, and $\beta = \frac{\omega}{c} = \frac{2\pi n}{\lambda}$ = propagation constant. Note that, in this analytical formula, the refractive indices of all layers are assumed to be the same. The forward propagating field after one round trip, E_f, inside the cavity is

$$E_f = E_t + E_{feedback} = t_1 E_{inc} + r_1 r_2 e^{-\alpha_{ex}(L_1+L_2)-\alpha d-2\jmath\beta L} E_f \tag{3.3}$$

Eq. 3.3 can be rearranged to

$$\frac{E_f}{E_{inc}} = \frac{t_1}{1 - r_1 r_2 e^{\alpha_{ex}(L_1+L_2)-\alpha d-2\jmath\beta L}} \tag{3.4}$$

This equation tells us that the strongest resonance occurs when a round-trip phase shift equals an integer multiple of 2π with minimum absorption in the optical path. If there is absorption within the cavity, the E_f would be maximum when the denominator approaches 0.

The backward travelling field at $z = L, E_b$, could be expressed as a function of E_f

$$E_b = r_2 e^{-\alpha_{ex}(L_1+L_2)/2-\alpha d/2-\jmath\beta L} E_f \tag{3.5}$$

We could also write the transfer function of the cavity as

$$H = \frac{E_{ex}}{E_{inc}} = -\frac{t_1 t_2 e^{[-\alpha_{ex}(L_1+L_2)/2-\alpha d/2]-\jmath\beta L}}{1 - r_1 r_2 e^{-\alpha_{ex}(L_1+L_2)-\alpha d-2\jmath\beta L}} \tag{3.6}$$

Free Spectral Range (FSR), Effective Optical Length, and Finesse
The term Free Spectral Range (FSR) refers to the wavelength spacing between two resonant peaks. When the length of the optical cavity is much longer than the half of the wavelength, $\frac{\lambda}{2}$, more than one axial mode exists. The FSR can be expressed as [10]

$$FSR = \frac{\lambda^2}{2(n_{eff,cav}L + n_{eff,1}L_{eff,1} + n_{eff,2}L_{eff,2})} \tag{3.7}$$

where n_{eff}, i denotes the effective refractive index of the i-th layer and $L_{eff,i}$ is an effective optical length of the i-th mirror which is generally defined as

$$L_{eff,i} = \frac{1}{2}\frac{\partial\phi_i}{\partial\beta}, (i = 1, 2) \tag{3.8}$$

where ϕ_i is the reflection phase of the i-th mirror. The cavity finesse refers to the ratio of the FSR to the full width at half maximum of the linewidth, $\Delta\lambda_{1/2}$, and is given by

$$F = \frac{FSR}{\Delta\lambda_{1/2}} = \pi\frac{\sqrt{r_1 r_2 e^{-\alpha_{ex}(L_1+L_2)-\alpha d-2\jmath\beta L}}}{1 - r_1 r_2 e^{-\alpha_{ex}(L_1+L_2)-\alpha d-2\jmath\beta L}} \tag{3.9}$$

Quantum Efficiency One of the key parameters for the design parameter of the RCE photodetector is the amount of power absorbs in the absorbing layer. The time-average energy density inside the optical cavity is given by

$$P = \frac{n^2 \varepsilon_0}{2} |E|^2 \tag{3.10}$$

and the quantum efficiency, η, of a photodetector is defined as a ratio of the absorbed power, P_a, over the incident power, P_i. Neglecting a standing wave effect, we can write the power absorbed in the active layer as a summation of the forward and backward propagating powers.

$$\begin{aligned} P_a &= (P_f e^{-\alpha_{ex} L_1} + P_b e^{-\alpha_{ex} L_2})(1 - e^{-\alpha d}) \\ &= (P_f e^{-\alpha_{ex} L_1} + r_2^2 e^{-\alpha_{ex}(L_1+L_2) - \alpha d - \jmath \beta L} e^{-\alpha_{ex} L_2} P_f)(1 - e^{-\alpha d}) \\ &= \frac{(1 - r_1^2)(e^{-\alpha_{ex} L_1} + r_2^2 e^{-\alpha_{ex} L_2} e^{-\alpha_c L - \jmath \beta L})(1 - e^{-\alpha d})}{|1 - r_1 r_2 e^{-\alpha_{ex}(L_1+L_2) - 2\jmath \beta L}|^2} P_i \end{aligned}$$

Thus, the quantum efficiency, η, is expressed by

$$\eta = \frac{P_a}{P_i} = \frac{(e^{-\alpha_{ex} L_1} + R_2^2 e^{-\alpha_{ex} L_2} e^{-\alpha_c L})}{1 - 2\sqrt{R_1 R_2} e^{\alpha_{ex} L} cos(2\beta L + \phi_1 + \phi_2) + R_1 R_2 e^{-2\alpha_c L}} (1 - R_1)(1 - e^{-\alpha d}) \tag{3.11}$$

where

$$\alpha_c = \frac{\alpha_{ex} L_1 + \alpha_{ex} L_2 + \alpha d}{L} \tag{3.12}$$

At resonant condition, $2\beta L + \phi_1 + \phi_2 = 2m\pi$, the quantum efficiency is greatly enhanced and Eq. 3.11 is reduced to

$$\eta_{max} = \frac{(e^{-\alpha_{ex} L_1} + R_2^2 e^{-\alpha_{ex} L_2} e^{-\alpha_c L})}{1 - 2\sqrt{R_1 R_2} e^{\alpha_{ex} L} + R_1 R_2 e^{-2\alpha_c L}} (1 - R_1)(1 - e^{-\alpha d}) \tag{3.13}$$

Standing Wave Effect A standing wave is a periodic pattern arises when two counter-propagating waves interfere with each other. Because the RCE photodetectors usually incorporate an active layer which is much thinner than

the standing wave period, the quantum efficiency of the RCE photodetectors is influenced greatly by the position of the absorbing layer in the cavity. To calculate a quantum efficiency of the device, an effective absorption coefficient, α_{eff}, is introduced to either enhance or decrease the standing wave effect depending on locations within the field. From the weighted average definition, we can write the effective absorption coefficient as [52]

$$\begin{aligned}\alpha_{eff} &= \frac{\int E^* \alpha E dz}{\int |E|^2 dz} \\ &= \frac{\int \alpha(z)|E_f + E_b|^2(z,\lambda)dz}{\int |E_{T,f}(z,\lambda)|^2 + |E_{T,b}(z,\lambda)|^2 dz}\end{aligned}$$

where the subscript T refers to the transverse component.

Speed Response A key advantage of the RCE detector is its high speed response that is attributed to the thin absorbing layer. For a simple photodetector, the device speed is limited by the transit time of the photocurrent, the device RC time constant and carrier trapping at heterojunction boundaries. The response time due to the photocurrent is determined by two factors, drift and diffusion of the carriers. The drift transit time of the carrier generated within the depletion region is given by

$$\tau_{tr} = \frac{W}{\nu_d} \tag{3.14}$$

where W is the depletion width and ν_d is the carrier drift velocity. The diffusion time of the carrier generated outside the depletion region is relatively slow compared to the drift process. It is given by

$$\tau_{diff} = \frac{W^2}{2D_p} \tag{3.15}$$

where W is the thickness of the highly doped region and D_p is the diffusion time constant. The diffusion current will be collected at the terminal only when the carriers diffuse into the depletion region. Hence, the diffusion length can be minimized by increasing doping in the contact region. In addition to the carrier transit time, the charging/discharging of an intrinsic layer plays an important

role in overall device speed. The transient time response of the device is given by

$$\tau_{RC} = (R_s + R_d)C_d = \frac{1}{2\pi f_c} \tag{3.16}$$

where R_s is the diode series resistance, R_L is the load impedance outside the photodiode, and C_d is the capacitance across the depletion layer.

The carrier trapping will not occur if a homojunction absorbing layer is employed. Even if the heterojunction is used, the effect can be minimized by using a grading layer. For a high speed device, the intrinsic region needs to be thin to keep the carrier time constant small. However, it should not be too thin such that the diode capacitance becomes too large as shown in Fig. 3.3.

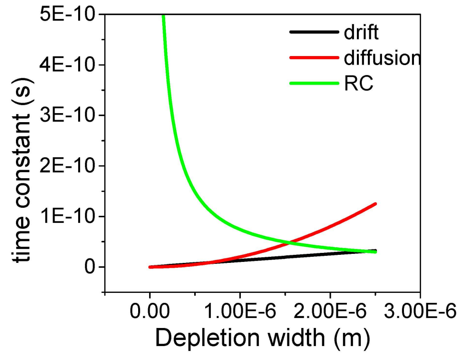

Figure 3.3: Time constants as a function of a depletion width with InGaAs as an active layer, the device area of 40μm$\times$ 40μm, and series resistance of 400 ohm.

3.1.2 Tunable RCE with HCGs

As previously mentioned, the resonant condition of the Fabry-Perot cavity satisfies when the round trip phase equals to $2\pi m$,

$$2\frac{2\pi n}{\lambda}L + \phi_1 + \phi_2 = 2\pi m \tag{3.17}$$

Eq. 3.17 tells us that to change the resonant wavelength, we can change either the refractive index (n), cavity length (L), or the mirror reflection phase shift

(ϕ_i). A popular technique to change the refractive indices of the optical cavity is done through thermal tuning [53]. However, this tuning method is slow, the tuning range is narrow, and an additional heating element is required to heat up the device. In this work, we choose to modulate the optical cavity length to shift the resonant wavelength. We will later explain that by incorporating a micromachined tuning technique, a broad tuning range can be achieved.

3.1.2.1 Design

In order to control the optical cavity length, either liquid or gas is needed as part of the cavity. By inserting an air gap spacing between the mirror and the photodiode material, the optical cavity can be modulated when one of the mirrors is movable along the z-axis. This combination of an air gap and semiconductor material allows us to form three types of cavities as described in Sugihwo thesis [54], an extended cavity (EC) in Fig. 3.4b, an air coupled cavity (ACC) in Fig. 3.4c, and a semiconductor coupled cavity (SCC) in Fig. 3.4d.

- **Air coupled cavity (ACC)** - In the ACC configuration, the air gap functions as a cavity with thickness of $(\frac{2m+1}{4} + \frac{\phi_{HCG}}{4\pi})\lambda$. Therefore, the reflection phase shift at the air gap/semiconductor cavity interface is shifted by π.
- **Semiconductor coupled cavity (SCC)** - In the SCC configuration, the air gap functions as part of the top mirror with thickness equals to $(\frac{n}{2} + \frac{\phi_{HCG}}{4})\lambda$ and there is no reflection phase shift at the air gap/semiconductor cavity interface.
- **Extended cavity (EC)** - In the EC configuration, an anti-reflection layer is placed between the air gap and the semiconductor cavity region. Therefore, the air gap becomes an integral part of the cavity

The characteristics of each cavity configuration can be understood by looking at the forward and backward propagating waves at the air gap/semiconductor cavity interface as shown in Fig. 3.5. In all cavity configurations, the total reflection at the air gap/semiconductor cavity interface consists of a reflected wave from the air/semiconductor interface and a reflected wave from the mirror. In the ACC configuration, the reflected wave from the mirror has π phase different from the reflected wave at the air/semiconductor interface which results in a destructively interfered of the two reflected waves. The SCC configuration, on the other hand, has both reflected waves in phase. Thus, the two waves are

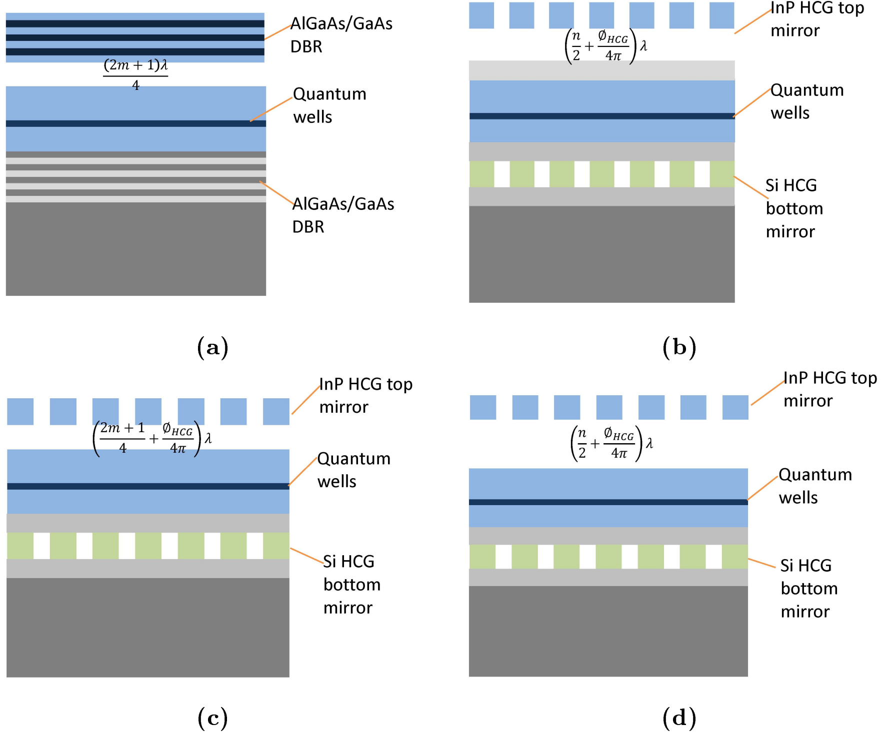

Figure 3.4: (a) Semiconductor coupled Cavity (SCC) with DBRs as the mirros (b) Extended cavity (EC) (c) Air coupled cavity (ACC) (d) Semiconductor coupled cavity (SCC) with HCGs as the mirrors.

constructively interfered. Lastly, in the EC configuration which has an anti-reflection layer between the air gap and the semiconductor cavity, the reflected wave from the air gap/semiconductor cavity interface is suppressed. Only the reflected wave from the mirror contributes to the total reflection. From Fig. 3.5c, 3.5f, 3.5i, assuming the same mirror design, the ACC configuration has a smaller resultant field amplitude than the SCC and EC. In addition, the phase change of the resultant wave between the neutral cavity and the π phase shift mirror with respect to the initial position of the ACC configuration is larger than the SCC design.

To design the tunable RCE photodetector from these cavity configurations,

- First, we need to consider parameters which yield optimal device performance. Mirror reflectivity is known to be one of the most important

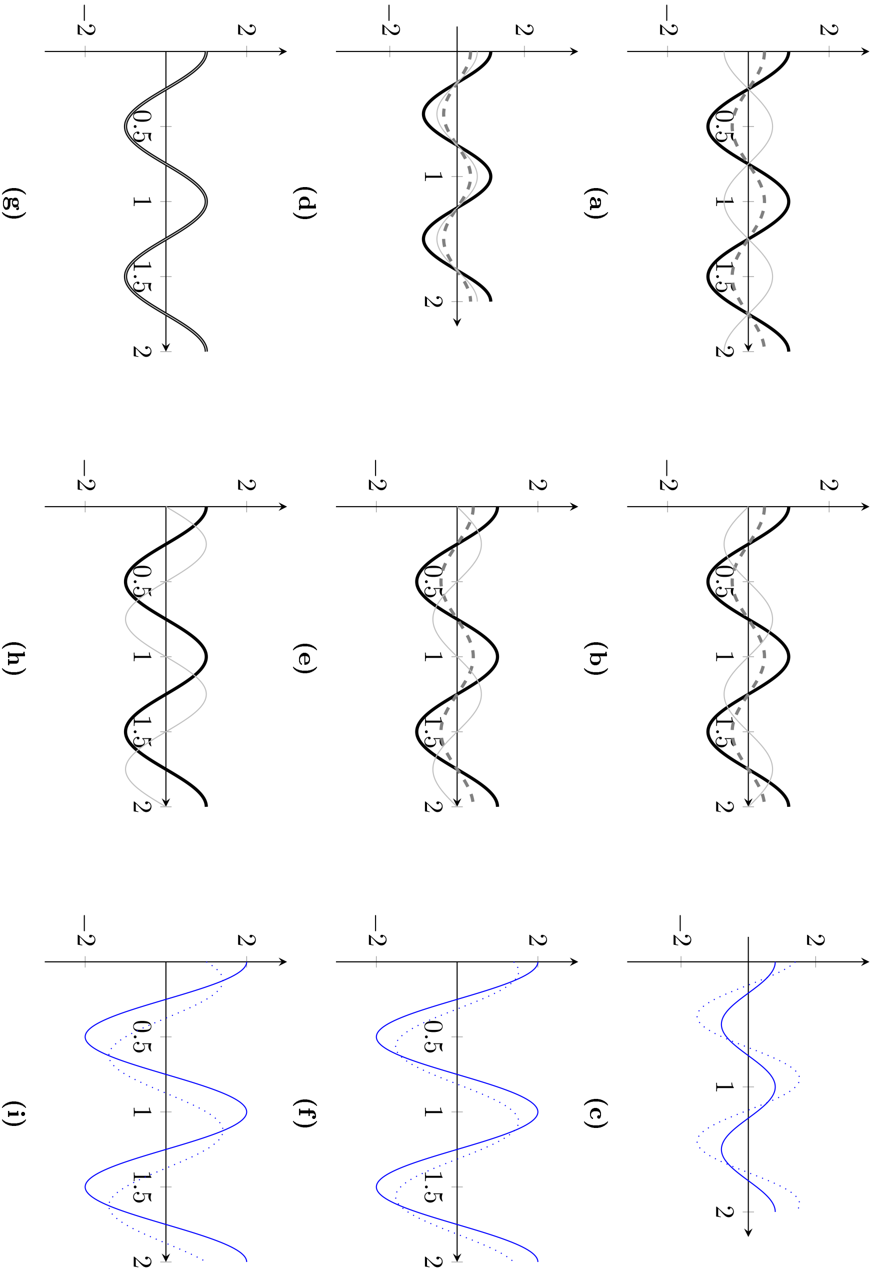

Figure 3.5: Example of wave propagation of (a)-(c) destructive interference, (d)-(f) constructive interference (g)-(i) anti-reflection mirror scheme. (a),(d), (g) represents incident wave (solid black line), reflected wave from the cavity/air gap interface (gray dashed line), and reflected wave from the mirror (light gray solid line) with 0 phase shift. (b), (e), (h) shows the waves when introduce a π phase shift from the mirror. (c), (f), (i) shows resultant wave of the 0 phase shift and π phase shift from the air gap/semiconductor interface.

parameter. To obtain the highest possible quantum efficiency, the mirror reflectivity to which light is incident, R_1, is required to be lower than that of the other mirror, R_2, in accordance with the following equation:

$$R_1 = R_2 e^{-2[\alpha_{ex}(L_1+L_2)+\alpha d]} \quad (3.18)$$

- Next, the field maximum location within the cavity to place the absorbing layer is determined.
- Lastly, the highly doped layers is placed at field minima positions. These high doped layers are used as ohmic contacts and dissipates charges evenly in the lateral direction.

3.1.2.2 Results

Table 3.1: HCG parameters

Mirror Scheme	DC	Λ (μm)	t (μm)
Destructive/top	0.63	0.71	0.48
Constructive/top	0.73	0.84	0.54
AR/top	0.76	0.83	0.53
Constructive/bottom	0.75	0.63	0.5

Following the design rules, four different tunable RCE photodetector structures using the HCGs are prepared for numerical investigations of tuning properties. The epitaxial structure details can be found in appendix B. In the simulation, we compare device performances of each cavity configuration using a double HCG mirror. In addition, to see how these devices perform compared to the traditional RCE photodetector, we use the SCC configuration with two DBRs as a reference design. For ease of explanation, we define the term "mirror reflectivity" here as a reflection at the low refractive index material/semiconductor cavity interface. First, the bottom mirror made of the 500-nm thick HCG with SiO_2 as a surrounding low index material was assumed. By using a constructively interfered mirror scheme, the highest and broadest reflectance achieved was 99.94% under 1550-nm normal incident wavelength. Using this number, we constructed the bottom DBR to achieve similar reflectivity, 99.92%. The HCG top mirror parameters of each configuration were numerically determined to satisfy Eq. 3.18. The HCG parameters for all configurations are shown in table 3.1. The top mirror reflectivity of EC, ACC, and SCC configurations are 99.10%, 98.89%, and 98.94%, respectively.

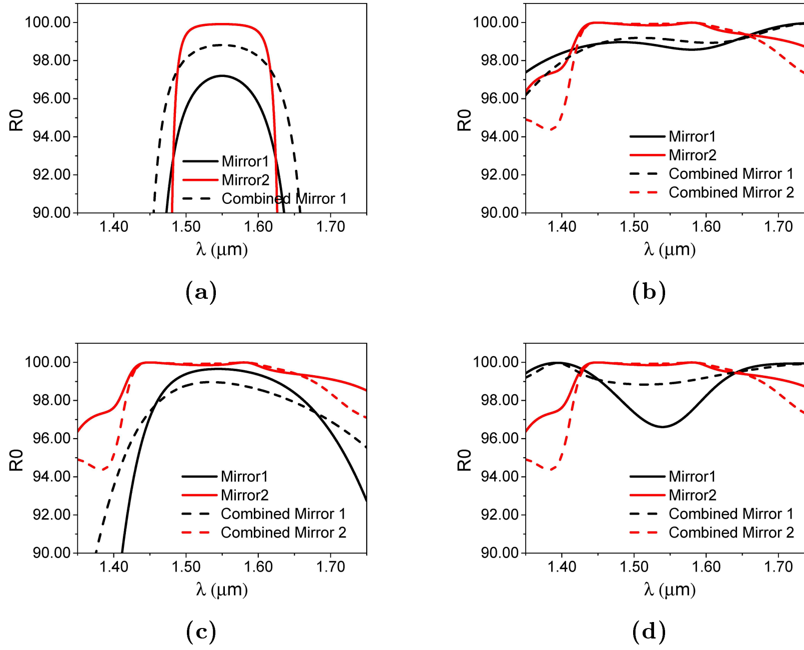

Figure 3.6: Reflectance of (a) SCC with DBRs as the top (black line) and bottom (red line) mirror (b) EC (c) ACC (d) SCC with HCGs as the mirrors. The solid line represents reflectance/transmittance from the HCGs or DBR. The dashed line represents reflectance at the semiconductor cavity/low refractive index material interface.

Fig. 3.6 shows the reflectance of the HCG grating and the combined reflectance at the low refractive index material/semiconductor cavity interface. We can see that for the SCC scheme, the reflectance from the HCG structure at 1550-nm is lower than the reflectance at the air gap/cavity interface. The ACC scheme, on the other hand, has lower reflectance at the interface compared to the reflectance from the grating. This is a result of the constructively and destructively interfered reflected wave as previously explained. It should be noted here that it requires multiple reflections from the destructive interference mirror to reach the target reflectance. In our design, it was calculated that 9 reflections were needed to achieve the target reflectivity. The EC configuration also incorporates a constructively interfered mirror scheme. Hence, the mirror reflectance is higher than the grating reflectance. The region with an ultra high reflectance, $R > 99\%$, for the HCG bottom mirror was 253.8 nm. On the other hand, the reflectance bandwidth of the bottom DBR was 112.4 nm.

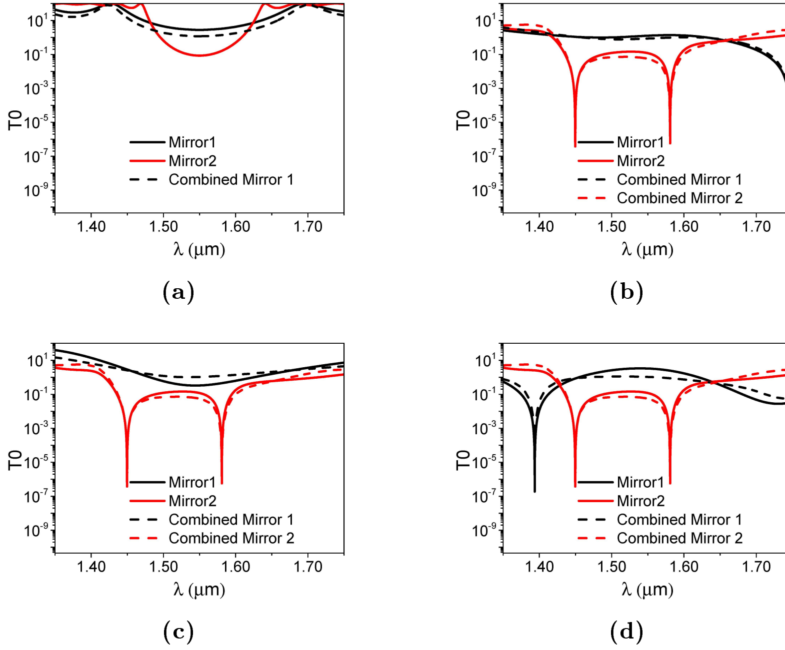

Figure 3.7: Transmittance in log scale of the (a) SCC with DBRs as the top (black line) and bottom (red line) mirror (b) EC (c) ACC (d) SCC with HCGs as the mirrors. The solid line represents reflectance/transmittance from the HCGs or DBR. The dashed line represents transmittance at the semiconductor cavity/low refractive index material interface.

When looking at the transmission plot in Fig. 3.7, for the bottom HCG, the structure was supported by 2 leaky-mode resonances at 1.45 μm and 1.58 μm. While the top mirror of the EC and SCC configuration were supported by the resonances at 1.75 μm and 1.39 μm, respectively. There was no resonance found within the 300 nm range for the ACC top mirror. For the DBR mirror, the lowest transmission is found at the centre wavelength, 1.55 μm. The HCGs, on the other hand, have the transmission dips which can reach 10^{-6}. These transmission plots show that for the highly reflective bottom HCG mirrors, the transmission dips are close to the centre wavelength. On the other hand, the lower reflectance top mirrors have the transmission dips away from the center wavelength.

The reflection phase shift plot in Fig. 3.8 confirms 0 phase shift at the air/cavity interface for the EC and SCC configuration and π phase shift for the ACC config-

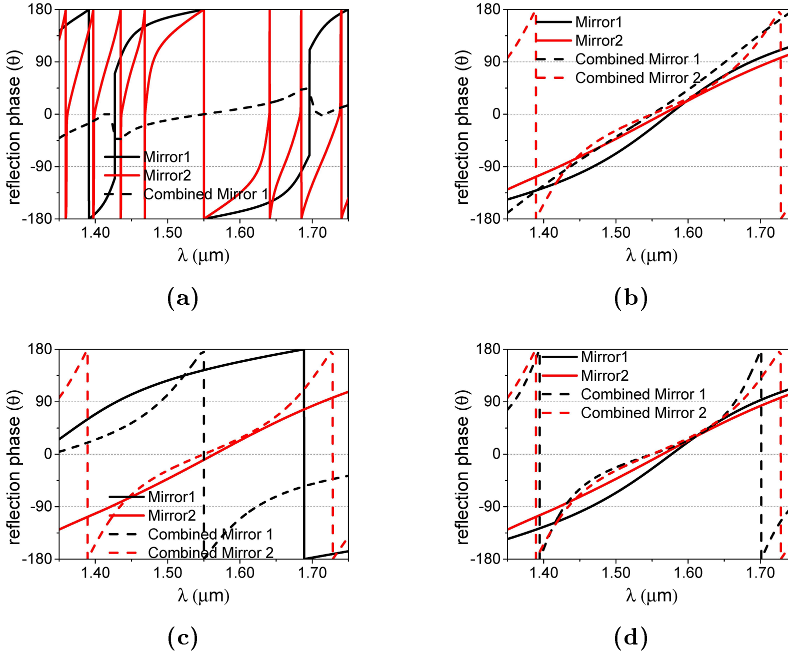

Figure 3.8: Reflection phase shift of the (a) SCC with DBRs as the top (black line) and bottom (red line) mirror (b) EC (c) ACC (d) SCC with HCGs as the mirrors. The solid line represents reflectance/transmittance from the HCGs or DBR. The dashed line represents reflection phase at the semiconductor cavity/low refractive index material interface.

uration. Apart from showing the reflection phase shift at the centre wavelength, the plot shows how the reflection phases were changed for each mirror scheme. For the DBR mirror, the reflection phase was shifted by 180 degree at the air gap/cavity interface. The phase slope defined as, $\frac{d\phi}{d\lambda}$, remains unchanged after added the air gap over a wavelength range of 300 nm. The phase slope of the top DBR is 4.25 rad/μm and the bottom DBR is 3.22 rad/μm at the wavelength of 1.55 μm. For the EC configuration where the AR layer is introduced between the air gap and the cavity, the phase slope between the HCG and the HCG with the air gap changes over the wavelength span. Initially, the reflection phase of the HCG becomes nonlinear around the wavelength shorter than 1.45 μm and above 1.60 μm. After incorporating an air gap spacing of $\frac{\lambda}{2} + \frac{\phi_{HCG}\lambda}{4\pi}$, the reflection phase becomes linear over the entire wavelength span. For the ACC configuration which incorporates the destructively interfered top mirror scheme, the phase slope of the top grating mirror remains the same for the most part.

The reflection phase slope increases a little below 1.45 μm. However, when the destructively interfered mirror scheme was added, the reflection phase slope has changed from 5.51 rad/μm at the grating/air interface to 29.0 rad/μm at the air gap/cavity interface at the wavelength of 1.55 μm. The phase slope decreases as it goes further away from the centre wavelength. At 1.35 μm and 1.75 μm, the reflection phase slope goes down to 6.46 rad/μm and 4.03 rad/μm, respectively. Lastly, the SCC configuration which incorporates the constructively interfered mirror scheme for both the top and bottom mirror, the reflection phase slope at the grating exit plane is steeper than the reflectance at the air gap/cavity interface. The reflection phase slope of the constructively interfered top mirror changes from 15.7 rad/μm at the grating exit plane to 7.43 rad/μm at the air/cavity interface. However, as opposed to the destructively interfered mirror, the phase slope of this combined mirror increases as it goes further away from the centre wavelength. At 1.35 μm and 1.75 μm, the phase slopes of the combined mirror are 24.05 rad/μm and 20.16 rad/μm, respectively. The HCG bottom mirror for three cavity configurations are all the same and have the phase slope of 11.61 rad/μm at the grating exit plane and 9.10 rad/μm at the air gap/cavity interface.

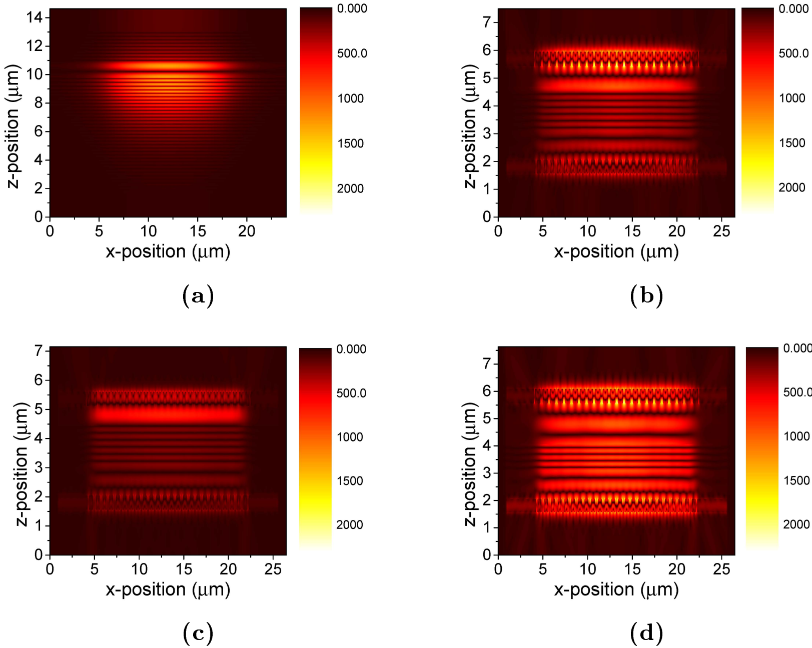

Figure 3.9: $|E_x|$ field component of the (a) SCC with DBRs (b) EC (c) ACC (d) SCC with HCGs as the mirrors.

The electric field profile of the devices is presented in Fig. 3.9. In the EC configuration, the top HCG consists of 22 periods and the bottom HCG has 24 periods. For the ACC configuration, there are 26 top grating periods and 24 bottom grating periods. For the SCC, there are 22 top grating periods and 24 bottom grating periods. As can be seen, the device with two DBRs is much thicker than the devices the double HCG structures. Hence, the DBR-based reference structure has larger modal volume compared to the HCG-based structures. When looking the field intensity, we can see that the SCC configuration yields the highest field intensity follows by the EC and ACC configurations, respectively. It should be noted that the electric field intensity within the air gap spacing of the ACC and EC configuration is higher than in the semiconductor cavity. The SCC configuration, on the other hand, has the field intensity within the air gap similar to that inside the semiconductor cavity.

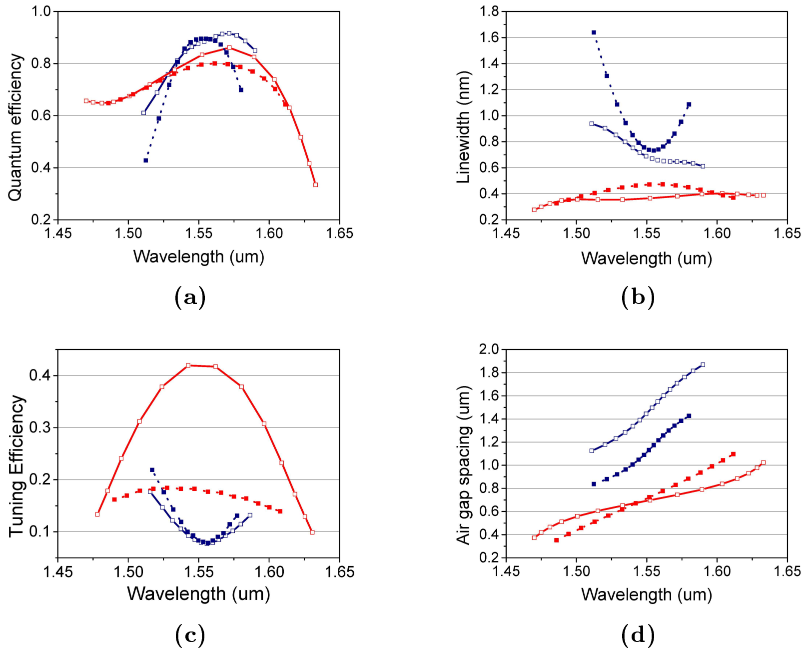

Figure 3.10: Simulation result of the devices. (a) Quantum efficiency, (b) absorption linewidth, (c) tuning efficiency, and (d) air gap spacing as a function of wavelength. Red solid line represents ACC. Red dashed line represents EC. Blue solid line represents SCC. Blue dashed line represents SCC with two DBRs

The FSRs for the ACC, SCC, EC and reference structures estimated by using Eq. 3.7 were 0.1531, 0.1226, 0.1113, and 0.2184 μm. From the numerical sim-

ulations, the mode spacings or FSRs of the ACC, SCC, EC, and the reference structures were 0.120, 0.137, 0.111, and 0.241 μm, respectively. For the EC structure, the analytical approximation is close to the numerical calculation. This is attributed to the linear reflection phase over the wavelength span. The SCC configurations were underestimated for both the HCG and DBR structure. This can also be explained by the steeper reflection phase away from the centre wavelength. The overestimation of the FSR for ACC configuration can also be explained similarly.

The device quantum efficiency, absorption linewidth, tuning efficiency, and air gap spacing as a function of wavelength were calculated by importing the reflection/transmission coefficients of the grating mirror calculated by RCWA software to MATLAB. The field distribution within the cavity was then calculated by the transfer matrix method (TMM) MATLAB script where we assume that the reflected wave from the grating mirrors are plane wave.

The quantum efficiencies of all cavity configurations shown in Fig. 3.10a are all above 0.8 at the centre wavelength. The peak quantum efficiency observed in SCC with 2 DBRs, EC, ACC, and SCC configurations are 89.50%, 79.58%, 83.33%, and 87.43%, respectively. The efficiency decreases as the resonant wavelength moves away from 1.55 μm. The tuning range of the ACC covers over 158 nm span. The EC, SCC, and SCC with 2 DBRs have tuning ranges of 125.7, 79.1, and 67.2 nm, respectively.

The detection linewidth is defined as the linewidth measured at its full width half maximum and can be approximated from the Eq. 3.9. The equation shows that the detection linewidth is proportional to the FSR. As previously discussed, the SCC with DBRs has the largest FSR. Hence, the widest linewidth. The other cavity configurations also obey this guideline. The linewidth variation over the wavelength span follows the inverse shape of the mirror reflectivity.

The tuning efficiency, $\frac{\partial\lambda_m}{d_{air}}$, can be estimated by using the following equation [17]

$$\frac{\partial\lambda_m}{\partial d_{air}} = \begin{cases} \frac{\lambda_0}{D_{eff}} & \text{extended cavity} \\ \frac{\lambda_0}{D_{eff}}\left(-\frac{\lambda_0}{4\pi}\left[\frac{\partial\theta_{top}}{\partial d_{air}}\right]_{\lambda_0}\right) & \text{unextended cavity} \end{cases} \tag{3.19}$$

where λ_0 is the centre wavelength, $\frac{\partial\theta_{top}}{\partial d_{air}}$, is a change of the reflection phase over the change of air gap thickness, and D_{eff} is a total effective optical cavity length. The Eq. 3.19 shows that for the extended cavity, the tuning efficiency is constant throughout the wavelength span. The unextended cavity, on the other hand, has the tuning efficiency changed as the top mirror reflection phase change over the air gap spacing.

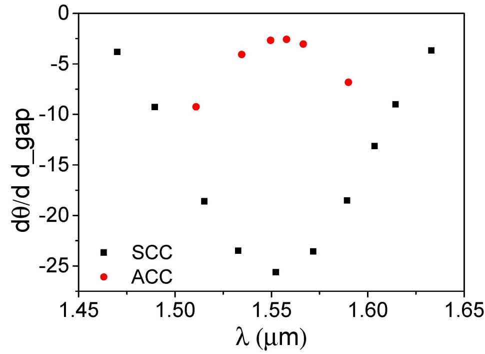

Figure 3.11: The reflection phase slope, $\frac{\partial\theta}{\partial d_{gap}}$, of the top mirror as a function of incident wavelength.

The reflection phase slope over the air gap spacing in Fig. 3.11 shows the phase slope calculated at each resonant wavelength. The result shows good agreement with the tuning efficiency obtained in Fig. 3.10c. Because the phase slope is negative for both the SCC and ACC top mirror configuration, the tuning efficiency calculates in Eq. 3.19 is a positive number because of the multiplication with $\frac{-\lambda_0}{4\pi}$.

The air gap spacing vs wavelength in Fig. 3.10d follows the same shape as the reflection phase shift of the air gap/cavity interface shows in Fig. 3.8. The change of the air gap means the shift in the device cavity length. Therefore, the air gap change undergoes the same phase shift as the mirror reflection.

3.1.2.3 Summary

In this section, we have presented the device performances of the tunable RCE photodetector with 3 cavity configurations (EC, ACC, and SCC) with the HCG structure compared to the SCC configuration with the DBR structure. We have shown that by incorporating the HCG structure, the device can be made more compact without compromising the device performances. By using the HCG, the FSR was much smaller than the DBR counterpart. Therefore, the detection linewidth at full-width half maximum is smaller. The tuning efficiency of the ACC configuration was the best out of all 3 cavity schemes and yielded largest tuning range.

3.1.3 Tunable RCE with HGs

Previously introduced in chapter 2, the HG reflectors have recently been proposed by our group. This new type of reflector offers an ultra high reflection bandwidth comparable to the HCGs. The mirror comprises of a grating layer made of a high refractive index material situated on top of a low refractive index material with an addition of a high refractive index cap layer attached on top of the grating. By adding another mirror on top, a Fabry-Perot cavity can be formed which induces a resonance inside the cap layer. This cap layer can be equipped with an absorbing material and form optoelectronic devices. In this section, we show an example of the RCE photodetector by incorporating the HG reflector with an active material in the cap layer and the HCG mirror.

3.1.3.1 Design

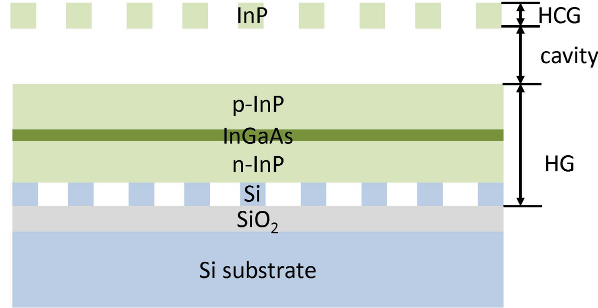

Figure 3.12: Schematic of a hybrid HG-HCG RCE photodetector.

The design of this tunable HG-HCG RCE detector is similar to the double HCG detector in the previous section. The device structure is shown in Fig. 3.12. The bottom HG reflector is made of Si on the SiO_2. The cap layer is an InP lattice-matched material with an absorbing layer placed at the field maximum position. The air gap cavity was determined by matching the reflection phase of the HCG and the HG mirror which is $\frac{n\lambda}{2} + \frac{\phi_{HCG}\lambda}{4\pi} + \frac{\phi_{HG}\lambda}{4\pi}$. The condition which yields the highest possible amount of absorption is similar to the conventional RCE detector with a minor difference. Because the photodiode is now an integral part of the reflector, the condition previously described in Eq. 3.18 is now reduced

to

$$R_1 = R_2 \tag{3.20}$$

For this type of detector, we cannot use the TMM to model the device because the field interaction within the diode region is not a plane wave. Therefore, we used the RCWA to calculate transmission and reflection of the entire structure and assume that the absorbing layer is the only lossy material within the device. The absorption was calculated as $A = 1 - R - T$.

3.1.3.2 Result

First, we investigated how the amount of reflection affects the absorption in the active layer. This investigation can also be applied to the previous type of RCE photodetector as well. As shown in Fig. 3.13, the amount of absorption is proportional to the mirror reflectance. The solid lines represent the bottom mirror reflectance, R_2. The blue dashed line shows the point $R_1 = R_2$ where the highest amount of absorption is observed. We can see that the absorption decreases exponentially as the mirror reflectance decreases. Therefore, to obtain high absorption from the RCE photodetector, the mirror reflectance should be as high as possible. However, it should be noted that for a highly reflective bottom mirror, a small mismatch between reflectance R_1 and R_2 leads to a drastic drop of the absorption especially when R_1 is higher than R_2.

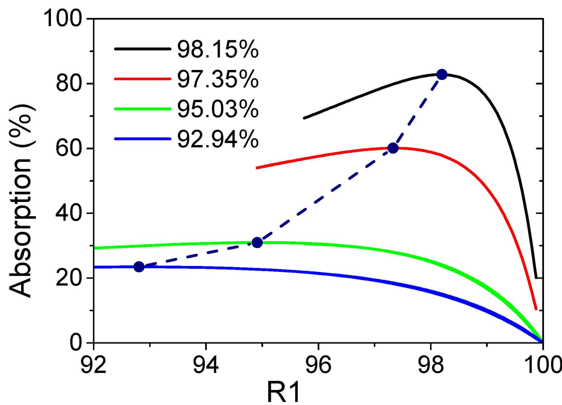

Figure 3.13: Absorption as a function of mirror reflectance R_1 and R_2.

Given the knowledge in Fig. 3.13, the device was designed by, first, determining the HG reflector parameters with an ultra high and flat spectral response. From

numerical simulations, we found the Si grating with a thickness of 520 nm, a grating bar width of 352 nm, and a period of 824 nm together with the InP cap layer thickness of 605 nm incorporating two 6.6-nm thick non-absorbing quantum wells gave the highest and the flattest spectral band. Under 1.55 μm TM-polarized normal light incident, the reflectance of the HG reflector was 99.65% with spectral bandwidth where $R_2 > 99\%$ equals to 170 nm. After adding an imaginary part of the refractive index, $\jmath 0.1$, to the absorbing layers and positioned them at the field maxima, the reflectance at 1.55 μm has reduced to 98.15% as seen in Fig. 3.14a. The reflectance of the entire wavelength span does not exceed 98.3%. After that, the HCG top mirror parameter was numerically determined to have the reflectance matched that of the bottom HG. Fig. 3.16a shows the InP top grating with a thickness of 530 nm, a bar width of 362.5 nm, and a period of 824 nm gives the reflectance of 98.29% at 1.55 μm. The spectral response reaches 99.99% at 1.470 and 1.645 μm incident wavelength. The transmittance plot of both mirrors show supported leaky mode resonances. The reflection phase shift in Fig. 3.14b indicates the greater phase slope on the HG reflector compared to the HCG. The reflection phase slope, $\frac{\partial \theta}{\partial \lambda}$ of the HG is 5.55 rad/μm at 1.55 μm, while the HCG is 6.85 rad/μm. However, the reflection phase slope of the HG increases to 99.1 rad/μm at 1.36 μm, while the HCG does not exceed the phase slope of 16.3 rad/μm for the entire span. Further information of the epitaxial structure can be found in appendix B.

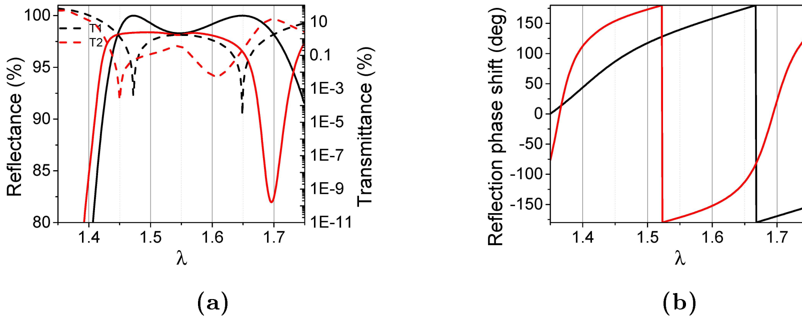

Figure 3.14: (a) Reflectance in linear scale and transmittance plot in log scale (b) Reflection phase shiftf the top mirror (black), R_1, and bottom mirror (red), R_2.

The $|E_x|$ field profile in Fig. 3.15 shows 1.55 μm surface normal light incident from the top, enters the resonant cavity, and exits the HG reflector to the 3 μm thick SiO_2 at the bottom. The figure shows strongest resonance within the air gap cavity. The HG reflector contains 3 field maxima and the absorbing material was placed in the middle of the cap layer. We can see a very small portion of light escaping the cavity to the SiO_2 layer.

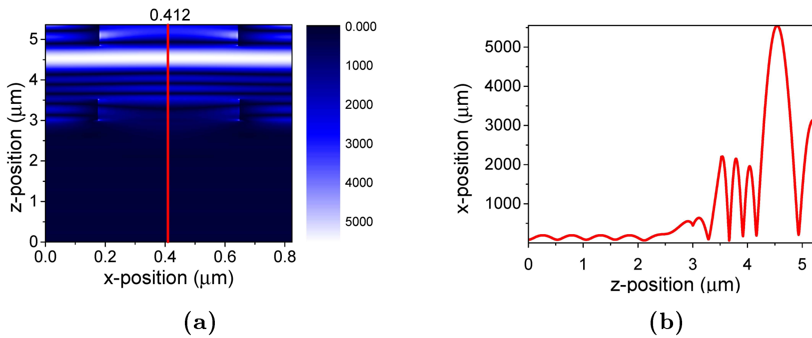

Figure 3.15: (a) $|E_x|$ field component of the hybrid HG-HCG RCE photodetector. (b) The cutline field profile from (a) at x = 0.412 μm.

Lastly, the tuning properties of the hybrid HG-HCG RCE detector have been investigated and the results are shown in Fig. 3.16a.

The absorption at 1.55 μm was calculated to be 82.68%. The tuning range where the absorption remains above 50% is 128 nm. The absorption linewidth is under 2 nm across the tuning range. The tuning efficiency shows a large improvement over the double HCG structure. In the previous section, we showed the highest tuning efficiency, 0.42, in the ACC configuration at the centre wavelength and drop to 0.1 when the resonant wavelength moves further away. However, for the HG-HCG structure, the tuning efficiency starts at 2 and increases as the resonant wavelength shifts from the centre wavelength. As a result, the device requires only 275 nm air gap spacing shift to move the resonant wavelength from 1.62 μm to 1.49 μm.

3.1.3.3 Summary

In conclusion, we have shown that the novel HG reflector can be used to form the RCE photodetector. Comparing to the double HCG structures in the previous section, this structure offers similar absorption efficiency and tuning range to the ACC and EC configuration. On top of that, the tuning efficiency increases drastically for the hybrid HG-HCG structure. This structure also facilitates the fabrication by removing the need of the low refractive index layer. Therefore, we decided to pursue the HG-HCG structure instead of the double HCGs structure. However, to modelling full device with absorption in other cladding layers, an in-house RCWA MATLAB script was developed. The script was used to model the epitaxial structure fabricated in the next chapter.

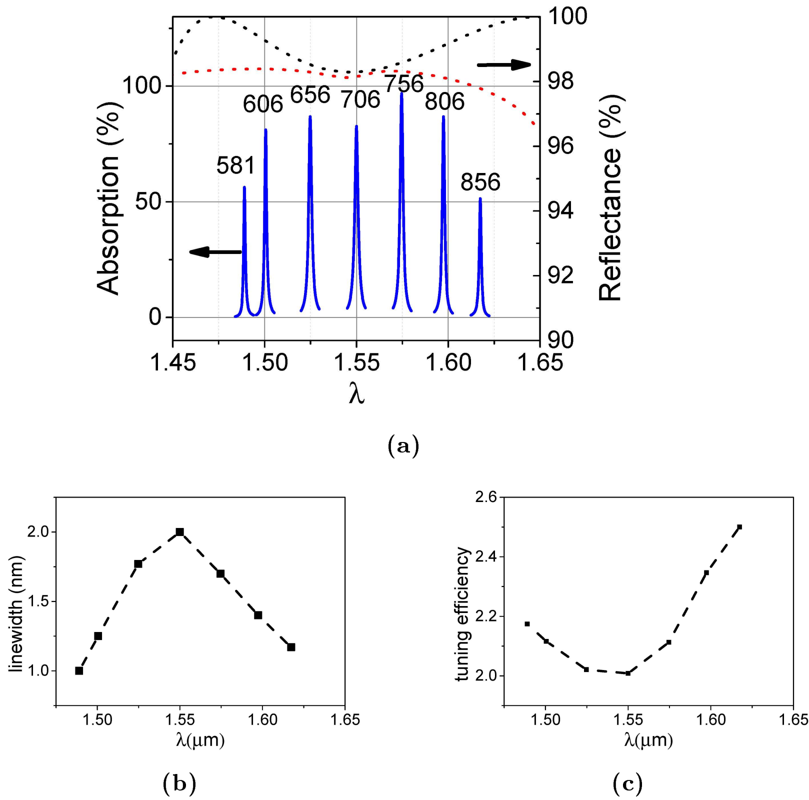

Figure 3.16: (a) Absorption efficiency of the tunable RCE photodetector across the wavelength span where the number on top of each spectral lines denote air gap spacing in nm. Blue and red dotted lines represent mirror reflectance R_1 and R_2, respectively. (b) Absorption linewidth at each resonant wavelength. (c) Tuning efficiency vs resonant wavelength.

3.2 Micro-Electro-Mechanical System (MEMS) Design

Previous section shows that the detection wavelength of the RCE detector can be changed by adjusting the cavity length. This can be achieved by moving the top grating mirror in the vertical direction. There are several schemes for micro actuations e.g. thermal actuation, piezoelectric actuation, and electrostatic

actuation. For the device in this study, the electrostatic actuation was pursued.

3.2.1 Electrostatic Actuation

Electrostatic actuation is one of the most common actuation schemes. It only requires two conductive materials which are relatively easy to fabricate. It requires relatively low energy consumption and can provide higher speed response than thermal actuation scheme. When an electric field is applied to a capacitor, there are charges stored on both capacitive plates, one with positive charges and another with negative charges. These opposite charges create an attraction force between the plates. When both plates are fixed, the energy is stored between the plates and may dissipate as heat in the resistor. However, when at least one plate is movable, this energy can be dissipated in a form of physical displacement.

Without considering fringing field, capacitance of a movable parallel plate capacitor is expressed as [55]

$$C = \frac{Q}{V} = \frac{\varepsilon A}{d} \tag{3.21}$$

where ε, A, and d are the dielectric constant, the overlap area, and the gap between the two conductive plates, respectively. Q is the electric charge and V is the potential difference. The stored energy is given by

$$U = \frac{1Q^2}{2C} = \frac{Q^2 d}{2\varepsilon A} \tag{3.22}$$

and the co-energy is

$$U^* = \frac{CV^2}{2} = \frac{\varepsilon A V^2}{2d} \tag{3.23}$$

For a linear capacitor, both the energy and co-energy are the same. However, they could be different in a nonlinear capacitor. By taking a derivative of the energy, the force and potential difference are calculated by,

$$F = \frac{\partial U}{\partial d} = \frac{Q^2}{2\varepsilon A} \tag{3.24}$$

$$V = \frac{\partial U}{\partial Q} = \frac{Qd}{\varepsilon A} \tag{3.25}$$

The electrostatic actuator can be operated under two schemes, i.e., charge control and voltage control. However, in practice, it is difficult to design and build

a very small predetermined current source under a wide range of voltage. Therefore, we will only discuss the voltage control operation here.

Since we are dealing with the voltage control, the co-energy must be used. When we take a derivative of Eq. 3.23 with respect to V, we will get Q:

$$Q = \frac{\varepsilon A}{d} V \tag{3.26}$$

By substituting Eq. 3.26 to Eq. 3.24, we can get F:

$$F = \frac{\varepsilon A V^2}{2d^2} \tag{3.27}$$

where

$$d = d_0 - z \tag{3.28}$$

$$z = \frac{F}{k} \tag{3.29}$$

where d_0 is an air gap spacing at the resting position, z is the displacement of the movable plate, and k is the spring constant. Therefore, we can rewrite Eq. 3.28 as

$$d = d_0 - \frac{\varepsilon A V^2}{2kd^2} \tag{3.30}$$

Eq. 3.30 shows that as the voltage increases, the gap decreases. Thus, this positive feedback system can go unstable under a critical voltage which is known as "pull-in voltage". By taking a derivative of the net force of the system with respect to d, $F_{net} = -F_{electrostatic} + F_{spring}$, the stable condition is calculated to be

$$k > \frac{\varepsilon A V^2}{d^3} \tag{3.31}$$

Therefore, the pull-in gap occurs at

$$d_{PI} = \frac{2}{3} d_0 \tag{3.32}$$

and the pull-in voltage is

$$V_{PI} = \sqrt{\frac{8kd_0^3}{27\varepsilon A}} \tag{3.33}$$

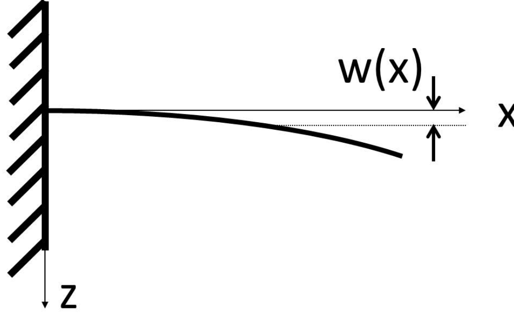

Figure 3.17: Geometry of a bent cantilever beam.

3.2.2 Beam Bending

As shown in Eq. 3.33, to calculate the pull-in voltage and the plate position, a mechanical spring constant must be determined. Consider a simple cantilever beam under a transverse load, a differential equation for small angle bending is given as

$$\frac{d^2w}{dx^2} = -\frac{M}{EI} \tag{3.34}$$

where w is the position of a beam deviating from the neutral position along the x-axis, M is the internal bending moment, E is the Young's modulus, and I is the moment of inertia which is

$$I = \frac{1}{12}WH^3 \tag{3.35}$$

where W denotes the beam width and H is the beam thickness.

For a concentrated load, the internal moment at any x-position along the beam is $M = -F(L-x)$ where L is the beam length and F is the applied force. Thus, Eq. 3.34 is rewritten as

$$\frac{d^2w}{dx^2} = \frac{F(L-x)}{EI} \tag{3.36}$$

After solving the linear equation, we find

$$w = \frac{FL}{2EI}x^2(1 - \frac{x}{3L}) \tag{3.37}$$

The maximum deflection occurs when $x = L$. Thus,

$$w = \frac{L^3}{3EI}(F) \tag{3.38}$$

and the spring constant of the cantilever is expressed as,

$$k = \frac{F}{w} = \frac{3EI}{L^3} = \frac{EWH^3}{4L^3} \tag{3.39}$$

For a uniformly distributed load on the entire beam, the spring constant can be calculated by using the same procedure from Eq. 3.34 to Eq. 3.38. However, the internal moment, M, is changed to $\frac{f}{2}L^2$ [56], where f is the force per unit length. The maximum displacement becomes

$$w = \frac{L^4}{8EI}(f) \tag{3.40}$$

and the spring constant is given by,

$$k = \frac{2EWH^3}{3L^3} \tag{3.41}$$

3.2.3 MEMS simulation

To accurately model the MEMS structure, we have used COMSOL Multiphysics to solve the coupled equations of the structural deformation and the electric field. In order to validate the model accuracy, we first simulated a simple cantilever under a uniformly distributed electrostatic force and compare the result with an analytical solution. The physical parameters used in the simulation are shown in table 3.2.

Physical property	Value
Young's modulus	6.106 [$x10^{11} dyn/cm^2$]
Poission's ratio	0.357
Density	4.81 [g/cm^3]
Relative permittivity	12.3

Table 3.2: Physical properties of InP [57].

Fig. 3.18a shows the deflection surface plot of the cantilever with thickness of 530 nm, width of 1 μm, and a length of 17 μm. The cantilever is suspended in the air, 664 nm above the ground electrode. The simulation was done in both 2D and 3D to show the effect of the fringing field. From Eq. 3.32, the pull-in gap is 442.67 nm which corresponds to the pull-in voltage of 26.66 V. The

analytical solution and COMSOL simulation of the maximum deflection under each bias voltage in Fig. 3.18b shows small discrepancy at high bias voltage. The 2D simulation deflects less compared to the analytical solution because of the spring constant weakening effect [58]. By introducing the air gap variation, the capacitance of the system changes as a function of position. As the air gap spacing decreases, the electrostatic force increases. Therefore, an effective spring constant of the system decreases. We could calculate the capacitance vs cantilever position profile to induce a position dependent effective spring constant. However, this analytical solution is only used as a design guideline, so we have opted out this weakening effect for calculation simplicity. The 3D simulation proves that fringing field plays a role in making the cantilever deflects more than the analytical expression.

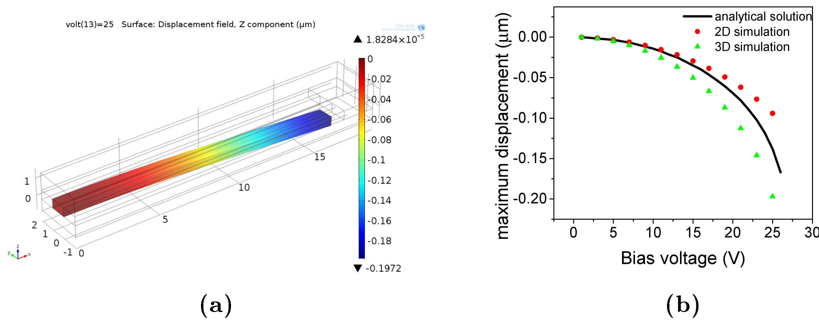

(a) (b)

Figure 3.18: (a) Deflection surface plot of the cantilever under 25 V bias. (b) Comparison between analytical solution, 2D simulation, and 3D simulation of the maximum deflection of the cantilver.

After we have validated the simulation tool, we move on to modelling the actual MEMS structure used in the fabrication. By importing the L-Edit layout to COMSOL, the MEMS dimension is the same as in the e-beam exposure pattern. The structure dimensions were initially determined by analytical expressions. By assuming that the grating is an attached mass, the spring constant could be calculated by the concentrated load model. The design is intended to operate under 20 V bias. The structure thickness, air gap spacing, and the dimension of each suspensions is the same as the previous example. The size of the grating area is 12 μm x 12 μm with 2 μm wide frame. The simulation result in Fig. 3.19 shows the surface displacement, von Mises stress, and deflection vs applied voltage. This design shows 171 nm deflection at 16 V with maximum stress of 52.8 MPa, much lower than the InP fracture limit of 910 MPa [59].

3.2.3.1 Summary

To sum up, we have shown the MEMS design for the grating mirror in this section which operates under 20 V. The maximum deflection of 171 nm at 16 V was enough to shift the resonant wavelength approximately half of the tuning range.

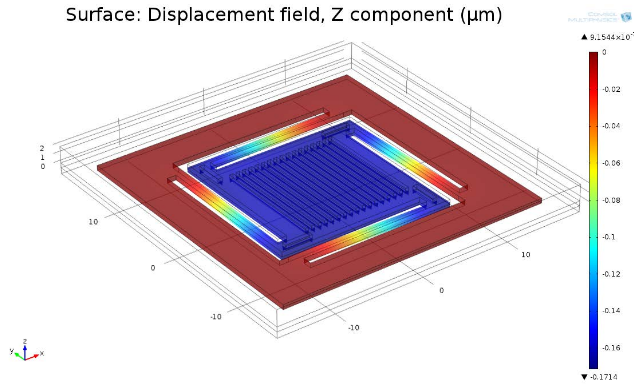

(a)

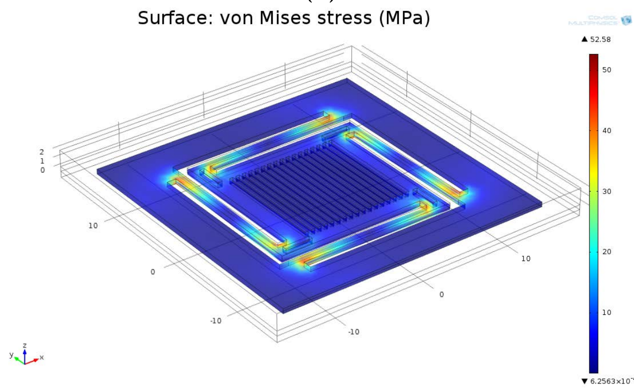

(b)

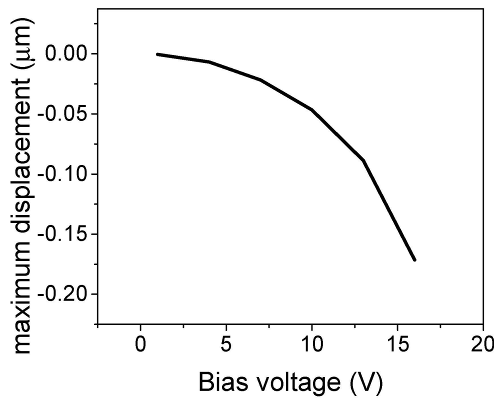

(c)

Figure 3.19: (a) Deflection surface plot of the InP MEMS under 16 bias voltage. (b) Stress surface plot (c) Maximum deflection as a function of voltage.

Chapter 4

Device Fabrication

In this chapter, we will describe the realization of the tunable HG-HCG RCE photodetector described in the last section of chapter 3. The epitaxial structure is described in appendix C and the details processing flow are described in appendix A. The chapter is organized into 2 sections: the **device processing** and the **processing tests**. The device processing describes the whole processing steps to make the device. The **processing tests** section describes several small tests to determine process parameters used in the main processing.

4.1 Device Processing

The device fabrication consists of 2 electron-beam lithography and 9 UV contact lithography steps. The schematic of the full processing sequence is shown in fig. 4.1.

(a) **Bottom grating patterning** To make the device we started by solvent cleaning a 1.5 x 1.5 cm SOI chip in an ultrasonic bath. Then, spun coat an electron beam sensitive resist and followed by soft baking the resist. Next, the chip was exposed to an electron beam to draw the grating pattern. After the pattern was developed, we baked the sample to increase the dry

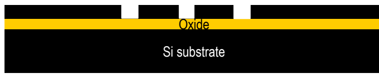

(a)

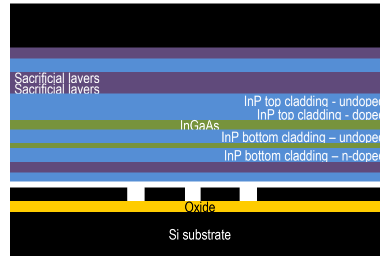

(b)

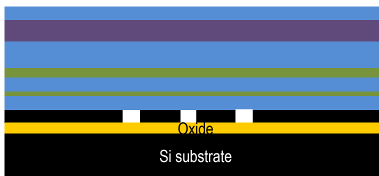

(c)

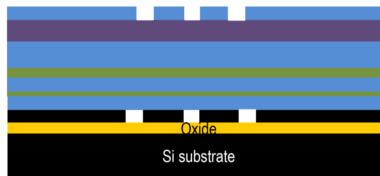

(d)

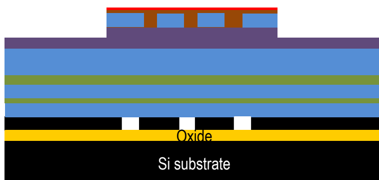

(e)

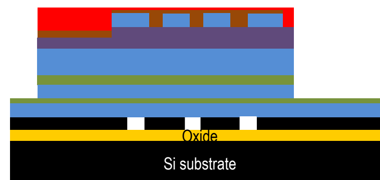

(f)

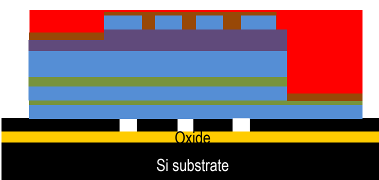

(g)

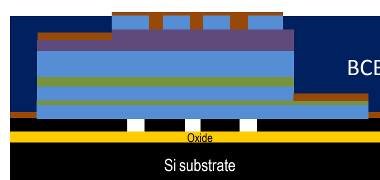

(h)

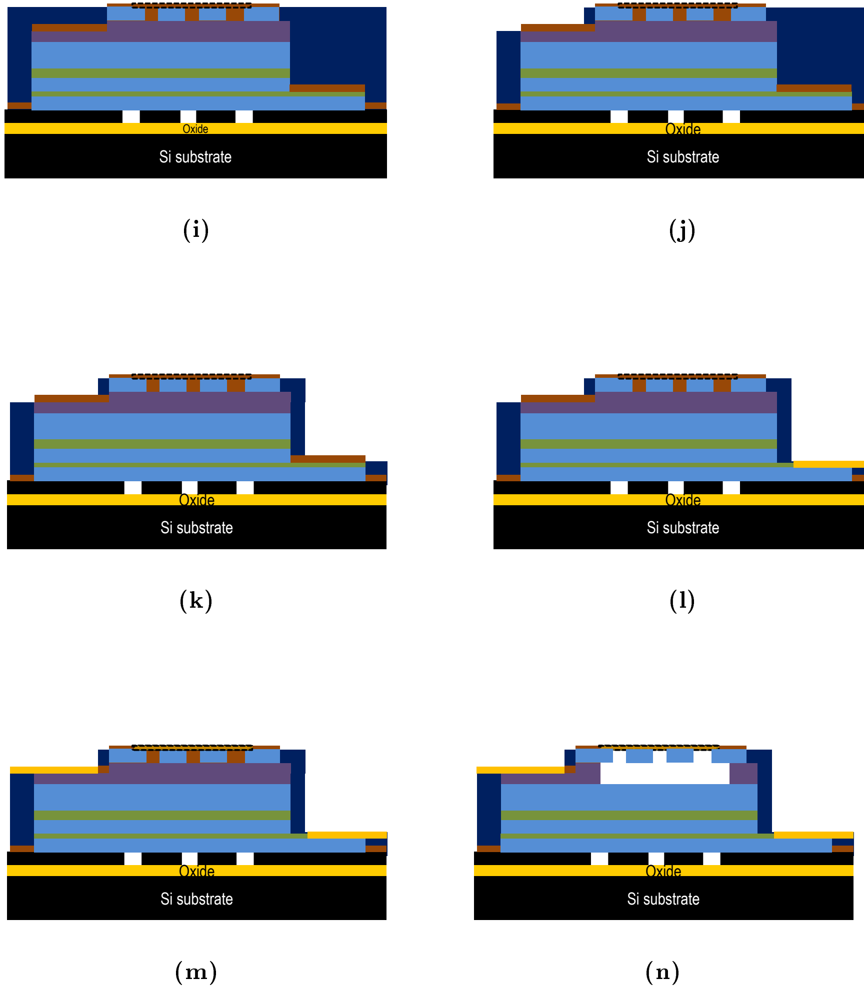

Figure 4.1: Device processing

etch selectivity. To transfer the grating pattern from the e-beam resist to the top Si layer, the sample was dry etched with C_4F_8 and SF_6 gases using a Bosch process.

(b) **Preparing the III-V epitaxy** Next, The epitaxially grown III-V samples were prepared by solvent cleaning the cleaved 8 x 8 mm chip with the SOI sample in the previous step. Then, the protective cap layers of the III-V sample was removed in 37% HCl and $1H_2SO_4$:8 H_2O_2:8 H_2O, respectively. The next bonding step requires a particle free surface. If particles were observed, the sample has to be cleaned again in DI water. However, the ultrasonic cleaner should be avoided for the III-V chip because particles from the cleaved surface could be deposited on the sample due to wet etching effect in the earlier process.

(c) **Chip bonding** After both the SOI chip and the III-V chip were prepared, the bonding process began with the modified RCA1 treatment at elevated temperature for 10 mins to remove remaining organic particle and have a hydrophilic surface finish [60, 61]. Then, DI water was rinsed on the samples. Next, both chips were treated with O_2 plasma [62, 63]. The superhydrophilic surface was activated by dipping both chips in the DI water. Followed by baking for 10 mins to remove water vapour on the surface. The chips were manually bonded at room temperature afterwards. To complete the bonding process, the bonded samples were loaded into the bonder system. The samples were heated under applied force. Next,

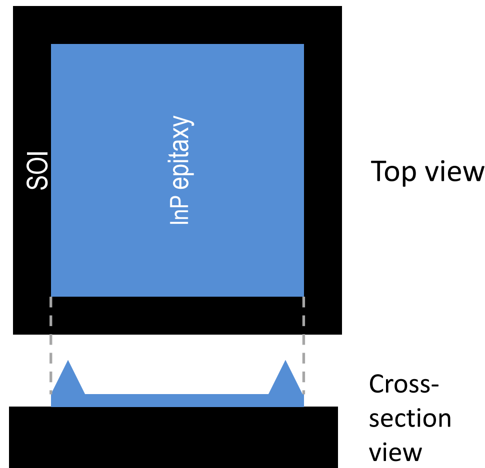

Figure 4.2: Schematic of the bonded sample after InP wet substrate removal with 37% HCl .

the InP substrate was removed by the 37% HCl and rinsed with DI wa-

ter. Because of the anisotropic wet etching nature of the InP, we observed an InP protruding part at the edge in the $[0\bar{1}\bar{1}]$ and $[0\bar{1}1]$ direction after finishing the process as shown in Fig. 4.2 [64]. These protruding edges are more than 100 μm in height. So, these edges had to be manually removed. By spinning on photoresist at arbitrarily thickness, the protruding edges were scratched off with a tungsten pen or diamond pen. Then, the samples were cleaned in solvent to remove the photoresist together with dust particles. Finally, the InGaAs etch stop layer was removed with $1H_2SO_4$:8 H_2O_2:8 H_2O.

(d) **Top grating patterning** The top grating patterning was done through a pattern transfer from the e-beam resist to a Si_3N_4 hard mask via dry etching process. Then, the e-beam resist was removed and the samples were ashed with O_2 plasma to remove the remaining residue. The pattern transfer from the Si_3N_4 to the InP grating layer was done through another dry etching. Finally, the Si_3N_4 was stripped off by buffered HF (BHF).

(e) **Forming the first mesa** In this step, we opened the p-contact area through wet etching. The process started with deposition of Si_3N_4 hard mask and spin coating the photoresist. The sample was then exposed with the UV contact aligner and developed in the 1AZ351B:$5H_2O$ solution. The mesa pattern was transferred to the Si_3N_4 by wet etching, subsequently. Next, after removing the photoresist with acetone, IPA, and O_2 plasma, the InP layer was etched by dry etching and the InGaAs layer was wet etched for 360 nm by 10(10 %)H_2SO_4:$8H_2O_2$:$71H_2O$. We chose wet etching to expose the contact area to avoid surface damage and contamination from dry etching. On the other hand, we need to precisely control the etch depth in this step, so the diluted etchant was chosen. The etch rate of the wet etchant can be different on each mixing. Because an in-situ equipment to monitor the etch depth is not available, the process had to be carefully done by repeated etching and monitoring with a profilometer. Again, we finished off this step by removing the Si_3N_4 with the BHF. Note that, we removed and redeposited the hard mask in every step because of large thickness variation of the deposited film. It is important that we know the precise thickness of the hard mask for monitoring purpose. Therefore, to minimize the variation, we chose to deposit a new hard mask in every step.

(f) **Forming the second mesa** Next, the n-contact area was exposed. We started off by depositing the new Si_3N_4 and patterning the second mesa by using the UV lithography. Again, the pattern was transferred to the Si_3N_4 layer by wet etching and the photoresist was removed, respectively. To open the n-contact area, we chose a combination of dry and wet etching. First, we dry etched the remaining InGaAs and p-cladding layer. The etching was stopped right before the InGaAs absorbing layer. The dry

etch was chosen in the beginning to minimize undercut area and gives a better control of the device size. Then, the samples were dipped in 1(37 %)HCl:4(85 %)H_3PO_4 solution to selectively remove the remaining InP, followed by 1H_2SO_4:8H_2O_2:8H_2O to selectively remove the InGaAs, and 1(37 %)HCl:4(85 %)H_3PO_4 again to reach down to the InGaAsP etch stop before the n-contact layer. We chose to stop the dry etching before the InGaAs layer to prevent over etching and damage on the n-contact area.

(g) **Forming the third mesa** The third mesa was done to isolate the devices from one another. After removing the Si_3N_4 from the previous step, we directly spun on the photoresist without depositing another Si_3N_4 because only wet etching was done at this step. After the pattern was created by the UV lithography, the samples were dipped into 1H_2SO_4:8H_2O_2:8H_2O to remove the InGaAsP etch stop layer and followed by 1(37 %)HCl:4(85 %)H_3PO_4 to remove the remaining InP layer. Again, we finished this step by removing the photoresist with acetone, IPA, and O_2 plasma, respectively.

(h) **Bisbenzocyclobutene (BCB) planarization** Before continuing to the planarization step, the Si_3N_4 was deposited on the sample. This Si_3N_4 layer will be used as a protective layer in the subsequent processes. The planarization step was done by spin coating an adhesion promoter AP3000, followed by the BCB, and baking to remove solvent and stabilize the film. After the coating, the sample was hard cured in a BCB oven at 250 °C for 6 hours. This curing achieves 95-100% polymerization according to the technical paper from the manufacturer. Because the BCB can be oxidized at elevated temperature (>150°C), the curing has to be done in an oxygen free environment. Next, we dry etched the BCB to expose the grating area. In the first processing, we had a big square with a size of 500 x 500 μm^2 as a test structure for end point detection. However, because it was a large island, the film on the test structure was thicker than on the device which caused us to over etched the sample. We have resized the test structure to 100 x 100 μm^2 and 50 x 50 μm^2 in the second processing and found the 100 x 100 μm^2 was a suitable size for monitoring purpose. The 50 x 50 μm^2 island was too small for the laser spot. Note that, the end point measurement was on the Si_3N_4 surface and we timed the etch until the BCB was at the same level as the InP grating. The etch selectivity of the Si_3N_4 to BCB was about 1:10. The mask erosion was taken into account for the precise etching.

(i) **Grating contact opening** Next, the grating contact area was opened by patterning the grating contact opening area with the UV lithography and followed by dipping the sample in the BHF to remove the Si_3N_4 hard mask. Then, the photoresist was removed by solvent. Note that, we stopped using the O_2 plasma cleaning at this step because the gas can

etch the BCB. The photoresist baking after development was avoided if no dry etching needed to increase the resist solubility in the solvent. In addition, we chose to open the contact from the top area to the bottom to minimize the spin coating non-uniformity due to surface topology.

(j) **p-contact opening** The p-contact opening pattern was formed by the UV lithography. At this step, the samples were baked after the photoresist development to reflow the photoresist. The reflowing helps achieving a tapered wall profile which is beneficial for metal deposition coverage. After the baking, the sample was dry etched to the p-contact area. It is crucial to stop the etch right on the p-contact level which is below the Si_3N_4. Another end point detection area is needed similar to the previous step. Lastly, we wet etching the Si_3N_4 with the BHF and removed the photoresist using solvent.

(k) **n-contact opening** The contact opening at this step was done similarly to the previous step. By patterning the n-contact opening via UV lithography, the contact area was opened by dry etching through the BCB, the InGaAsP etch stop layer was removed by $1H_2SO_4$:$8H_2O_2$:$8H_2O$, and the process was finished by removing the photoresist mask using the solvents. We would like to address here that the etch depth necessary to open this contact from the top grating level is 1.95 μm. In the first processing batch where we directly etched 1.95 μm in one go, and we have experienced difficulty in removing the photoresist afterwards. As shown in Fig. 4.3a

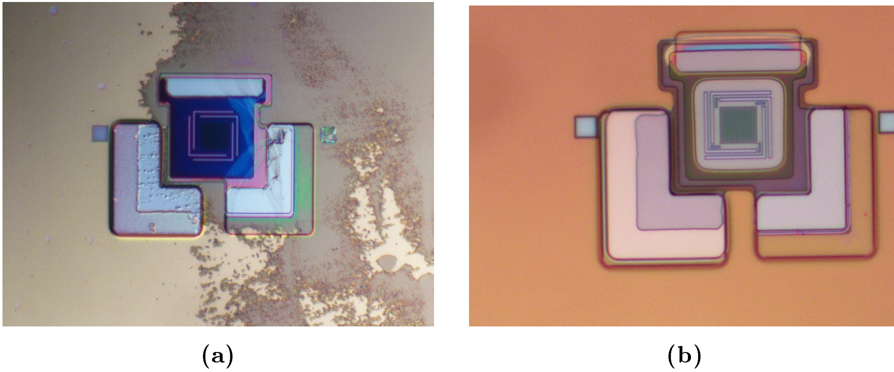

(a) (b)

Figure 4.3: Microscope image of the (a) first processing batch (b) second processing batch after removing the photoresist in the n-contact opening step.

where the photoresist residue was observed after solvent clean on the p-contact (right) and grating contact area (top). We suspected the prolong dry etching process increases cross linking of the photoresist. Therefore,

we decided to use 2 steps etching in the second processing batch. The first etch was done together with the p-contact opening and another etch was done in this step. Thus, the etch depth splits into 894 nm depth and 1061 nm depth, respectively. As a result, the photoresist residue disappeared in the second batch.

(l) **n-metal deposition** Next, the metals were evaporated onto the samples to form an electrical connection of the device. Before actually depositing the metals, It is worth mentioning that the glass transition temperature of the BCB is above 350 °C. We will show in the later step that the annealing temperature of the contacts is higher than the glass transition temperature. Therefore, to avoid reflowing of the BCB in later steps, the samples were heated at the annealed temperature in the beginning of this step. After that, the metals were deposited by patterning the n-metal with the negative photoresist using the UV contact lithography. After the exposure, the sample has to be baked again. This is called the "post exposure bake" which harden the resist part that was exposed to the UV light. After the development, the samples were dipped in the $1H_2SO_4{:}8H_2O_2{:}8H_2O$ solution to remove a native oxide on the surface [65] and then loaded into the metal evaporation chamber to deposite 20 nm Pd/ 40 nm Ge/ 40 nm Ti/40 nm Pt/ 250 nm Au. Finally, the metal was lifted off in the MR1165 remover.

(m) **p-metal deposition** The p-metal deposition was done similarly to the n-metal deposition step except that the surface preparing solution changed to $1(37\,\%)HCl{:}4(85\,\%)H_3PO_4$ and the metal material is 50 nm Ti/ 75 nm Pt/ 250 nm Au. After completing the deposition, the sample was rapidly annealed at 440 °C for 15 sec to alloy the metal to the InP and formed an ohmic contact.

(n) **Sacrificial etch** The last step of the device fabrication is releasing the grating MEMS structure by wet etching of the InGaAs sacrificial layer. In the first processing batch, after patterning the grating opening area with the positive photoresist, the sample was dry etched to remove remaining BCB in the grating groove. The second batch, on the other hand, the BCB was removed in the p-contact opening step. The process was modified to ensure a complete BCB removal. The Si_3N_4 was removed by the BHF, subsequently. Next, the sample was dipped in the $1H_2SO_4{:}8H_2O_2{:}8H_2O$ for 50 sec in the first batch and 2 min in the second batch. The increase etch time in the second batch was because of incomplete etch observed in the 50 sec etch time seen in Fig. 4.4. The highlighted green area represents the remaining InGaAs layer around the grating border, which is 2 μm wide. After the etching, the sample was immersed in a running DI beaker. Then, without blow drying the sample, we removed the photoresist by immersing the sample in the solvents. Note that, after sacrificial etching, the sample

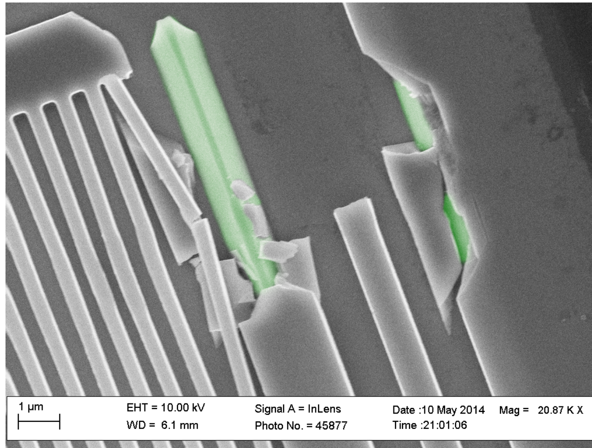

Figure 4.4: SEM image showing an incomplete sacrificial etch in the first processing batch.

should not be dried to prevent stiction of the MEMS structure. Next, we repeatedly immersed the sample in a new IPA 4-5 times to completely remove any remaining H_2O. The sample was then loaded into the CO_2 critical point dryer to dry the structure.

4.2 Processing tests

Before starting the main processing flow, several short processing tests had to be done to develop and confirm process parameters. To minimize possible failures, the tests were designed to have conditions closest to the main processing. In this section, we describe the major processing tests done to determine process parameters in the main processing. The tests include electron beam dose test, dry etching of a grating structure, wet etching of materials, lift off process development, and metal deposition on a tapered BCB.

4.2.1 Electron beam dose test

Electron beam lithography (EBL) is a technique to directly write nanoscale structures. The objective of the e-beam writing is to achieve arbitrary patterns with high resolution, high sensitivity, and high reliability. The process

conditions include electron beam energy, dose, development time and temperature. Factors that complicate these process conditions are forward scattering and backscattering of electrons. As electrons enter the resist, they begin to elastically collide and deflect. This is called forward scattering, which broaden the beam spot size. When electrons pass through the resist, they usually penetrate into the substrate. Some fractions of electron undergo a large angle collision and re-emerge into the resist. This backscattering can be microns away from the entering points. This is called the "proximity effect". In addition, for an inelastic collision, some of the energy dissipates into secondary electrons and contributes to the proximity effect. However, the contribution is much smaller compared to the backscattering. So, it is often negligible. It is known that the effective dose contributed by the backscattered electrons is proportional to the substrate's atomic number and III-V material has a higher atomic number than Si substrate. Determining the clearing dose for the grating pattern on each type of substrate is required. Furthermore, we have verified that for a small exposed area, e.g. 20 x 20 μm^2 of the grating, the dose modulation was not necessary because the energy was distributed uniformly in a small area.

The experiment started with an exposure series on the bonded sample and found the clearing dose of the 500 nm ZEP520A positive e-beam resist started from 220 $\mu C/cm^2$ at 100 kV. However, for repeatable processing, we increased the dose to 250 $\mu C/cm^2$. In addition, we ran exposure series on the InP substrate and found the dose required to clear the resist was 180 - 200 $\mu C/cm^2$. The grating width was 80 nm narrower than the design is shown in Fig. 4.5. The grating width further decreases by 100 nm after 10:20 min Si_3N_4 etch. It is also shown in Fig. 4.5 that after the resist development, the side wall profile was still vertical. We will later show in the next section that the tapered side wall is observed during the dry etching process.

4.2.2 Reactive ion etching of the grating

To transfer the grating pattern from the e-beam resist to the Si_3N_4 hard mask and the InP layer, respectively, the etch time was needed to be determined. It is known that the etch rate in the reactive ion etcher (RIE) can be proportional to the total exposed area. This is called the "loading effect". Normally, the etch rate decreases as more etch surface exposes in the chamber [66]. However, local variation in pattern density causes local variation in etch rate as well. This is called the "microloading effect" [67]. Therefore, the endpoint detection test structure which is normally a large open square cannot represent the etch rate inside the grating grooves and they are too small for the laser interferometer to determine the stop position. As a result, it is important to perform a test to determine the etch time required for a particular grating structure.

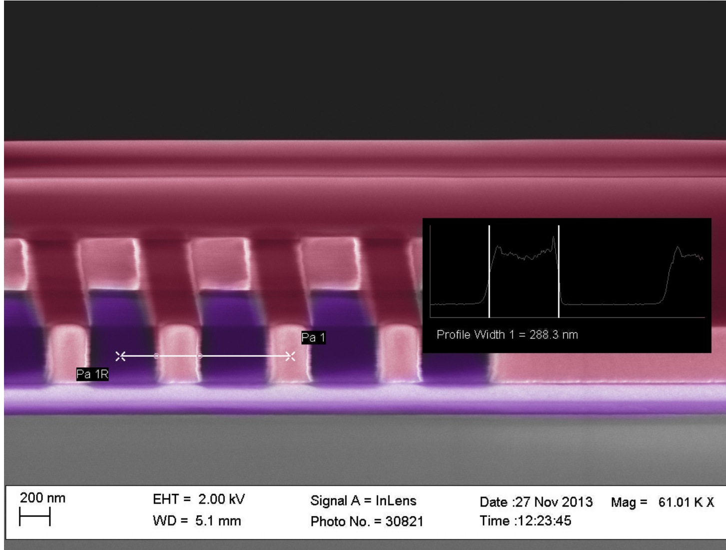

Figure 4.5: Cross section SEM image of the e-beam resist after development. Red hue represents the e-beam resist. Purple hue represents the Si_3N_4 hard mask.

4.2.2.1 Pattern transfer to Si_3N_4

Etch gases for Si_3N_4 established at our Cleanroom facility is CHF_3 and O_2 with the flow rate of 15 sccm and 1 sccm, respectively. In this experiment, we deposited 200 nm thick PECVD Si_3N_4 on the Si substrate, span coat an e-beam resist on top, and soft baked the sample. Then, the grating pattern was exposed using the e-beam writer. The pattern was developed with ZED-N50 developer. The grating arrays were 100 μm apart to minimize the proximity effect with the size of 20x20 μm^2 each. The grating period was 710 nm with the grating width of 404.7 nm. Furthermore, a 100x100 μm^2 box was put on the sample as a reference. Next, each sample was loaded into the RIE chamber and etched for 2:40 min, 05:20 min, 08:00 min, 10:20 min, and 13:20 min, respectively. We found the etch rate on the 100x100 μm^2 isolated opened box was 45.6 mm/min. Therefore, this large opening box required 4:20 min to etch 200 nm Si_3N_4. The etch rate in the grating grooves, on the other hand, are different. Figure 4.6 shows the cross-section of the grating structure with different etch times. The sample with the shortest etch time, 5:20 min, shows incomplete etch with curvature at the bottom corner as seen in Fig.4.6a. As the etch time increases, the side wall profile improves. However, the bottom linewidth decreases from 303 nm in Fig.4.6b to 207 nm in Fig.4.6d. This huge difference from the design

has to be taken into account. From this experiment, we chose to use 10:20 min etch time for future processing. However, it should be noted that we did not additionally bake the resist after development. The etch rate might be different if the resist is baked.

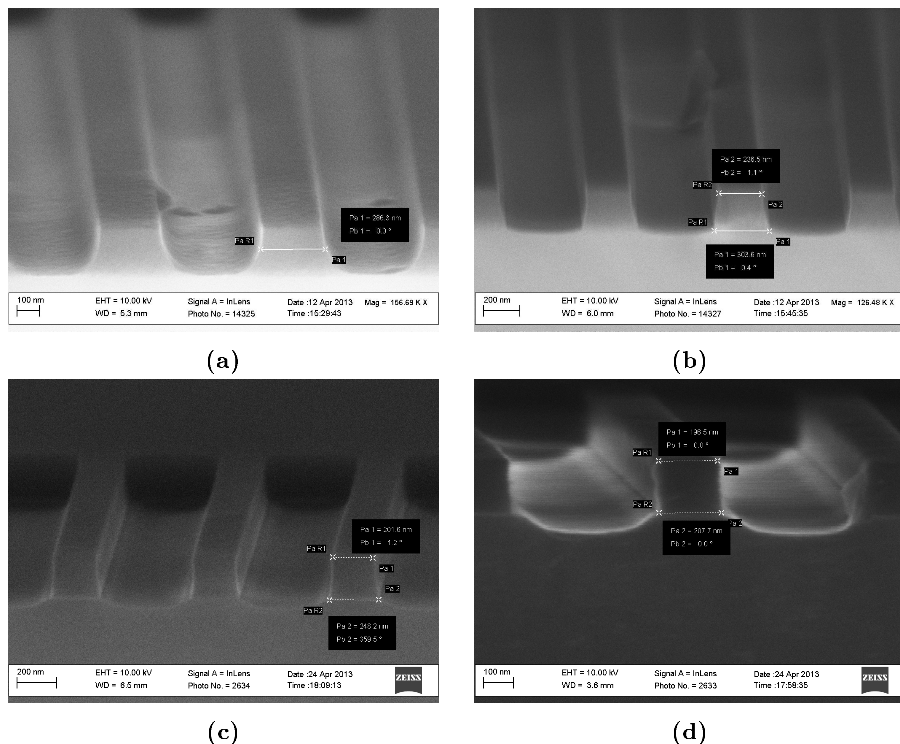

Figure 4.6: Cross section SEM images of the (a)05.20 min (b) 08.20 min (c) 10.20 min (d) 13.20 min Si_3N_4 etch on Si substrate.

4.2.2.2 Pattern transfer to InP

In this section, the pattern transfer from Si_3N_4 to InP was investigated. For a steep wall profile, we used the etch recipe that has been developed in our facility which uses a switched processing. This is a time multiplexed etch alternating between an overpassivation to protect side wall and isotropic etching of the passivated layer. Etch gasses are CH_4 and H_2 with a flow rate of 4.2 sccm and 33.6 sccm, respectively. The first experiment in this series started with finding out the erosion of the 200 nm Si_3N_4 hard mask under a standard InP etch recipe.

The mask erosion was negligible for 9 cycles of 2:30 min etch InP as shown in Fig. 4.7.

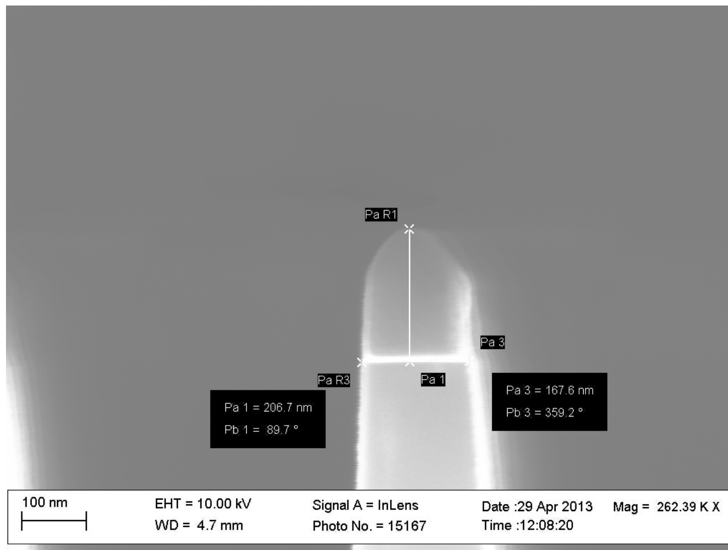

Figure 4.7: Si_3N_4 mask erosion after 9 cycles etch.

Next, the etch rate of the InP in the grating groove area was tested. The etch depth of 8 cycles was found to be 506 nm and 9 cycles was 551 nm. The designed grating thickness in the device is 530 nm. Therefore, from the test, 9 cycles etch for the main processing was chosen.

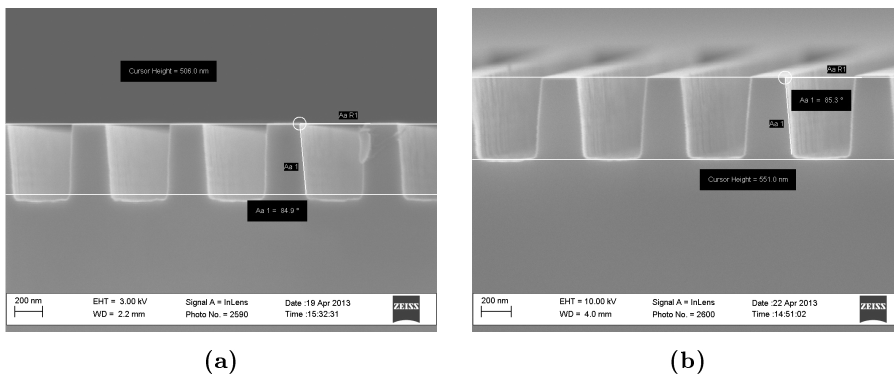

Figure 4.8: SEM images of the (a)8 cycles (b) 9 cycles InP surface relief etching.

Finally, we used the etch time obtained in the previous experiments on the bonded sample to find the linewdith reduction offset needed to put on the lithography mask. The duty cycles were varied on the grating mask. As shown in Fig. 4.9, the top and bottom linewidth was measured from the cross-section SEM images. After plotting the graph, a linear equation was determined and the offset required for the arbitrary duty cycle in the final etch mask was found.

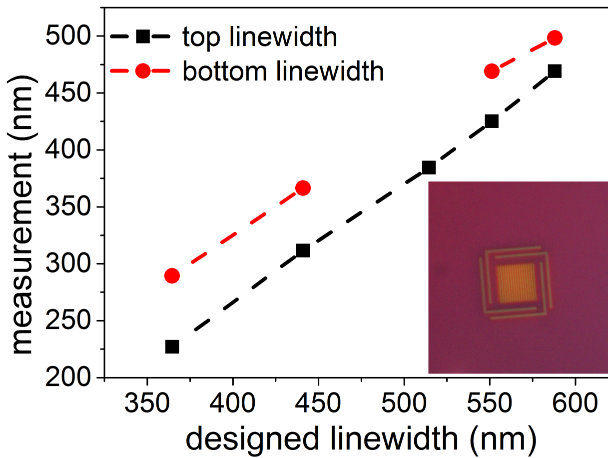

Figure 4.9: Measurement grating width vs designed grating width.

It should be noted that a vertical wall profile in the simulation was assumed. However, in the fabrication, we observed a slanted profile of approximately 84 to 87 degree depending on the duty cycle. Therefore, the linewidth in the middle was used as a reference to compare the simulated result.

4.2.3 Wet etch tests

Wet etching was used throughout the processing steps for sacrificial etching and avoiding dry etch induced damage. It is necessary to know the etch rate of each material to control an etch depth and undercut. The wet etch test on of several materials was needed after we found the etch rate has deviated from the previous records. Table. 4.1 shows wet rate rate of several materials.

Wet etching is normally isotropic. However, for crystalline materials, the etch rate is typically lower on a densely packed surface. For sacrificial etching, the etch rate in lateral direction has to be determined. In our fabrication procedure,

Table 4.1: Wet etch rate.

	InP	InGaAs	PECVD SiO_2	PECVD Si_3N_4
$1H_2SO_4$(97 %):$8H_2O_2$(30 %):$8H_2O$	•	1.6 $\mu m/min$ in <011> and 2.5 $\mu m/min$ in <010>	•	•
$10H_2SO_4$(10 %):$8H_2O_2$(30 %):$71H_2O$	•	0.48 $\mu m/min$	•	•
1HCl(37 %):$4H_3PO_4$(85 %)	0.6 $\mu m/min$	•	•	•
BHF	•	•	0.6 $\mu m/min$	0.15 $\mu m/min$

we used InGaAs as a sacrificial layer and the etch solution, H_2SO_4:H_2O_2:H_2O, has been commonly used as a selective wet etchant for InGaAs and InGaAsP. The most comprehensive study of the selective undercut etching of the InGaAs is described in [68]. However, because the mixture composition is different from what we use at our facility, the test has to be performed. The process for testing the undercut etch rate is different from the usual etch rate test in the <100> direction. As seen in Fig. 4.10, the square boxes rotating at different angles were patterned on the InP layer. The InP was removed by dry etching and then the InGaAs was wet etched.

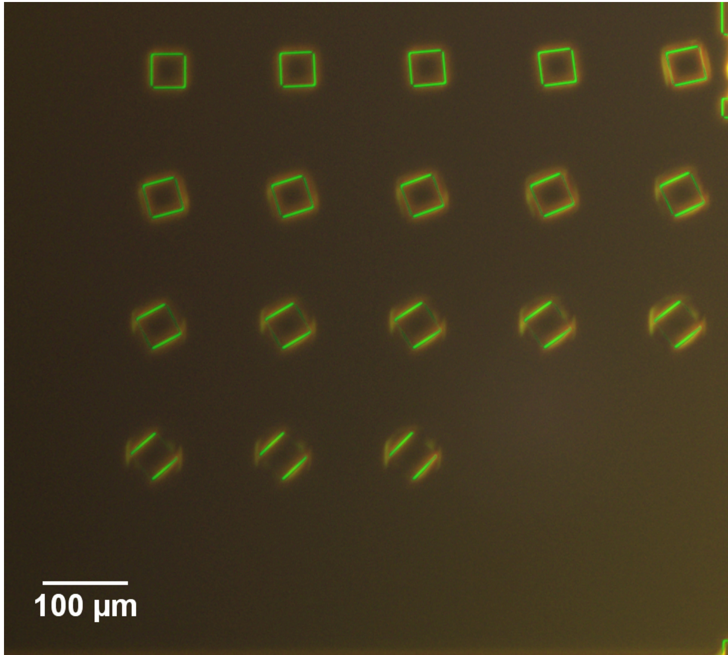

Figure 4.10: Microscope image of a InGaAs wet etching.

4.2.4 Lift off process

Lift off process is a method to create a pattern where direct etching is difficult. Normally, the lift off process is done during the metallization step. By starting the process with defining a pattern with the lift off resist using standard photolithography, a metal film is deposited over the substrate covering the photoresist afterwards. During the lift-off, the photoresist under the thin film is removed, taking the film on top with it, and leaving the film deposited on the substrate behind. Because the process parameters of the lift off process have not been developed in our facility before, the process development was needed. Initial parameters were derived from the manufacturer datasheet. However, we used different light source power and developer from the manufacturer. Thus, we fixed all other parameters and varied exposure and development time. Figure. 4.11 shows the undercut profile of the lift-off resist exposed for 11 sec under the UV light and developed for 180 sec. The lamp power was 5 mW/cm^2. In this figure, we obtained an undercut height which is used to determine the maximum thickness of metal we can deposit on. Figure 4.12 shows the microscope pictures

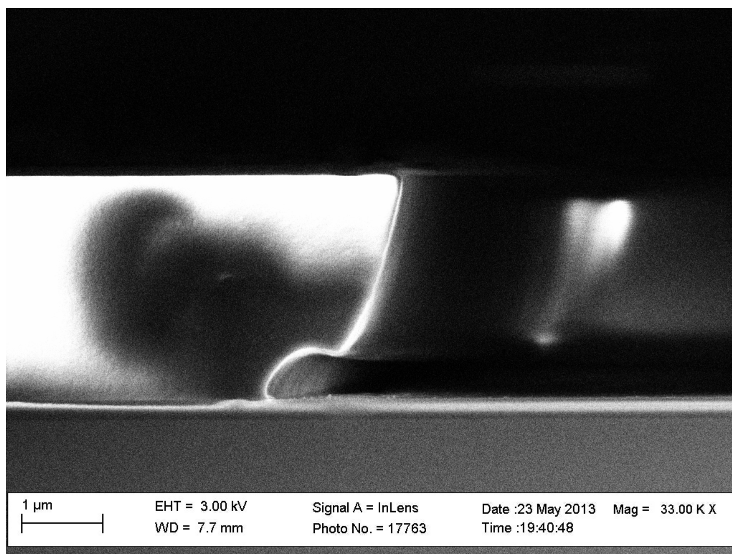

Figure 4.11: Undercut profile of the lift off resist exposed for 11 sec and developed for 180 sec.

of the sample with 9, 10, 11 sec exposure time. We can see that the undercut is larger with the lesser exposure time. If the exposure time was less than 9 sec, the resist erosion started to appear. Therefore, in the main processing, 9 sec exposure was chosen.

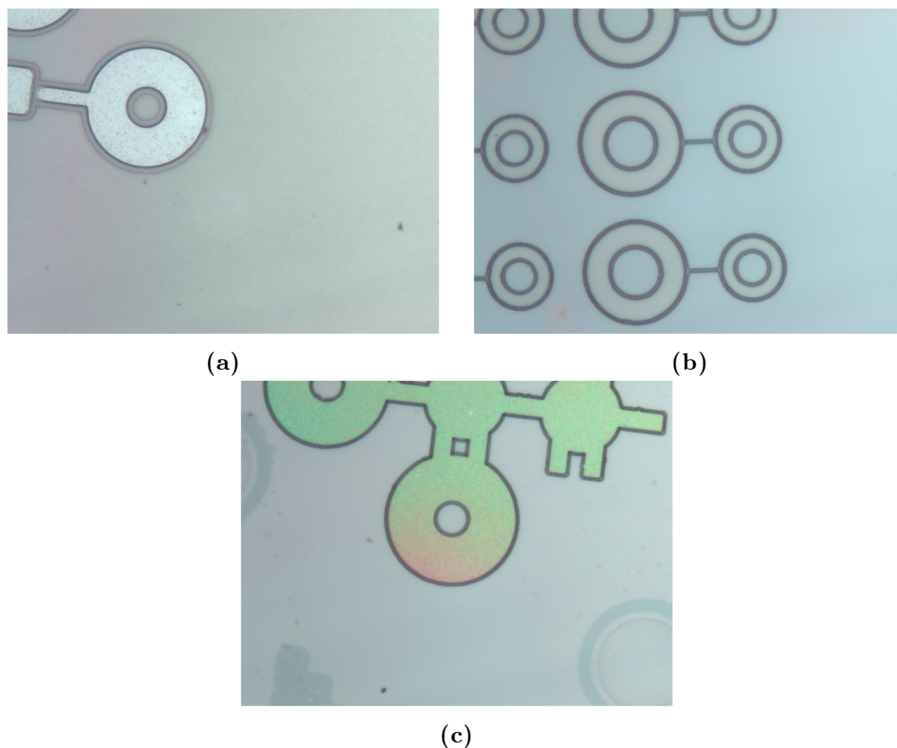

(a) (b)

(c)

Figure 4.12: Microscope images images of the (a)9 sec (b) 10 sec (c) 11 sec exposure time of the AZ2020 negative resist on the BCB.

4.2.5 Metal deposition on a tapered BCB

The final experiment that was done before starting the full device processing was metal deposition in the BCB. Here, we needed to confirm that the deposited metal can be lifted off with the given metal thickness. In addition, we would like to see the BCB sidewall profile after dry etching which affect the metal coverage. From this experiment, we deposited 200 nm SiO_2 as an intermediate layer between the substrate and the BCB. There was no problem lifting off the resist. However, when we took the cross-section image of the sample, we found a metal disconnection between the substrate and the BCB. This is a result of an undercut air gap of the SiO_2 under the BCB. Therefore, in the full processing, we designed the metal line to continue from the contact area to the BCB. Thus, the intermediate layer would not play a role when the metal thin film climbs up the slope of the BCB side wall. Figure 4.13 shows the BCB profile before and after the annealing. We could see that the BCB shrunk after

the thermal processing. With this information, we chose to anneal the sample before the metal deposition to minimize the shrinkage which could cause the metal disconnection in the subsequent processing.

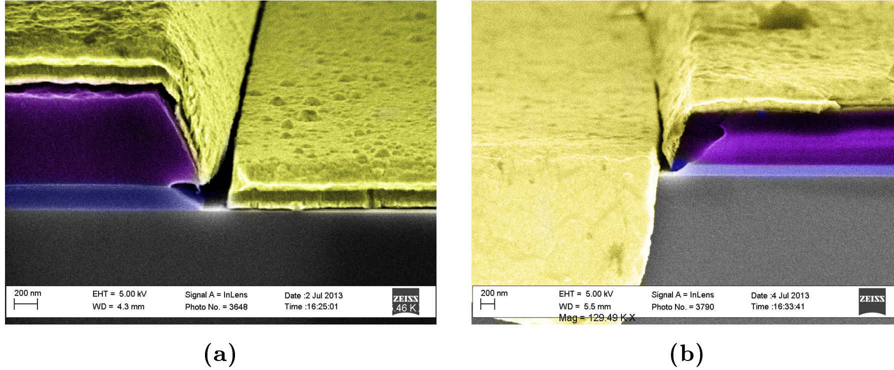

(a) (b)

Figure 4.13: Cross-section SEM images of the metal deposition (a)after lift off (b) after rapid thermal annealing process.

4.3 Summary

Processing flow and process development of the HCG-HG RCE photodetector has been presented in this chapter. The chapter begins by describing the whole process of making the device. Then, specific process developments were described.

Chapter 5

Device Characterization

In this chapter, we present the proof-of-concept measurement results of the 1550 nm RCE photodetectors incorporating HG-HCG structure. The device schematic is shown in Fig. 3.12 and the processing procedures are described in Chapter 4. In the following sections, measurement setup will be presented along with issues of the fabricated devices. Results show polarization dependence property of the grating structures. Under TM-polarized light incident, the devices show the peak response around 1550 nm while TE-polarized light incident show flat response. The device responsivity and quantum efficiency will also be discussed.

5.1 Characterization

In Fig.5.1, the microscope image of the first batch device is shown. The size of the grating area in the middle is 12×12 μm^2. The folded beam suspensions are measured to be 0.8 μm wide and the border around the grating area is 2 μm wide. The area with a rainbow contour is covered with Si_3N_4. The p-contact area is on the lower right corner. The n-contact area is on the lower left corner and the tuning contact is on top of the picture.

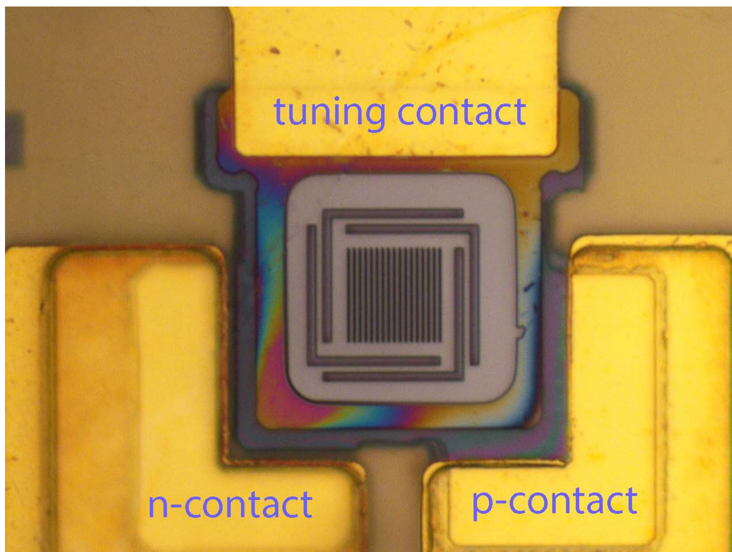

Figure 5.1: Microscope picture of the device after finishing the fabrication.

5.1.1 Characterization set up

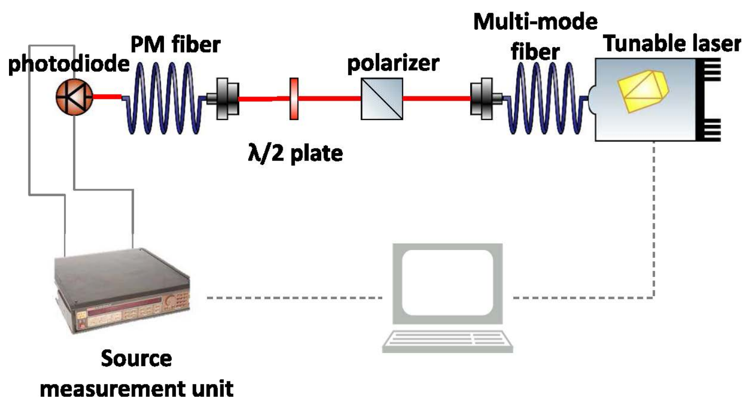

Figure 5.2: Measurement setup.

The characterization setup is illustrated in Fig. 5.2. The light output of a tunable laser with a sweeping range from 1480 nm to 1580 nm is coupled to a multimode fiber. Then, the laser light passes through a linear polarizer and a half-wave plate and is coupled a polarization-maintaining (PM) fiber. The other end of the PM fiber has been cleaved using a fiber cleaver. The laser light from the PM fiber is projected onto the top grating of a device under investigation.

Electrical probes from a source measurement unit are placed on the p- and n-contact pads to measure the current-voltage characteristics. An automation of the measurement was done with LabVIEW as shown in 5.2. Because the tunable laser is elliptically polarized, changing the polarization state with the linear polarization alone would also change the laser output power. Therefore, we fixed the linear polarizer to an angle with maximum output power and change the polarization state using the half-wave plate. During the characterization, there were a few issues worth mentioning. First, it was difficult to align the fiber to the grating area. Because the grating area is small and observing the fiber core through a microscope was not possible in our setup, determining a position was done manually by assuming the maximum current output position as the center of the grating.

5.1.2 Diode characteristics: Current vs. Voltage

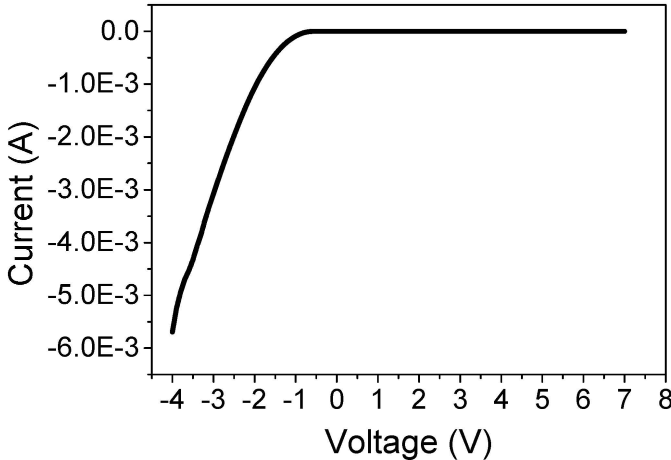

Figure 5.3: Diode characteristic.

First, a diode current-voltage measurement was performed and a result of the device is shown in Fig.5.3. A differential resistance of this device is 450 ohm. The reverse saturation current is 0.6 nA. From the measurement of 8 devices, the minimum differential resistance was 260 ohm and the maximum was 950 ohm. On average the differential resistance is 400-500 ohm. The junction breakdown was not observed below 10 V. From the diode equation

$$I = I_0(e^{\frac{eV}{k_B T}} - 1) \tag{5.1}$$

where I_0 is the reverse saturation current, V is the diode voltage, k_B is the Boltzmann constant, and T is the temperature. The dark current is approximately 0.6 nA at 3 V reverse bias.

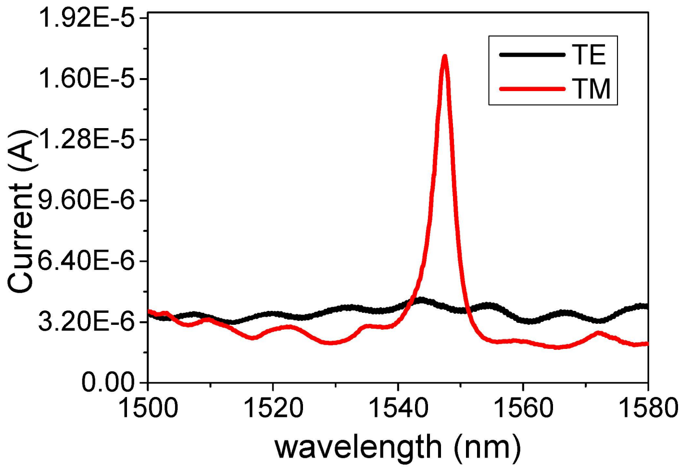

Figure 5.4: Light-Current characteristic of the RCE photodetector.

5.1.3 Photocurrent spectrum

After we have confirmed the diode characteristic, the fiber was aligned on top of the grating and the fiber tip was approached the device without touching the grating. The reflected power at the cleave interface is estimated to be 19% by assuming the core refractive index of 1.47. With the numerical aperture of 0.13, the divergence angle of the beam is equal to 5 degree. The mode field diameter as specified by the manufacturer is 9.8 μm. Thus, the air gap between the fiber and the grating must not exceed 12 μm for the laser spot to be within the grating area. From the experiment setup, it was difficult to achieve, we could estimate the air gap spacing between the fiber and the grating to be 100 μm by calculating from a free spectral range of the noise floor in Fig. 5.4. The figure also shows that the device responds differently at different polarization. With the laser output power of 0 dBm, the maximum output current for 1547.5 nm TM-polarized light incident is 17.2 μA and for the TE-polarized light incident is 4.1 μA. If we assumed 10 dBm loss at the fiber coupling and 19% of the power reflected back at the cleaved interface, the incident power projected to the grating would equal to -10.9 dBm and the responsivity of the device is calculated to be 0.21 A/W for the TM-polarized incident and 0.05 A/W for the

TE-polarized light incident. The responsivity can be converted to the device quantum efficiency by the following equation,

$$R = \eta \frac{e}{hv} \tag{5.2}$$

where hv is the photon energy, e is the elementary charge, and η is the quantum efficiency. The calculated quantum efficiency of the device is 16.8% for the TM-polarized light incident and 4% for the TE-polarized light incident. However, the simulated quantum efficiency of the designed structure was 90%. This drastic performance reduction of the device compares to the simulation is partly due to the change of the epitaxial structure as described in tab.5.1 and tab.5.2. For the proof-of-concept purpose, the quantum wells layers in the simulation have been replaced by a single InGaAs absorbing layer. Because growing the quantum wells is more complicated than the normal absorbing layer, the InGaAs was chosen for a fast turn around time. In addition, the etching process is simpler for InGaAs than the quantum wells because wet etch selectivity between the InGaAs and InP is high. The quantum well layers often contain Aluminum content which does not react well with wet etch chemical and has poor selectivity over the InP. The main numerical difference between the simulated and fabricated structures lies in the refractive index of the barrier layer. The detection linewidth of the measured device was 3.25 nm, while the simulated structure was only 0.9 nm. This large difference is a result of absorption coefficient mismatches used in the simulation tool. As seen in Fig. 5.5, the resonance linewidth increases as the imaginary part of the refractive index increases. It should also be mentioned that as the absorption increases, the bottom mirror reflectance decreases. Therefore, we expect the quantum efficiency of the device to be lower than that of the design. From the simulation, the efficiency was indeed lower than 30% with different material and absorption coefficient.

Apart from confirming the resonance characteristics, we have also measured current-voltage characteristics as a function of laser output power. Figure 5.6 shows the current output rises as the reverse bias increases. At certain voltages, the current becomes saturated. This saturation voltage increases as the laser power increases.

Lastly, we have measured several devices with different grating widths. From the calculation, if the grating width is wider than the design by 5 nm, the resonant wavelength should be red shifted by 3 nm and vice versa if the grating width is smaller than the design by 5 nm. This tendency has not shown in Fig. 5.7 where both grating width offset were blue shifted. We believe this is due to variation of the fabrication, even though all the 4 devices were less than 500 μm apart from each other. The detection linewidth ranges from 4.3 to 7 nm. The

Table 5.1: Epitaxy structure of the simulated RCE photodetector

Repeat count	**Layer name**	**Material**	**thickness** (nm)	**Doping concentration** (cm^{-3})	**n**
1	top grating	InP	530	5×10^{17}	3.1661
1	air gap	air	664		1
1	p-cladding	InP	380	1×10^{18}	3.1661
1	cladding	InP	245		3.1661
1	barrier	InAlGaAs	7.5		2.9
5	absorbing	InGaAs	6.5		3.5911
5	barrier	InAlGaAs	7.5		2.9
1	cladding	InP	131.9		3.1661
1	n-cladding	InP	133	1.5×10^{18}	3.1661
1	bottom grating	Si	497		

Table 5.2: Epitaxy structure of the fabricated RCE photodetector

Repeat count	**Layer name**	**Material**	**thickness** (nm)	**Doping concentration** (cm^{-3})	**n**
1	top grating	InP	530	5×10^{17}	3.1661
1	air gap	air	664		1
1	p-cladding	InP	380	1×10^{18}	3.1661
1	cladding	InP	272		3.1661
1	absorbing	InGaAs	12		3.5911
1	cladding	InP	97		3.1661
1	etch stop	InGaAsP	5		3.1661
1	n-cladding	InP	189.9	1.5×10^{18}	3.1661
1	bottom grating	Si	497		

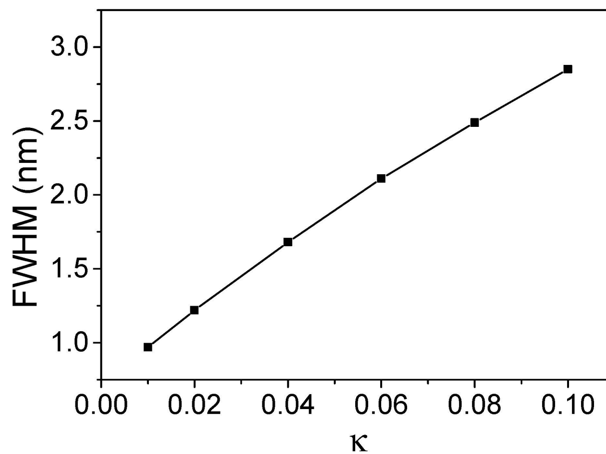

Figure 5.5: Resonant linewidth as a function of imaginary part of the refractive index in the absorbing layer.

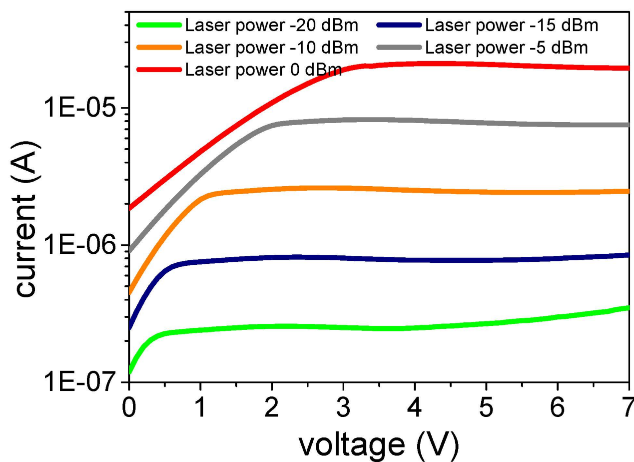

Figure 5.6: Current-Reverse bias voltage characteristic of a TM-polarized light incident as a function of laser power at resonant wavelength.

peak position is at 1551.47 nm for the device with grating offset of -5 nm from the design and 1555.45 nm for the device with no grating offset.

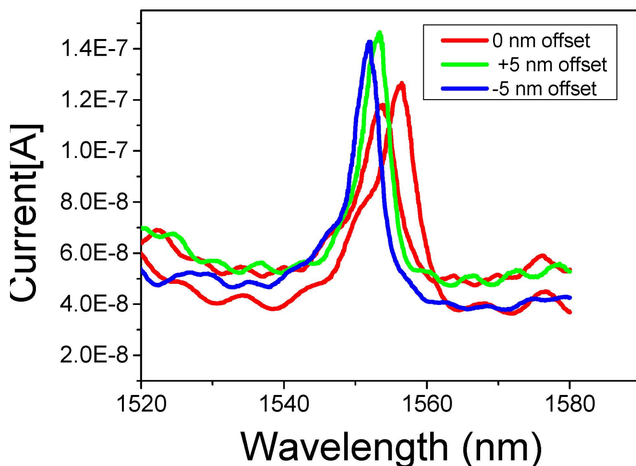

Figure 5.7: Grating width vs resonant wavelength of the TM-polarized light incident with the laser power of -20 dBm.

5.2 Discussion on the broken metal lines

Figure 5.8a and 5.8b shows the continuity of the metal lines from the contact area to the BCB layer. It is shown that there is discontinuity in some part of the p-contact. This was thought to be because of the step different of the p-InP and the BCB in the first batch. However, the discontinuity was still observed in the second batch with the step difference of less than 100 nm. We have not concluded the cause of this disconnection yet, but we suspect the air gap formed during wet etching of the Si_3N_4 intermediate layer causes a small space in which the metal deposition could not cover.

5.3 Summary

In this chapter, the measurement results of the first demonstration of RCE photodetectors using HCG and HG structures have been presented. The performance of the first batch device was not as good as the theoretical calculation due to mismatch of the absorption coefficient and the epitaxial structure. With the laser power of 0 dBm, we have shown the polarization characteristic of the subwavelength grating reflector with the peak current output of 17.2 μA for the TM-polarized light incident and 4.1 μA for the TE-polarized light incident. The

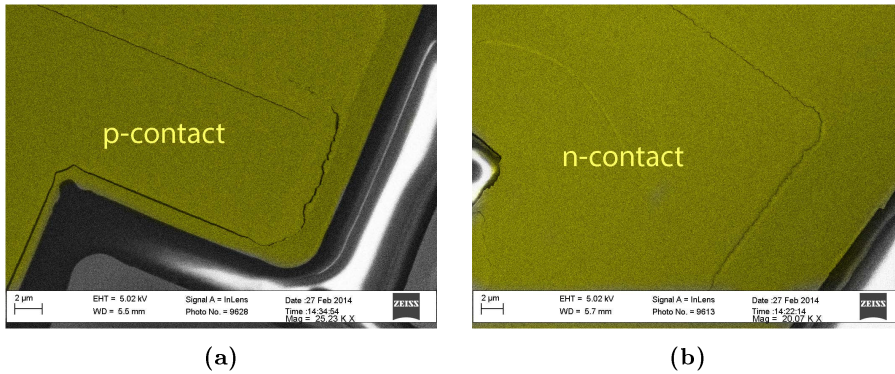

(a) **(b)**

Figure 5.8: (a) and (b) are SEM images of the p- and n-contact area, respectively.

current output demonstrates a linear relationship with the laser power when the bias voltage is greater than 3 V. The saturation voltage increases as the laser power rises. From the calculation, the detection wavelength could be shifted by changing the grating width. However, due to variation in the fabrication process, the devices with grating width differs from the design by ±5 nm have not shown a shift in the expected direction.

Chapter 6

Conclusion and Outlook

6.1 Conclusion

In this thesis, the new designs of the wavelength tunable resonant cavity enhanced photodetector at 1550 nm communication wavelength were proposed and fabricated. Instead of using a conventional distributed Bragg reflector (DBR) as normally uses to form a Fabry-Perot cavity, the dielectric subwavelength grating was introduced. The thesis describes several designs of the cavity by incorporating the HCG and HG mirrors in chapter 3. Different types of cavity show different characteristics. The proposed cavity designs are air coupled cavity, semiconductor coupled cavity and extended cavity. With the semiconductor coupled cavity with DBR as a reference, the proposed device performances were compared. It was shown in the numerical simulation that the ACC configuration yields the broadest tuning range. The SCC configuration performances of the DBR as the reflector and HCG as the reflector are similar. However, the detection linewidth of the HCG device is smaller because of small mode volume. The HG reflector was later introduced in the chapter to solve the problem of chip bonding during the fabrication. The simulation shows improve tuning efficiency, while other characteristics are similar to HCG structure. After deciding to demonstrate the HG structure experimentally, a lot of work was dedicated to developing the processing flow and determining process parameters. Several small processing tests were done. This includes determining the wet etch and

dry etch rate for different type of materials used in the device. Developing the lift-off lithography process parameters. Also, confirming the metal line coverage over the BCB slope profile. Finally, the fabricated devices were characterized using the electrical probe station. We later found that the electrostatic tuning did not function because of an incomplete sacrificial wet etch. The second fabrication attempt failed because of metal lines were broken at the semiconductor contact area and BCB interface.

The devices demonstrate the polarization selectivity. The peak output current with 0 dBm laser power was 17.2 μA for the TM-polarized light incident. The TE-polarized light incident produced 4.1 μA at the same wavelength. We believe that the device responsivity was not as good as the design largely because of the mismatch of the absorption coefficient used in the simulation and the fabricated device.

6.2 Outlook

Only a few measurements have been performed on the proposed RCE photodetectors due to low fabrication yield. A lot of work is left to be done on improving the processing flow. Although, many issues have been solved, the main issues on metal disconnection remain unsolved. Previously, we speculated that the disconnection could have occurred because of a large step different between the InP contact area and the BCB support area. However, after confirming a minimal step different of < 100 nm in the second fabrication batch. The disconnection was still observed.

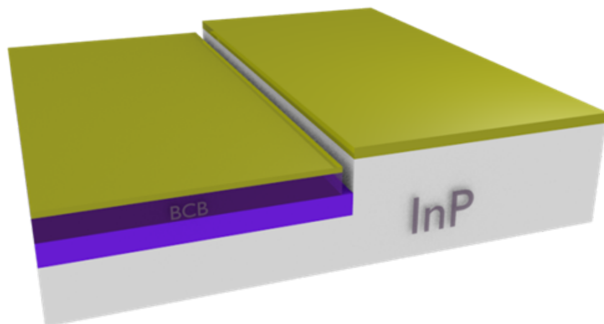

Figure 6.1: Schematic of the metal disconnection part.

The characterization was done to see the basic characteristic of the devices. A few others measurement could have been done. For example, the device speed response and contact resistance. Although, we have included test structures in the mask layout, the structures were damaged during the fabrication. Therefore, it could not be measured.

Despite all the issues, we have successfully demonstrated the novel RCE photodetector with the HG/HCG structure under static operation. In the future, after solving the metal disconnection issue, we hope to be able to demonstrate the electrostatic tuning properties of the device. The simulation results show promising tuning range and tuning efficiency, which could not be achieved by the conventional RCE structure.

Appendix A

Fabrication Process

A.1 Process Flow

1. Preparation		
Cleave wafer		Cleave SOI wafer into 1.5 cm x 3 cm and 3 cm x 3 cm
Cleaning	Solvent bench	Acetone 10 mins + Iso-propanol(IPA) 5 mins in ultrasonic bath
Inspection	Filmtek	Measure silicon thickness on the SOI chips
Cleaning	Solvent bench	rinse with deionized(DI) water to remove particles
2. Bottom grating patterning		
Spin coat resist	III-V spinner	Spin on ZEP 520a 5.5% anisol @ 4000 rpm for 60 sec.
Soft bake	Hot plate	Bake at 160 °C (set point), 2 min

Exposure	e-beam writer	Load samples on chip cassette A and B, Dose 250 $\mu C/cm^2$, Condition files: 2nA, aperture 7(for grating pattern) and 60nA, aperture 7(for noncritical pattern), Voltage 100 kV
Develop	Solvent bench	1 min in ZED-N50(no stirring). IPA rinse 30 sec. DI water rinse 1 min.
Post exposure bake	Hot plate	Bake at 110°C (set point), 3 min
Cleaving		Cleave SOI chips into 1.5 cm x 1.5 cm and blow clean particles with nitrogen gun
Pattern transfer	ASE	Recipe: process/set/com/nanoetch, 11 cycles, pressure 10 mTorr, chamber temperature 10°C, Use 4 inches Si carrier. Run cleaning recipe after finish the processing.
Resist strip	Solvent bench	Dip in MR1165 15 min in the ultrasonic bath. *This step should be done right before the bonding step.*

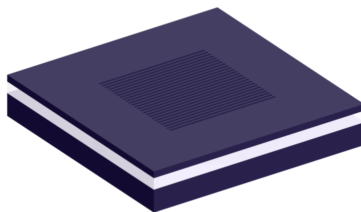

3. Chip bonding

Cleave wafer		Cleave III-V epitaxy wafer into 4 pieces of 8 mm x 8 mm
Inspection	SEM	Measure epitaxy thicknesses
Cleaning	Solvent bench	Clean both the III-V epitaxy and SOI 5 min in acetone, 5 min IPA in the ultrasonic bath, and 1 min in running DI water.
Inspection	Microscope	Inspect for particles. If not clean, repeat the cleaning process.

Remove cap layer	Acid bench	Remove InP cap layer of the III-V epitaxy sample by dipping in the HCl(37 %) 10 sec, rinse with DI water 1 min, dip in 1 H_2SO_4(97 %):8 H_2O_2(30 %):8 H_2O 10 sec, and rinse again with DI water 1 min.

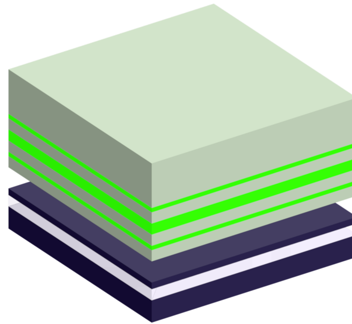

Inspection	Microscope	Inspect for particles. If not clean, try to rinse in DI water.
RCA1 clean	Acid bench	Clean both the III-V sample and SOI chip.
O_2 Plasma treatment	III-V RIE	Treat with O_2 plasma. No carrier wafer.
Thin film activation	Solvent bench	Immerse in DI water.
Dehydration	Hot plate	Bake both samples.
Room temperature bonding		Manually put the III-V epitaxy on top of the SOI sample.
Low temperature bonding	EVG-NIL	

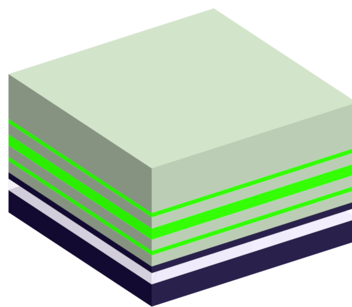

Inspection	SEM	Measure the grating width on test structure outside the bonded area.

InP Substrate removal	Acid bench	Immerse the bonded sample in HCl(37%) for 1 hr with continuous magnetic rod stirring. DI water rinse 1 min.
Resist spin on	III-V spinner	Spin on AZ5214E @ 2000 rpm for 60 sec.
Soft bake	Hot plate	Bake at 90°C for 90 sec.
Remove protuding edge		Manually remove the remaining InP around the edge with a diamond pen.
Cleaning	Solvent bench	Remove the resist with acetone 5 mins, ethanol 5 min in ultrasonic bath. DI water rinse 1 min

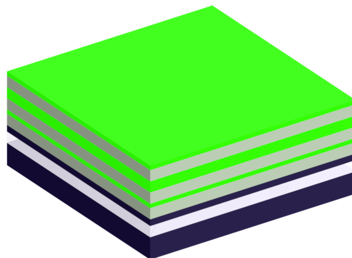

Remove InGaAs etch stop	Acid bench	Immerse the sample in 1 H_2SO_4(97 %):8 H_2O_2(30 %):8 H_2O 20 sec. DI water rinse 1 min.

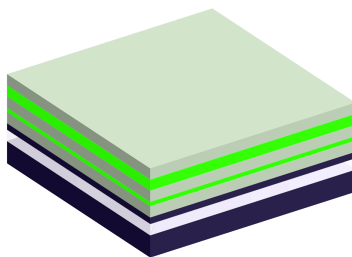

4. Top grating patterning		
Deposit Si_3N_4 hard mask	PECVD2	Recipe: sinstd80, time: 3 min 20 sec. Expected thickness 200 nm. Put 1.5 cm x 1.5 cm Si dummy sample in the chamber together with the bonded sample.

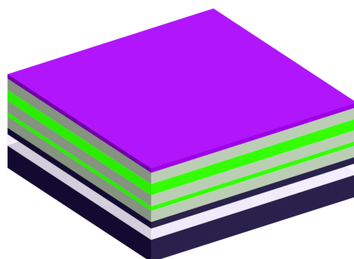

Inspection	Filmtek	Measure and record the Si_3N_4 film thickness on Si dummy sample.
Spin coat resist	III-V spinner	Spin on ZEP 520a 11% anisol @ 2600 rpm for 60 sec. Expected thickness is 500 nm.
Soft bake	Hot plate	Bake at 170 °C (set point), 5 min
Exposure	e-beam writer	Load samples on chip cassette B and C, Dose 250 $\mu C/cm^2$, Condition files: 0.8nA, aperture 5, Voltage 100 kV. Do alignment with the bottom grating.
Develop	Solvent bench	2 min in ZED-N50(no stirring). IPA rinse 30 sec. DI rinse 1 min.
Pattern transfer to Si_3N_4	III-V RIE	Recipe: si3n4std, etch time: 10.20 min. No carrier wafer. Clean the chamber after use, recipe: clean.
Resist stripping	Solvent bench	Dip in MR1165 1 hr in the ultrasonic bath @ 60°C.

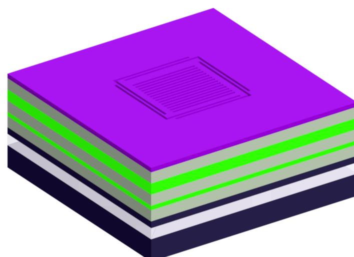

Pattern transfer to InP	III-V RIE	Preconditioning chamber, recipe: morie/precond. InP etch with recipe: coral/cyc3ch42, 9 cycles, 2.30 min/cycle, Use 2 inches InP carrier wafer. Clean the chamber after use, recipe: vlclean.
Remove hard mask	Acid bench	Dip in BHF 2 min. DI water rinse 1 min.

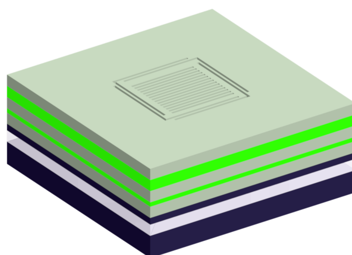

5. Mesa1 Patterning

Deposit Si_3N_4 hard mask	PECVD2	Recipe: sinstd80, time: 3.20 min. Expected thickness 200 nm. Put 1.5 cm x 1.5 cm Si dummy sample in the chamber together with the bonded sample.
Inspection	Filmtek	Measure and record the film thickness on Si dummmy sample. It is important to record the thickness at this step.

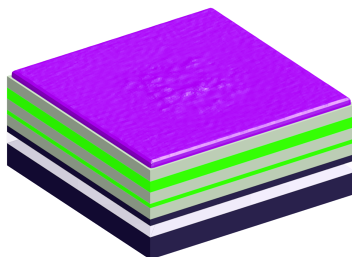

HMDS application	Solvent bench	Put samples in HMDS vapour 15 min and leave in free air 5 min.

Spin coat resist	III-V spinner	Spin on AZ5214E @ 6000 rpm for 30 sec. Expected thickness is 1.5 μm.
Soft bake	Hot plate	Bake at 90 °C (set point), 90 sec.
Exposure	III-V aligner	Mask layer: MESA1, exposure time 8 sec, vaccuum mode. Lamp power 5 mW/cm^2. Room humidity should be around 44%, temperature 22-23°C.
Develop	Solvent bench	60 sec in 1 AZ351B:5 H_2O. DI rinse 1 min.
Descum	III-V asher	40% power, 60 sec.
Hard bake	Hot plate	130°C (set point), 60 sec.
Pattern transfer to Si_3N_4	III-V RIE	Recipe: si3n4std, etch time: 5.30 min. No carrier wafer. Monitor etch completion with the laser end point detector. Clean the chamber after use, recipe: clean.
Resist stripping	Solvent bench	Dip in acetone 10 min, ethanol 3 min in the ultrasonic bath
Inspection	DEKTAK	Measure and record the step height different.

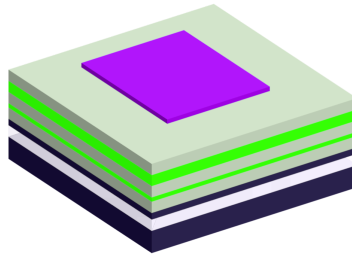

Pattern transfer to InP	III-V RIE	Preconditioning chamber, recipe: morie/precond. InP etch with recipe: inpstd, 8 cycles, 2.30 min/cycle. Exptected etch rate: 29 nm/min. Use 2 inches InP carrier wafer. Clean the chamber after use, recipe: vlclean.

Pattern transfer to InGaAs	Acid bench	Dip the sample in 10 H_2SO_4(10 %):8 H_2O_2(30 %):71 H_2O 40 sec. Then, monitor the etch depth with DEKTAK. Repeat the process until the remaining InGaAs thickness is approximately 300 nm. Etch rate approx. 0.5 $\mu m/min$

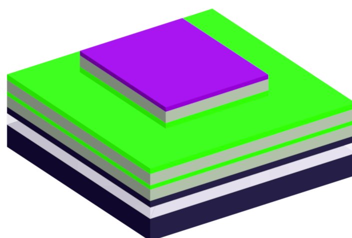

6. Mesa2 Patterning		
Deposit Si_3N_4 hard mask	PECVD2	Recipe: sinstd80, time: 3.20 min. Expected thickness 200 nm. Put 1.5 cm x 1.5 cm Si dummy sample in the chamber together with the bonded sample.
Inspection	Filmtek	Measure and record the film thickness on Si dummmy sample. It is important to record the thickness at this step.
HMDS application	Solvent bench	Put samples in HMDS vapour 15 min and leave in free air 5 min.
Spin coat resist	III-V spinner	Spin on AZ5214E @ 4000 rpm for 30 sec. Expected thickness is 1.7 μm.
Soft bake	Hot plate	Bake at 90 °C (set point), 90 sec.
Exposure	III-V aligner	Mask layer: MESA2, exposure time 8 sec, vaccuum mode. Lamp power 5 mW/cm^2. Room humidity should be around 44%, temperature 22-23°C.
Develop	Solvent bench	60 sec in 1 AZ351B:5 H_2O. DI rinse 1 min.
Descum	III-V asher	40% power, 60 sec.

Hard bake	Hot plate	130°C (set point), 60 sec.
Pattern transfer to Si_3N_4	III-V RIE	Recipe: si3n4std, etch time: 5.30 min. No carrier wafer. Monitor etch completion with the laser end point detector. Clean the chamber after use, recipe: clean.
Resist stripping	Solvent bench	Immerse in acetone 10 min, ethanol 3 min in the ultrasonic bath
Resist ashing	III-V asher	100% power, 10 min.

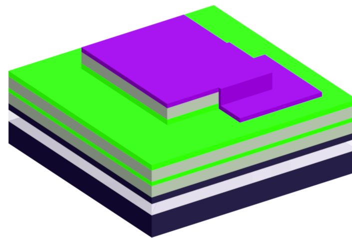

Pattern transfer to InP	III-V RIE	Preconditioning chamber, recipe: morie/precond. InP etch with recipe: inpstd, 13 cycles, 2.30 min/cycle. Then, inspect the step different with DEKTAK. Repeat the process until the etch layer almost reach InGaAs absorbing layer. Exptected etch rate: 29 nm/min. Use 2 inches InP carrier wafer. Clean the chamber after use, recipe: vl-clean.
Wet etch remaining InP	Acid bench	Dip in 1 HCl(37 %):4H_3PO_4 15 sec. Etch rate approx. 0.5 $\mu m/min$
Inspection	DEKTAK	Measure and record the step different.
Wet etch InGaAs absorbing layer	Acid bench	Dip in 10 H_2SO_4(10 %):8H_2O_2(30 %):71 H_2O 10 sec. Etch rate approx. 0.5 $\mu m/min$

Wet etch remaining InP	Acid bench	Dip in 1 HCl(37 %):4H_3PO_4 15 sec. Etch rate approx. 0.5 $\mu m/min$
Inspection	DEKTAK	Measure and record the step different. Repeat the wet etch process if necessary.

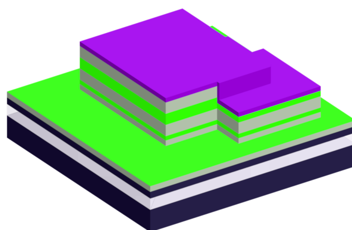

7. Mesa3 Patterning

HMDS application	Solvent bench	Put samples in HMDS vapour 15 min and leave in free air 5 min.
Spin coat resist	III-V spinner	Spin on AZ5214E @ 2000 rpm for 30 sec.
Soft bake	Hot plate	Bake at 90 °C (set point), 90 sec.
Exposure	III-V aligner	Mask layer: MESA3, exposure time 10 sec, vaccuum mode. Lamp power 5 mW/cm^2. Room humidity should be around 44%, temperature 22-23°C.
Develop	Solvent bench	60 sec in 1 AZ351B:5 H_2O. DI rinse 75 sec.
Descum	III-V asher	40% power, 60 sec.
Hard bake	Hot plate	130°C (set point), 60 sec.
Wet etch Q1.1 etch stop layer	Acid bench	Dip in 1 H_2SO_4(97 %):8H_2O_2(30 %):8 H_2O 30 sec.
Wet etch InP	Acid bench	Dip in 1 HCl(37 %):4H_3PO_4 60 sec. Etch rate approx. 0.5 $\mu m/min$
Remove Si_3N_4	Acid bench	Dip in BHF 3 min. Etch rate approx. 0.15 $\mu m/min$

8. Planarization

Deposit Si_3N_4 hard mask	PECVD2	Recipe: sinstd80, time: 3.20 min. Expected thickness 200 nm. Put 1.5 cm x 1.5 cm Si dummy sample in the chamber together with the bonded sample.
Inspection	Filmtek	Measure and record the film thickness on Si dummmy sample. It is important to record the thickness at this step.
Spin on BCB	Solvent bench	Spin on AP3000 @ 1000 rpm for 60 sec.
Bake	Hot plate	Bake at 170 °C (set point), 60 sec.
Spin on BCB	Solvent bench	Spin on Cyclotene 3022-46 @ 3000 rpm for 60 sec.
Bake	Hot plate	Bake at 90 °C (set point), 5 min.
Hard cure	BCB oven	Cure recipe: BCB250BL, cure temperature 250 °C, cure time 5 hrs.
BCB etch back	III-V RIE	Etch BCB back until it is at the same level with InP top grating. Recipe: BCB3MP. Etch time: 8 min and monitor the etch depth with DEKTAK. Repeat the process with 1 min increment until it reaches the target depth. Monitor etch depth with laser end point detection. Etch rate approx. 140 nm/min or 209 nm/cycle. Use 4 inches BCB carrier.

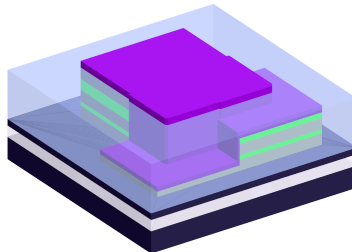

9. MEMS contact opening

HMDS application	Solvent bench	Put samples in HMDS vapour 15 min and leave in free air 5 min.
Spin coat resist	III-V spinner	Spin on AZ5214E @ 4000 rpm for 30 sec. Expected thickness is 1.7 μm.
Soft bake	Hot plate	Bake at 90 °C (set point), 90 sec.
Exposure	III-V aligner	Mask layer: MEMS-CONT, exposure time 10 sec, vaccuum mode. Lamp power 5 mW/cm^2. Room humidity should be around 44%, temperature 22-23°C. Overexpose the pattern to make sure that the resist will be complete clear because descuming cannot be done after BCB application.
Develop	Solvent bench	75 sec in 1 AZ351B:5 H_2O. DI rinse 1 min.
Hard bake	Hot plate	130°C (set point), 60 sec.
Si_3N_4 wet etch	Acid bench	BHF 2 min. DI water rinse 1 min.
Resist stripping	Solvent bench	Immerse in acetone 10 min, ethanol 3 min in the ultrasonic bath
10. Top contact opening		
HMDS application	Solvent bench	Put samples in HMDS vapour 15 min and leave in free air 5 min.
Spin coat resist	III-V spinner	Spin on AZ5214E @ 2000 rpm for 30 sec.
Soft bake	Hot plate	Bake at 90 °C (set point), 90 sec.
Exposure	III-V aligner	Mask layer: TOP-CONT, exposure time 10 sec, vaccuum mode. Lamp power 5 mW/cm^2. Room humidity should be around 44%, temperature 22-23°C. Overexpose the pattern to make sure that the resist will be complete clear because descuming cannot be done after BCB application.
Develop	Solvent bench	75 sec in 1 AZ351B:5 H_2O. DI rinse 1 min.
Hard bake	Hot plate	130°C (set point), 60 sec.

BCB dry etch	III-V RIE	Etch BCB back until it is at the same level with InGaAs P-contact. Recipe: BCB3MP. Etch time: x min and monitor the etch depth with DEKTAK. Repeat the process with 1 min increment until it reaches the target depth. Monitor etch depth with laser end point detection. Etch rate approx. 140 nm/min or 209 nm/cycle. Use 4 inches BCB carrier.
Si_3N_4 wet etch	Acid bench	BHF 2 min. DI water rinse 1 min.
Resist stripping	Solvent bench	Immerse in acetone 10 min, ethanol 3 min in the ultrasonic bath
11. Bottom contact opening		
HMDS application	Solvent bench	Put samples in HMDS vapour 15 min and leave in free air 5 min.
Spin coat resist	III-V spinner	Spin on AZ5214E @ 2000 rpm for 30 sec.
Soft bake	Hot plate	Bake at 90 °C (set point), 90 sec.
Exposure	III-V aligner	Mask layer: BOT-CONT, exposure time 10 sec, vaccuum mode. Lamp power 5 mW/cm^2. Room humidity should be around 44%, temperature 22-23°C. Overexpose the pattern to make sure that the resist will be complete clear because descuming cannot be done after BCB application.
Develop	Acid bench	75 sec in 1 AZ351B:5 H_2O. DI rinse 1 min.
Hard bake	Hot plate	130°C (set point), 60 sec.

BCB dry etch	III-V RIE	Etch BCB back until it is at the same level with InP n-contact. Recipe: BCB3MP. Etch time: x min and monitor the etch depth with DEKTAK. Repeat the process with 1 min increment until it reaches the target depth. Monitor etch depth with laser end point detection. Etch rate approx. 140 nm/min or 209 nm/cycle. Use 4 inches BCB carrier.
Si_3N_4 wet etch	Acid bench	BHF 2 min. DI water rinse 1 min.
Resist stripping	Solvent bench	Immerse in acetone 10 min, ethanol 3 min in the ultrasonic bath
12. n-metalization		
HMDS application	Solvent bench	Put samples in HMDS vapour 15 min and leave in free air 5 min.
Spin coat resist	III-V spinner	Spin on AZ2020 @ 1500 rpm for 60 sec. Expect thickness 2.8 μm
Soft bake	Hot plate	Bake at 110 °C (set point), 60 sec.
Exposure	III-V aligner	Mask layer: N-METAL, exposure time 9 sec, vaccuum mode. Lamp power 5 mW/cm^2. Room humidity should be around 44%, temperature 22-23°C.
Post exposure bake	Hot plate	Bake at 110 °C (set point), 60 sec.
Develop	Acid bench	75 sec in AZ726. DI rinse 2 min.
Contact preparation	Acid bench	Dip in 1 H_2SO_4(97 %):8H_2O_2(30 %):8 H_2O 30 sec.
n-metal deposition	Physimeca	Recipe: Pd20Ge40Ti40Pt20Au200
Metal lift off	Solvent bench	Immerse in MR1165 for 20 min. Continuously shake the sample.

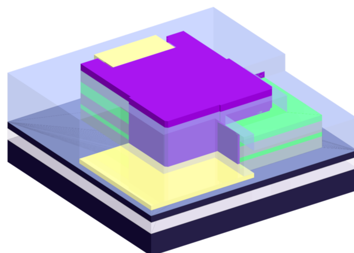

13. p-metalization		
HMDS application	Solvent bench	Put samples in HMDS vapour 15 min and leave in free air 5 min.
Spin coat resist	III-V spinner	Spin on AZ2020 @ 1500 rpm for 60 sec. Expect thickness 2.8 μm
Soft bake	Hot plate	Bake at 110 °C (set point), 60 sec.
Exposure	III-V aligner	Mask layer: P-METAL, exposure time 9 sec, vaccuum mode. Lamp power 5 mW/cm^2. Room humidity should be around 44%, temperature 22-23°C.
Post exposure bake	Hot plate	Bake at 110 °C (set point), 60 sec.
Develop	Acid bench	75 sec in AZ726. DI rinse 2 min.
Contact preparation	Acid bench	Dip in 1 HCl(37 %):4H_3PO_4(85 %) 30 sec. DI water rinse 1 min.
n-metal deposition	Physimeca	Recipe: Ti50Pt75Au250
Metal lift off	Solvent bench	Immerse in MR1165 for 20 min. Continuously shake the sample.
Contact annealing	RTP	Recipe: nalloy, temperature 420 °C, time 5 sec.

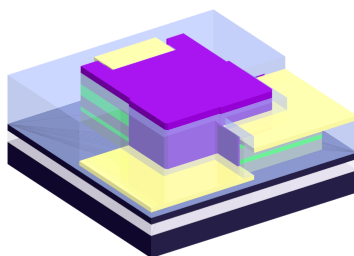

14. Grating MEMS release

HMDS application	Solvent bench	Put samples in HMDS vapour 15 min and leave in free air 5 min.
Spin coat resist	III-V spinner	Spin on AZ5214E @ 2000 rpm for 30 sec.
Soft bake	Hot plate	Bake at 90 °C (set point), 90 sec.
Exposure	III-V aligner	Mask layer: GRAT-OPEN, exposure time 10 sec, vaccuum mode. Lamp power 5 mW/cm^2. Room humidity should be around 44%, temperature 22-23°C.
Develop	Acid bench	75 sec in 1 AZ351B:5 H_2O. DI water rinse 2 min.
Hard bake	Hot plate	Bake at 130 °C (set point), 60 sec.
BCB dry etch	III-V RIE	Remove BCB residue Recipe: BCB3MP. Etch time: 2 min. Etch rate approx. 140 nm/min or 209 nm/cycle. Use 4 inches BCB carrier
Si_3N_4 wet etch	Acid bench	BHF 2 min. DI water rinse 1 min.
InGaAs wet etch	Acid bench	Dip in 1 H_2SO_4(97 %):8H_2O_2(30 %):8 H_2O 50 sec.
Resist stripping	Solvent bench	Immerse in acetone 10 min, IPA 3 min, DI water 1 min.
Dry the structure	Critical point dryer	Put sample in IPA and load into the critical point dryer.

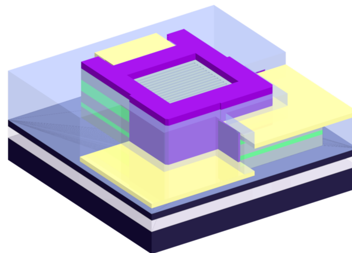

Appendix B

Mask Design

This appendix presents the UV lithography mask design. The processing sequence consists of 2 e-beam lithography steps and 9 UV contact lithography steps. First, the 15 mm x 15 mm SOI chip was patterned by e-beam lithography using 2 current exposures.

Figure B.1: Full mask layout

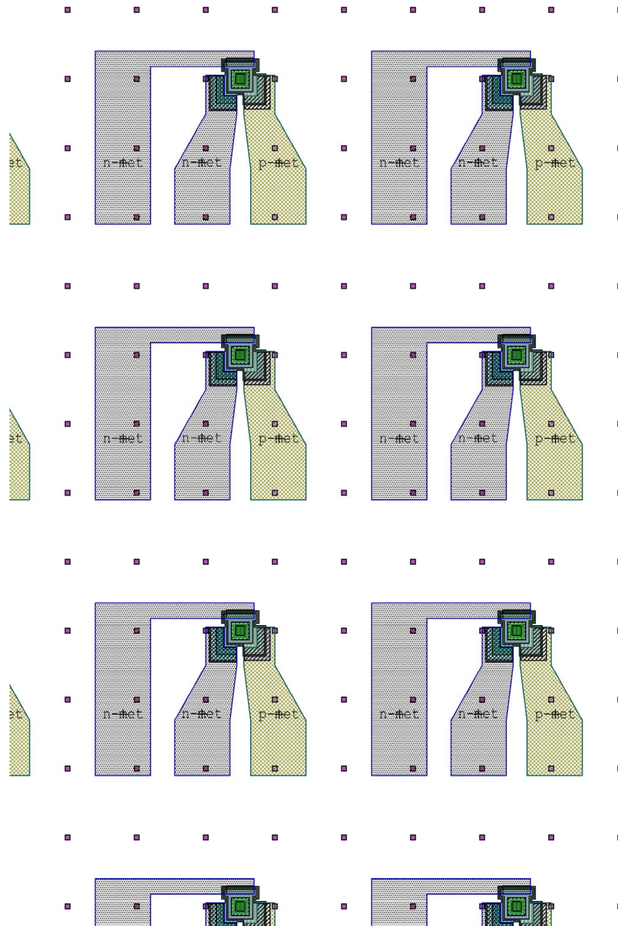

Figure B.2: Device overview

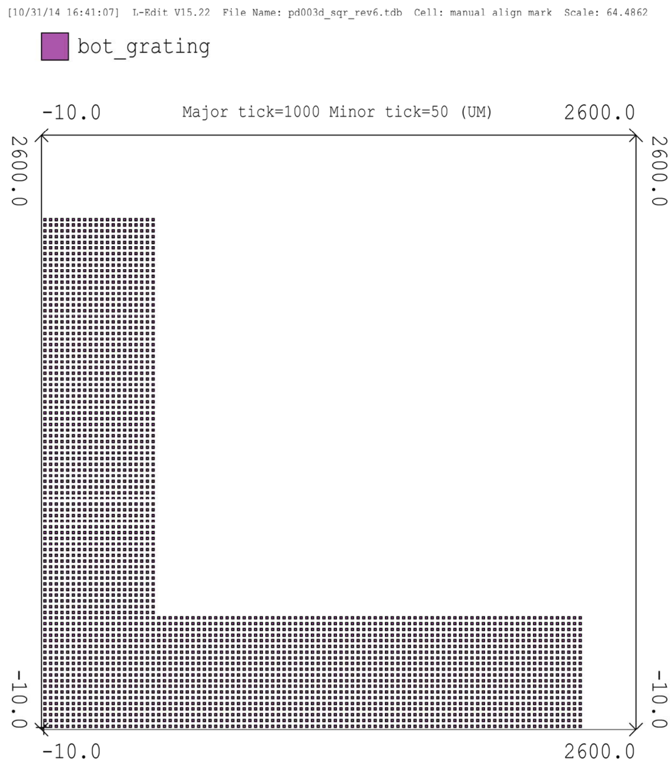

Figure B.3: Bonding guide

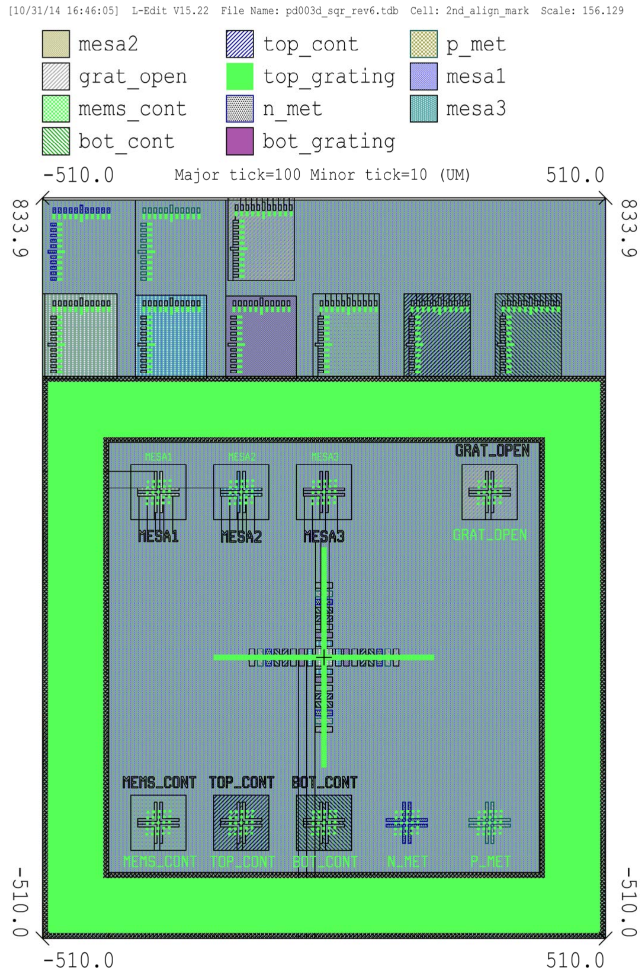

Figure B.4: Alignment mark set

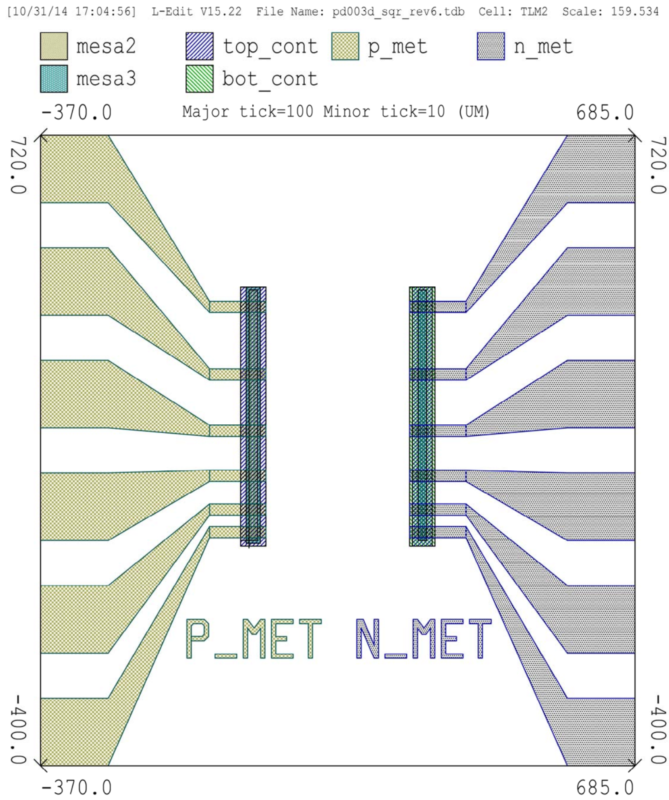

Figure B.5: Contact resistant test structure.

Appendix C

Device Structure

C.1 Double HCG Device Structure

Table C.1: Device structure of SCC with 2 DBRs

Repeat count	**Layer name**	**thickness** (nm)	**Doping concentration** (cm^{-3})	**n**	$\alpha(cm^{-1})$
9	DBR1	115.0		3.37	
9	DBR2	132.3		2.93	
1	DBR1	115.0		3.37	
1	air gap	1162.5		1	
1	p++	50.0	1.5×10^{18}	3.1661	10.5
1	p	47.4	5×10^{17}	3.1661	3.5
1	p++	50.0	1.5×10^{18}	3.16661	10.5
1	p	301.9	5×10^{17}	3.1661	3.5
1	barrier	7.0		3.4	
5	QW	6.6		3.4	810
5	barrier	7.0		3.4	
1	n+	326.9	8×10^{17}	3.1661	2.4
30	DBR1	115.0		3.37	
30	DBR2	132.3		2.93	

Table C.2: Device structure of EC with 2 HCGs

Repeat count	**Layer name**	**thickness** (nm)	**Doping concentration** (cm^{-3})	**n**	$\alpha(cm^{-1})$
1	HCG1	530.0	5×10^{17}	3.1661	
1	air gap	724.2		1	
1	AR	263.6		1.47	
1	p++	50.0	1.5×10^{18}	3.1661	10.5
1	p	169.8	5×10^{17}	3.1661	3.5
1	p++	50.0	1.5×10^{18}	3.16661	10.5
1	p	301.9	5×10^{17}	3.1661	3.5
1	barrier	7.0		3.4	
5	QW	6.6		3.4	810
5	barrier	7.0		3.4	
1	n+	694.1	8×10^{17}	3.1661	2.4
1	SiO_2	1040.1		1.47	
1	HCG2	500.0		1.47	

Table C.3: Device structure of ACC with 2 HCGs

Repeat count	**Layer name**	**thickness** (nm)	**Doping concentration** (cm^{-3})	**n**	$\alpha(cm^{-1})$
1	HCG1	480.0	5×10^{17}	3.1661	
1	air gap	697.9		1	
1	p++	50.0	1.5×10^{18}	3.1661	10.5
1	p	169.8	5×10^{17}	3.1661	3.5
1	p++	50.0	1.5×10^{18}	3.16661	10.5
1	p	301.9	5×10^{17}	3.1661	3.5
1	barrier	7.0		3.4	
5	QW	6.6		3.4	810
5	barrier	7.0		3.4	
1	n+	694.1	8×10^{17}	3.1661	2.4
1	SiO_2	1040.1		1.47	
1	HCG2	500.0		1.47	

Table C.4: Device structure of SCC with 2 HCGs

Repeat count	**Layer name**	**thickness** (nm)	**Doping concentration** (cm^{-3})	**n**	$\alpha(cm^{-1})$
1	HCG1	540.0	5×10^{17}	3.1661	
1	air gap	1496.7		1	
1	p++	50.0	1.5×10^{18}	3.1661	10.5
1	p	47.4	5×10^{17}	3.1661	3.5
1	p++	50.0	1.5×10^{18}	3.16661	10.5
1	p	301.9	5×10^{17}	3.1661	3.5
1	barrier	7.0		3.4	
5	QW	6.6		3.4	810
5	barrier	7.0		3.4	
1	n+	449.3	8×10^{17}	3.1661	2.4
1	SiO_2	1040.1		1.47	
1	HCG2	500.0		1.47	

C.2 Hybrid HG-HCG Device Structure

Table C.5: Device structure of Hybrid HG/HCG structure

Repeat count	**Layer name**	**thickness** (nm)	**n**	$\alpha(cm^{-1})$
1	HCG1	530.0	3.1661	
1	air gap	706.33	1	
1	top cladding	336.0	3.1661	
1	barrier	7	3.4	
2	QW	6.6	3.4	8100
2	barrier	7	3.4	
1	bottom cladding	234.8	3.1661	
1	HCG2	520	3.1661	
1	SiO_2	3000	1.47	

C.3 III-V Epitaxy for Fabrication

Table C.6: Epitaxy structure of the fabricated RCE photodetector

Repeat count	**Layer name**	**Material**	**thickness** (nm)	**Doping concentration** (cm^{-3})	**n**	$\alpha(cm^{-1})$
1	cap layer	InP	20.0		3.1661	
1	etch stop	InGaAs	100.0		1	
1	n-cladding	InP	189.9	1.5×10^{18}	3.1661	2.4
1	etch stop	InGaAsP	5.0		3.1661	
1	cladding	InP	70.0		3.1661	
1	cladding	InP	27.0		3.1661	
1	absorbing	InGaAs	12.0		3.5911	8100
1	cladding	InP	27.0		3.1661	
1	cladding	InP	245.1		3.1661	
1	p-cladding	InP	380.0	1×10^{18}	3.1661	10.5
1	sacrificial/p-cont	InGaAs	300.0	1×10^{19}		
1	sacrificial	InGaAs	364.0			
1	HCG	InP	530.0	5×10^{17}	3.1661	0.01
1	etch stop	InGaAs	250.0			
1	substrate	InP	-			

Bibliography

[1] T. H. Wood, C. A. Burrus, A. H. Gnauck, J. M. Wiesenfeld, Miller, D. A. B., D. S. Chemla, and T. C. Damen, “Wavelength-selective voltage-tunable photodetector made from multiple quantum wells,” Applied Physics Letters, vol. 47, no. 3, p. 190, 1985.

[2] F. Sugihwo, C.-C. Lin, L. A. Eyres, M. M. Fejer, and J. S. Harris, “Broadly-tunable narrow-linewidth micromachined laser/photodetector and phototransistor,” in International Electron Devices Meeting 1998. Technical Digest, pp. 665–668, 6-9 Dec. 1998.

[3] S. Strite and M. S. Ünlü, “Tunable photodetectors and light-emitting diodes for wavelength division multiplexing,” Electronics Letters, vol. 31, no. 8, p. 672, 1995.

[4] G. L. Christenson, A. Tran, Z. H. Zhu, Y. H. Lo, M. Hong, J. P. Mannaerts, and R. Bhat, “Long-wavelength resonant vertical-cavity led/photodetector with a 75-nm tuning range,” IEEE Photonics Technology Letters, vol. 9, no. 6, pp. 725–727, 1997.

[5] R. Chen, Junxian Fu, D. Miller, and J. S. Harris, “Design and analysis of cmos-controlled tunable photodetectors for multiwavelength discrimination,” Journal of Lightwave Technology, vol. 27, no. 23, pp. 5451–5460, 2009.

[6] K. Lai and J. C. Campbell, “Design of a tunable gaas/algaas multiple-quantum-well resonant-cavity photodetector,” IEEE Journal of Quantum Electronics, vol. 30, no. 1, pp. 108–114, 1994.

[7] J. Waclawek, J. Kováč, B. Rheinländer, V. Gottschalch, and J. Škriniarová, "Electrically tunable gaas/algaas mqw rce photodetector," Electronics Letters, vol. 33, no. 1, p. 71, 1997.

[8] M. S. Wu, E. C. Vail, G. S. Li, W. Yuen, and C. J. Chang-Hasnain, "Widely and continuously tunable micromachined resonant cavity detector with wavelength tracking," IEEE Photonics Technology Letters, vol. 8, no. 1, pp. 98–100, 1996.

[9] B. Pezeshki and Harris Jr., James S., "Electrostatically tunable optical device and optical interconnect for processors," 03/01/1994.

[10] K. Kishino, M. S. Unlu, J.-I. Chyi, J. Reed, L. Arsenault, and H. Morkoc, "Resonant cavity-enhanced (rce) photodetectors," IEEE Journal of Quantum Electronics, vol. 27, no. 8, pp. 2025–2034, 1991.

[11] I.-S. Chung, Y. T. Lee, J.-E. Kim, and H. Y. Park, "Effect of outermost layers on resonant cavity enhanced devices," Journal of Applied Physics, vol. 96, no. 5, p. 2423, 2004.

[12] Il-Sug Chung and Yong Tak Lee, "A method to tune the cavity-mode wavelength of resonant cavity-enhanced photodetectors for bidirectional optical interconnects," IEEE Photonics Technology Letters, vol. 18, no. 1, pp. 46–48, 2006.

[13] C. J. Chang-Hasnain, "High-contrast gratings as a new platform for integrated optoelectronics," Semiconductor Science and Technology, vol. 26, no. 1, p. 014043, 2011.

[14] C. J. Chang-Hasnain, "High-contrast gratings as new platform for integrated optoelectronics," in 2010 IEEE 22nd International Semiconductor Laser Conference (ISLC), pp. 3–4.

[15] C. Mateus, M. Huang, L. Chen, C. J. Chang-Hasnain, and Y. Suzuki, "Broad-band mirror (1.12 - 1.62μm) using a subwavelength grating," IEEE Photonics Technology Letters, vol. 16, no. 7, pp. 1676–1678, 2004.

[16] Ye Zhou, M. Huang, C. Chase, V. Karagodsky, M. Moewe, B. Pesala, F. G. Sedgwick, and C. J. Chang-Hasnain, "High-index-contrast grating (hcg) and its applications in optoelectronic devices," IEEE Journal of Selected Topics in Quantum Electronics, vol. 15, no. 5, pp. 1485–1499, 2009.

[17] I.-S. Chung, V. Iakovlev, A. Sirbu, A. Mereuta, A. Caliman, E. Kapon, and J. Mork, "Broadband mems-tunable high-index-contrast subwavelength grating long-wavelength vcsel," IEEE Journal of Quantum Electronics, vol. 46, no. 9, pp. 1245–1253, 2010.

[18] G. P. Agrawal, Fiber-optic communication systems with cd, vol. 222 of Wiley series in microwave and optical engineering. New York: Wiley, 4th ed ed., 2010.

[19] H. S. Nalwa, Photodetectors and fiber optics. San Diego, CA and London: AP, ©2001.

[20] P. V. Ramana, H. Kuruveettil, B. Lee Sik Pong, K. Suzuki, T. Shioda, Tan Chee Wei, J. Chandrappan, Lim Teck Guan, C. Teo Wei Liang, Chai Yi Yoon, Yap Guan Jie, C. Sharmani, and J. H. Lau, "Bi-directional optical communication at 10 gb/s on fr4 pcb using reflow solderable smt transceiver," in 2008 58th Electronic Components and Technology Conference (ECTC 2008), pp. 244–249.

[21] J. Liu, L. C. Kimerling, and J. Michel, "Monolithic ge-on-si lasers for large-scale electronic–photonic integration," Semiconductor Science and Technology, vol. 27, no. 9, p. 094006, 2012.

[22] Z. Fang and C. Z. Zhao, "Recent progress in silicon photonics: A review," ISRN Optics, vol. 2012, no. 21, pp. 1–27, 2012.

[23] Di Liang and J. E. Bowers, "Recent progress in lasers on silicon," Nature Photonics, vol. 4, no. 8, pp. 511–517, 2010.

[24] Heck, Martijn J. R., H.-W. Chen, A. W. Fang, B. R. Koch, Di Liang, H. Park, M. N. Sysak, and J. E. Bowers, "Hybrid silicon photonics for optical interconnects," IEEE Journal of Selected Topics in Quantum Electronics, vol. 17, no. 2, pp. 333–346, 2011.

[25] D. Liang and J. E. Bowers, "Highly efficient vertical outgassing channels for low-temperature inp-to-silicon direct wafer bonding on the silicon-on-insulator substrate," Journal of Vacuum Science & Technology B: Microelectronics and Nanometer Structures, vol. 26, no. 4, p. 1560, 2008.

[26] D. Pasquariello and K. Hjort, "Plasma-assisted inp-to-si low temperature wafer bonding," IEEE Journal of Selected Topics in Quantum Electronics, vol. 8, no. 1, pp. 118–131, 2002.

[27] T. K. Gaylord and M. G. Moharam, "Planar dielectric grating diffraction theories," Applied Physics B Photophysics and Laser Chemistry, vol. 28, no. 1, pp. 1–14, 1982.

[28] M. G. Moharam and T. K. Gaylord, "Rigorous coupled-wave analysis of planar-grating diffraction," Journal of the Optical Society of America, vol. 71, no. 7, p. 811, 1981.

[29] P. Bienstman, "Camfr (cavity modelling framework): Require python 2.7," 2013.

[30] P. Kwiecien, "rcwa-1d," 2014.

[31] C. Mateus, M. Huang, Y. Deng, A. R. Neureuther, and C. J. Chang-Hasnain, "Ultrabroadband mirror using low-index cladded subwavelength grating," IEEE Photonics Technology Letters, vol. 16, no. 2, pp. 518–520, 2004.

[32] T. Ansbaek, I.-S. Chung, E. S. Semenova, and K. Yvind, "1060-nm tunable monolithic high index contrast subwavelength grating vcsel," IEEE Photonics Technology Letters, vol. 25, no. 4, pp. 365–367, 2013.

[33] L. Carletti, R. Malureanu, J. Mork, I.-S. Chung, C. J. Chang-Hasnain, F. Koyama, A. E. Willner, and W. Zhou, "Wave-front-engineered grating mirrors for vcsels," in SPIE OPTO, SPIE Proceedings, p. 82700E, SPIE, 2012.

[34] C. J. Chang-Hasnain, "High-contrast grating vcsels," in VCSELs (R. Michalzik, ed.), vol. 166 of Springer Series in Optical Sciences, pp. 291–317, Berlin, Heidelberg: Springer Berlin Heidelberg, 2013.

[35] Y. Horie, A. Arbabi, and A. Faraon, "Reflective optical phase modulator based on high-contrast grating mirrors," in CLEO: Science and Innovations, p. STh4M.8.

[36] S. Learkthanakhachon, K. Yvind, I.-S. Chung, C. J. Chang-Hasnain, F. Koyama, A. E. Willner, and W. Zhou, "Tunable resonant-cavity-enhanced photodetector with double high-index-contrast grating mirrors," in SPIE OPTO, SPIE Proceedings, p. 86330Y, SPIE, 2013.

[37] W. Yang and C. Chang-Hasnain, "Ultra-compact optical switch using high contrast grating hollow-core waveguide," in CLEO: Science and Innovations, p. CTh4L.7.

[38] Ye Zhou, M. Moewe, J. Kern, M. C. Huang, and C. J. Chang-Hasnain, "A novel high-q resonator using high contrast subwavelength grating," in 2008 Conference on Lasers and Electro-Optics (CLEO), pp. 1–2.

[39] Yi Rao, Weijian Yang, C. Chase, Li Zhu, M. Huang, and C. J. Chang-Hasnain, "Tunable 1550-nm high contrast grating vcsel detector," in 39th European Conference and Exhibition on Optical Communication (ECOC 2013), pp. 933–935, 22-26 Sept. 2013.

[40] L. Zhu, V. Karagodsky, W. Yang, and C. J. Chang-Hasnain, "Novel high efficiency vertical optical coupler using subwavelength high contrast grating," in CLEO: Applications and Technology, p. JTuI2.

[41] V. Karagodsky, F. G. Sedgwick, and C. J. Chang-Hasnain, "Theoretical analysis of subwavelength high contrast grating reflectors," Optics express, vol. 18, no. 16, pp. 16973–16988, 2010.

[42] W. Yang, C. J. Chang-Hasnain, F. Koyama, A. E. Willner, and W. Zhou, "Physics of high contrast gratings: a band diagram insight," in SPIE OPTO, SPIE Proceedings, p. 863303, SPIE, 2013.

[43] V. Karagodsky and C. J. Chang-Hasnain, "Physics of near-wavelength high contrast gratings," Optics express, vol. 20, no. 10, pp. 10888–10895, 2012.

[44] Y. Ding and R. Magnusson, "Band gaps and leaky-wave effects in resonant photonic-crystal waveguides," Optics Express, vol. 15, no. 2, p. 680, 2007.

[45] R. Magnusson and M. Shokooh-Saremi, "Physical basis for wideband resonant reflectors," Optics Express, vol. 16, no. 5, p. 3456, 2008.

[46] S. S. Wang and R. Magnusson, "Theory and applications of guided-mode resonance filters," Applied optics, vol. 32, no. 14, pp. 2606–2613, 1993.

[47] Y. Zhou, Subwavelength High-Contrast Grating (HCG) and its Applications in Optoelectronic Devices. PhD thesis, University of California, Berkeley, 2008.

[48] M. Shokooh-Saremi and R. Magnusson, "Wideband leaky-mode resonance reflectors: Influence of grating profile and sublayers," Optics Express, vol. 16, no. 22, p. 18249, 2008.

[49] A. Taghizadeh, G. C. Park, J. Mørk, and I.-S. Chung, "Hybrid grating reflector with high reflectivity and broad bandwidth," Optics express, vol. 22, no. 18, pp. 21175–21184, 2014.

[50] J. A. Jervase and Y. Zebda, "Characteristic analysis of resonant-cavity-enhanced (rce) photodetectors," IEEE Journal of Quantum Electronics, vol. 34, no. 7, pp. 1129–1134, 1998.

[51] M. S. Unlu, B. M. Onat, and Y. Leblebici, "Transient simulation of heterojunction photodiodes-part ii: analysis of resonant cavity enhanced photodetectors," Journal of Lightwave Technology, vol. 13, no. 3, pp. 406–415, 1995.

[52] L. A. Coldren, S. W. Corzine, and M. L. Mašanović, Diode Lasers and Photonic Integrated Circuits. Hoboken, NJ, USA: John Wiley & Sons, Inc, 2012.

[53] R. W. Mao, Y. H. Zuo, C. B. Li, B. W. Cheng, X. G. Teng, L. P. Luo, J. Z. Yu, and Q. M. Wang, "Demonstration of low-cost si-based tunable long-wavelength resonant-cavity-enhanced photodetectors," Applied Physics Letters, vol. 86, no. 3, p. 033502, 2005.

[54] F. Sugihwo, Design and Fabrication of Wavelength Tunable Optoelectronic Devices. PhD thesis, Stanford University, 1998.

[55] S. D. Senturia, Microsystem design. Boston: Kluwer Academic, 2002.

[56] R. J. Roark, W. C. Young, and R. G. Budynas, Roark's formulas for stress and strain. New York: McGraw-Hill, 7th ed ed., 2002.

[57] S. Adachi, Physical Properties of III-V Semiconductor Compounds. Weinheim, FRG: Wiley-VCH Verlag GmbH & Co. KGaA, 1992.

[58] B. Morgan and R. Ghodssi, "Vertically-shaped tunable mems resonators," Journal of Microelectromechanical Systems, vol. 17, no. 1, pp. 85–92, 2008.

[59] K. Fricke, E. Peiner, M. Chahoud, and A. Schlachetzki, "Fractures properties of inp microcantilevers by hetero-micromachining," Sensors and Actuators A: Physical, vol. 76, no. 1-3, pp. 395–402, 1999.

[60] H. Zhao, L. Yu, and Y. Huang, "Investigation of a chemically treated inp(100) surface during hydrophilic wafer bonding process," Materials Science and Engineering: B, vol. 128, no. 1-3, pp. 93–97, 2006.

[61] S. Franssila, Introduction to microfabrication. Chichester, West Sussex, England and Hoboken, NJ: John Wiley & Sons, 2nd ed ed., 2010.

[62] P. Ramm, J. J.-Q. Lu, and Taklo, Maaike M. V, Handbook of wafer bonding. Weinheim: Wiley-VCH, ©2012.

[63] J. Arokiaraj, S. Tripathy, S. Vicknesh, and S. J. Chua, "Si layer transfer to inp substrate using low-temperature wafer bonding," Applied Surface Science, vol. 253, no. 3, pp. 1243–1246, 2006.

[64] P. Eliá, I. Kosti, J. oltýs, and S. Hasenöhrl, "Wet-etch bulk micromachining of (100) inp substrates," Journal of Micromechanics and Microengineering, vol. 14, no. 8, pp. 1205–1214, 2004.

[65] D. Cuypers, van Dorp, D. H., M. Tallarida, S. Brizzi, T. Conard, Rodriguez, L. N. J., M. Mees, S. Arnauts, D. Schmeisser, C. Adelmann, and S. d. Gendt, "Study of inp surfaces after wet chemical treatments," ECS Journal of Solid State Science and Technology, vol. 3, no. 1, pp. N3016–N3022, 2013.

[66] S. Wolf and R. N. Tauber, Silicon processing for the VLSI era. Vol. 1, Process technology. Sunset Beach, Calif.: Lattice, 2nd ed ed., 2000.

[67] C. Hedlund, "Microloading effect in reactive ion etching," Journal of Vacuum Science & Technology A: Vacuum, Surfaces, and Films, vol. 12, no. 4, p. 1962, 1994.

[68] D. Pasquariello, E. S. Bjorlin, D. Lasaosa, Y.-J. Chiu, J. Piprek, and J. E. Bowers, "Selective undercut etching of ingaas and ingaasp quantum wells for improved performance of long-wavelength optoelectronic devices," Journal of Lightwave Technology, vol. 24, no. 3, pp. 1470–1477, 2006.